Universität Augsburg
Lehrstuhl für
Experimentalphysik I

Universität Augsburg
Mathematisch-Naturwissenschaftlich-
Technische Fakultät

Biological physics at interfaces

On a modern device for cell adhesion
and Einstein at single molecules

Dissertation

zur Erlangung des akademischen Grades

Dr. rer. nat.

eingereicht an der

Mathematisch-Naturwissenschaftlich-Technischen Fakultät

der Universität Augsburg

von

Andreas Hartmann

Augsburg, September 2016

1. Gutachter:	Prof. Dr. Matthias F. Schneider
2. Gutachter:	Prof. Dr. Armin Reller
Tag der mündlichen Prüfung:	09.02.2018

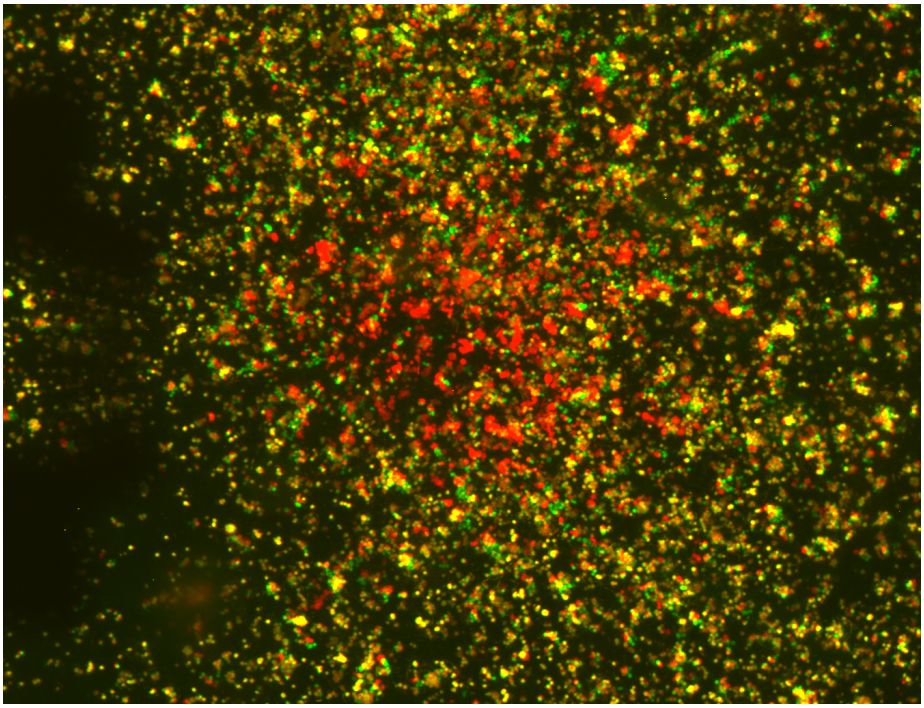

"Ceci n'est pas l'origine du monde", AH, 2012, cf. Fig. 4.32

IV

"Time (...) is what keeps everything from happening at once."

- The Big Business Man
in "The Girl in the Golden Atom" by R. Cummings (1922)

Contents

Chapter 1

Graphical Abstract

Chapter 2

Introduction

The motivation for the present work arises from two antipodes of scientific sources of progress - first, the idea of applying known physical and technological fundamentals in new contexts in order to create new technology as well as second, the general desire of a deeper understanding of physics. This in particular can be achieved by explaining several seeming non-related phenomena by a common, underlying theory.

This led to two big experimental parts that enter this thesis. One is the development of a device for cell adhesion research and several experiments carried out with it. The second deals with a single molecule force spectroscopy experiment on a biopolymer called "von Willebrand factor" (vWF). Therefore, in the following chapter, first several topics which might not be present in every physicists mind will be dealt with such as some basic information on cells and the present state of the physics of cell adhesion. Further on, an important, fundamental model in polymer physics is presented, the Freely-Jointed-Chain-model. As the research for this thesis opened the perspective for the unification of the explanation of different physical phenomena within one theory, this theory, which is based on Einstein's view on thermodynamics, is explicated. In chapter 4, the experimental work and its results are shown including the development of a surface acoustic wave (SAW)-driven device for the application in cell adhesion research. As a proof-of-principle, several initial studies with focus on implant research as well as altered physiological conditions were performed and can be studied there. Further on, the single molecule force spectroscopy experiments on vWF and their results are presented. In particular, the coherence between the experimental observations and the concept of proper entropy of 2-dimensional interfaces based on Einstein's view on thermodynamics is assessed. After a summary and outlook, this thesis ends with a closer look on several technical and experimental details given in the Appendix (see chapter 6).

There is a good tradition of physicists contributing to biological research as can be seen with Hermann von Helmholtz (physiology and energy conservation) or Erwin Schrödinger with his prediction of "aperiodic crystals" being necessary for heredity in his famous book "What is Life?" (cf. Schrödinger (1944)). Following this tradition, the author of this thesis wants to give a small contribution to the ongoing discussion on the specific properties of water at interfaces (cf.

e.g. Gekle (2015)) which is ubiquitous in biology and its connection to entropy considerations as both of the topics worked on in this thesis are closely connected to interfacial water and show promising results in a sense of being able to be integrated within the greater framework of Einstein's thermodynamics. This accompanies with a reduction of complexity as a main task of research in physics in contrast to the governing principle of ever increasing complexity as a prominent principle in biology. Following the principle of parsimony (first formulated by the Franciscan friar William of Ockham), therefore the idea of least hypothesis for the explanation of a phenomenon resp. a set of phenomena, Einstein's thermodynamics hold great potential for scientific progress as at present state, an impressive set of seemingly unrelated observations show indications of being able to be integrated.

Chapter 3

Theory and Basics

3.1 The cell and its membrane

In biology, cells state the smallest living units that exist. Living organisms consist of one cell (unicellular organism) up to huge agglomerations of cells that make up the organism like in the case of animals or humans. In terms of cell adhesion, the surface of cells and its properties are of major importance as they govern the interactions of the cell with its environment. The surface of the cell is mainly composed of a membrane and proteins that either reach through the membrane or are anchored in the membrane. Figure 3.1 shows the hierarchical structure of cell membranes and its constituents. Of particular importance for cell adhesion processes are the lipid bilayer membrane and the embedded proteins which are therefore described in more detail in the following. For a more comprehensive introduction into cell physiology, the reader is advised to use nearly any standard biological textbook like e.g. Silbernagl - Color Atlas of Physiology (Despopoulos and Silbernagl (2003)).

The cell membrane For the understanding of a cell membrane, it is important to know about its generating constituents. Cell membranes mainly consist of phospholipids. These are amphiphilic chemical compounds made up of a so-called glycerol backbone. At the three functional alcoholic groups of a glycerol molecule $C_3H_5(OH)_3$, two fatty acids and a phosphoric acid molecule is bound via esterification. The fatty acids with their long hydrocarbon chains state the hydrophobic part ("tail") of the molecule, the phosphate group states the hydrophilic part ("head"; cf. Fig. 3.1, blue box). This structure leads to self-assembly processes when phospholipids are dissolved in water. The hydrocarbon chains tend to face each other minimizing the exposure to water whereas the head groups face the water molecules. Herein lies the origin of the bilayer structure of cell membranes. For adhesion processes, this means that cells always face other surfaces with the polar head groups with, depending on the surrounding pH, usually a net negative charge (cf. Glaser (1986)).

Membrane proteins Beyond the phospholipids, cell membranes contain various proteins. The mechanism, how they are anchored in the membrane was first described in *The Fluid Mosaic Model of the Structure of Cell Membranes*

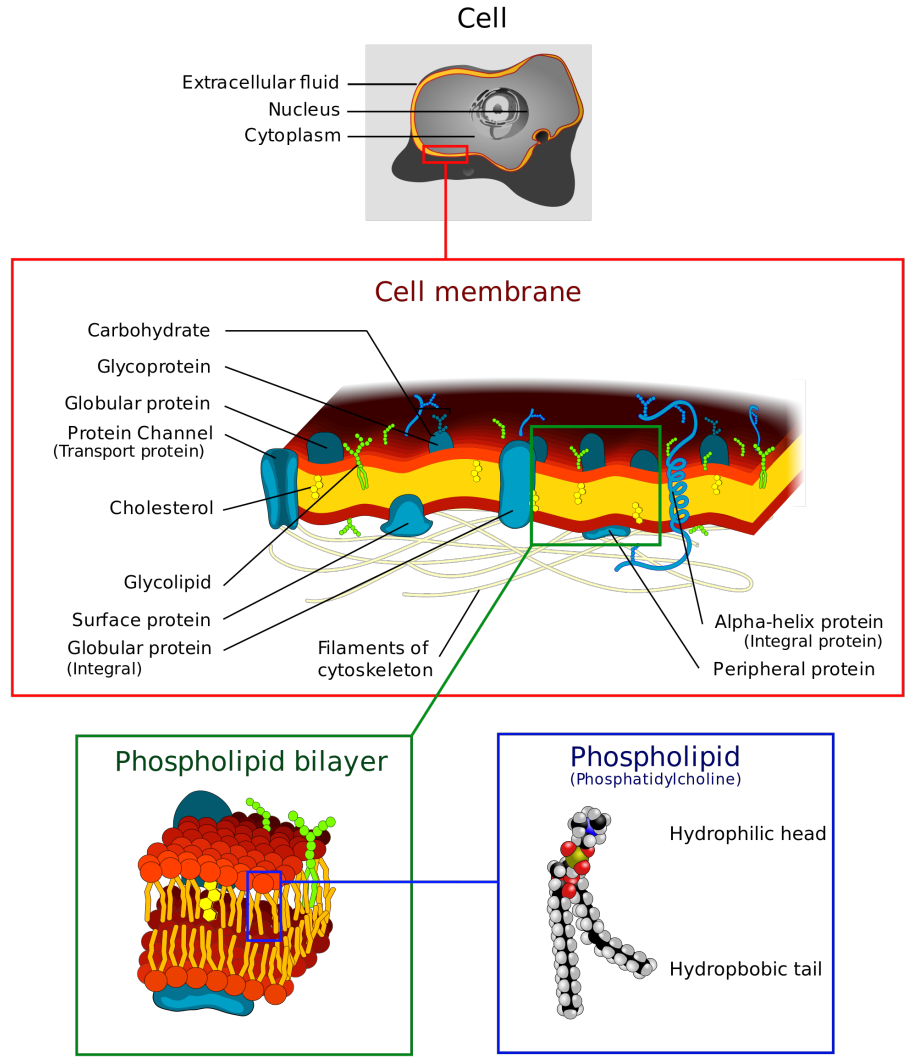

Figure 3.1: A top-down illustration of a cell, its membrane and the constituents of the membrane; a cell is defined by and separated from its environment by a phospholipid bilayer of around 5 nm thickness. Within this membrane, several biochemical compounds are either solved or reach through it. Most important of those are proteins with various functions amoung which are adhesion and interaction with the cell's surroundings. Image from WebSource02 (2013).

(Singer and Nicolson (1972)). This model suggests, that proteins are embedded into the membrane via the same mechanism as the membrane tends to self-assembly. Hydrophobic parts of the proteins are dissolved in the region, where the fatty acid chains are, in the middle of the bilayer structure. Polar/inonic (and therefore hydrophilic) parts of the proteins reach out of the membrane (cf. Fig. 3.2). This ensures a stable integration into the 2-dimensional membrane

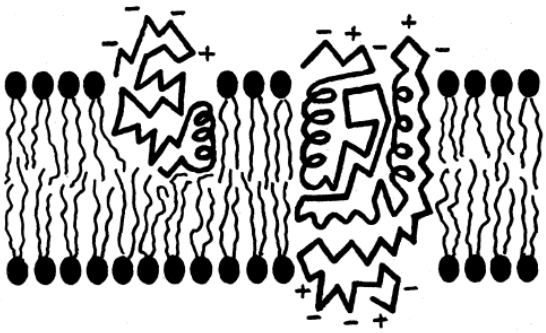

Figure 3.2: Illustration of the anchoring of proteins in a cell membrane. Hydrophobic parts of a protein are located next to the phospholipids of the membrane, hydrophilic parts reach out of the membrane either on one or two sides; figure taken from Singer and Nicolson (1972).

which again is confined only due to solubility effects. Although cells own proteins that specifically serve for adhesion purposes (e.g. integrins), in the later on discussed cases where adhesion on non-biological surfaces will be regarded, any protein reaching out of the membrane contributes only by sheer surface and therewith connected forces which is regarded closer in the following sections.

3.2 Theoretical approaches to cell adhesion

In general cell adhesion is described by two kinds of interactions, so-called specific and non-specific interactions. Specific interactions, also called key-lock-interactions or more scientifically, receptor-ligand-interactions, are interpreted as geometrically matching protein structures. These interactions are very strong with binding energies around 10 $k_{\mathrm{B}}T$ with a typical range in the order of 10 nm (cf. Goennenwein et al. (2003) and Sackmann (2006)). A nice overview on the present state of the biophysical picture of specific cell adhesion processes can be found in Schwarz (2015). These interactions can only occur when two biological entities are involved in the adhesion process. In the case of adhesion on non-biological surfaces consisting of e.g. titanium or diamond-like-carbon as regarded later on in the present work, only non-specific interactions occur. The forces involved add distance-dependent attractive as well as repulsive contributions, which leads to energetic minima with respect to the distance of the two adhesion partners. Given the entropic, fluctuating behaviour in particular of the membrane and trans-membrane polymers, the distance fluctuates and may even undergo larger, but quick changes due to transitions between local minima. Typical distances between substrate and adhering cells (resp. model cell systems) are between 20 and 60 nm (cf. Marx et al. (2002), Sackmann (2006)

and Fig. 4.51). The effects dominating cell adhesion on non-biological surfaces are presented deeper in the following sections.

3.2.1 Attractive interactions

As all adhesion phenomena discussed in this thesis take place in liquid media (either water or cell culture medium), hydration forces are one of the most obvious generic (unspecific) forces one would think of. They originate from the dipole structure of water and occur between two surfaces which are very close together. Nonetheless, hydration forces are of extremely short-range character ($\sim$ a few molecular layers) and are therefore negligible in the regarded systems where various surface proteins lead to distances of several ten nanometers as described above (cf. also Lorz (2003)). Further on, electrostatic forces as a general phenomenon occur, as cell membranes are usually negatively charged. But again, they only contribute a negligible force as they are very effectively shielded by ions in the solution and the Debye length, which is a measure for the range of the force, is significantly smaller than 1 nm as is known from the so-called Gouy-Chapman theory (cf. Israelachvili (2010)). Nonetheless, electrostatics are of importance in terms of small membrane parts or polymer parts that closely reach the surface and build up attractive forces due to permanent and spontaneous dipoles which is well-known as Van-der-Waals-interactions. Further on, gravitation appears to be the second force that governs cell adhesion as a generic interaction. An alternative, less microscopic approach to cell adhesion will be presented in terms of a wetting analogon.

3.2.1.1 Gravitation

Since the density of cells is slightly higher than that of water or cell culture medium, cells are subject to the gravitational acceleration g resulting in a net force F acting on them:

$$F = \Delta\rho V_{\text{cell}} g$$

with V_{cell} being the volume of the cell and $\Delta\rho$ being the difference in densities of the cell and its surrounding medium.

3.2.1.2 Van-der-Waals-interactions

Van-der-Waals-interactions (VdW) generally occur when either objects or surfaces get close to each other. They state a summarization of various electrostatic effects that originate either in permanent or spontaneously (fluctuation-based) emerging dipoles. VdW-forces for two single molecules exhibit a r^{-6}-dependent magnitude. For a membrane of thickness d and an infinite plane in distance h, the VdW-potential has the following shape:

$$V_{VdW} = -\frac{A_{\text{H}}}{12\pi}\left(\frac{1}{h^2} - \frac{1}{(h+d)^2}\right) \tag{3.1}$$

where A_{H} is the Hamaker constant which depends on the ionic surroundings in the solution, but is estimated to be in the order of magnitude of $k_{\text{B}}T$ in various publications (cf. Guttenberg (2001), Lorz (2003) and Goennenwein (2003)).

3.2.1.3 Wetting

A somehow more "macroscopic" approach to cell adhesion, which tries to overcome all these very microscopic effects which *practically* in detail are not accessible, is the description of cell adhesion in terms of a wetting process. This approach starts with the consideration of a water droplet on a given surface. The contact angle Θ_C of the droplet with the surface will be governed basically by the surface tensions σ_{ij} at the different interfaces (cf. Fig. 3.3). Therefore,

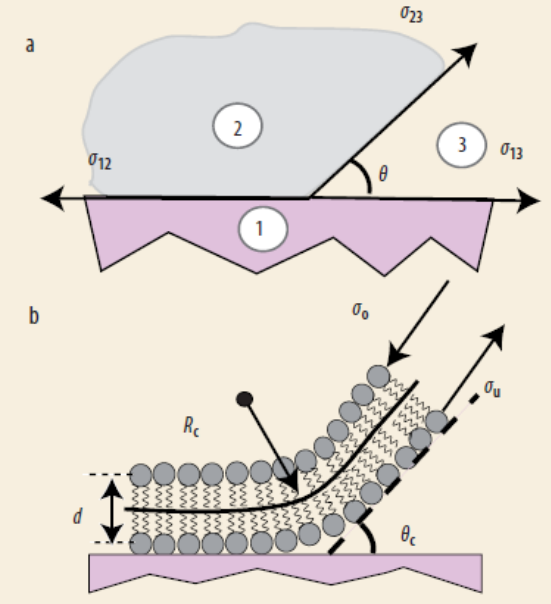

Figure 3.3: Upper part (a): illustration of a water droplet (2) adhering on a solid surface (1). The contact angle Θ_C is defined by the different surface tensions σ_{ij} between droplet, surface and environment (3); lower part (b): at the very edge of the contact between the cell and the substrate, there occurs the contact angle Θ_C which is connected with the contact curvature R_C; image taken from Sackmann (2006).

one obtains:

$$\sigma_{12} = \sigma_{13} + \sigma_{23}\cos\Theta_C \tag{3.2}$$

which finally leads to the following equation for the adhesion energy W, also known as Young's law:

$$W = \sigma_{23}(1 - \cos\Theta_C) \tag{3.3}$$

This consideration so far can be done in exact the same manner for a cell. In case of an adhering cell, the adhesion energy that is released is necessary for the deformation and therefore curvature of the membrane that is connected with the adhesion process. Taking the bending modulus κ of the membrane into account, one finally obtains:

$$W = \frac{\kappa}{2R_C^2} \tag{3.4}$$

In case of a non-biological surface, the typically discussed (strong) receptor-ligand interactions cannot occur as the substrate does not offer components

for these discussed key-lock-mechanisms. Therefore, the balance of adhesion energy (equation 3.3) and bending energy (equation 3.4) should govern the whole process. The beauty of this approach lies in the fact, that all necessary physical parameters are *experimentally* accessible. R_C and Θ_C can be gained by optical means and κ due to flicker analysis (cf. e.g. Sackmann and Bruinsma (2002), Sackmann (2004) and Sackmann (2006)).

3.2.2 Repulsive interactions

There occur two important interactions in unspecific cell adhesion which both are of entropic character, one connected with proteins, the other one with the cell membrane itself.

3.2.2.1 Polymer-induced forces

Although proteins reaching through or on top of the membrane are incapable of forming receptor-ligand-interactions (specific binding), they still are present which might interfere with the adhesive process as the proteins state a steric obstacle and might have to be compressed against their extension they would have in a relaxed state. For the sake of an impression, there shall be shown the repulsive potential that was derived in Bruinsma et al. (2000) for polymers with a surface concentration σ_0 on a membrane:

$$V_{\mathrm{rep}}(h) = k_{\mathrm{B}}T\sigma_0 \left[1 - \exp\left[-\frac{\pi^2}{6}\left(\frac{R_{\mathrm{G}}}{h}\right)^2 \exp\left[-1.5\left(\frac{h}{R_{\mathrm{G}}}\right)^2\right]\right]\right] \tag{3.5}$$

with R_G as the radius of gyration, a measure for the polymer extension (cf. de Gennes (1979)). In particular, attention shall be drawn on the fact, that for low distances of a given cell to the substrate ($h << R_G$), the potential becomes

$$V_{\mathrm{rep}}(h) = k_{\mathrm{B}}T\sigma_0 \tag{3.6}$$

which impressively shows the entropic character of this repulsion.

3.2.2.2 Helfrich undulations

Besides the proteins hindering of adhesion, the membrane itself exhibits also a thermodynamically induced behavior that counteracts adhesion. As already mentioned in part 3.2.1.3 where wetting phenomena are discussed, the membrane undergoes deformations which are connected with its bending modulus κ. This states a thermodynamic degree of freedom where - following the equipartition theorem - $\frac{1}{2}k_{\mathrm{B}}T$ of energy is stored. The derivation of the interaction potential per area V_{HE} regards the fixed mean spacing $\langle h \rangle$ by an external constraint which in the case of cell adhesion would be the typical distance between substrate and cell membrane as within this distance, the undulations can take place. The derivation leads to:

$$V_{\mathrm{HE}}(\langle h \rangle) = 0.116\frac{(k_{\mathrm{B}}T)^2}{\kappa \langle h \rangle^2} \tag{3.7}$$

as a further repulsive component (cf. Marx et al. (2002)).

3.3 Polymer physics - The Freely-Jointed-Chain-model

A very fundamental (and oversimplified) approach to describe the physics of a polymer is the Freely-Jointed-Chain-model (FJC-model). In the FJC-model, we assume a polymer to consist of N identical units of length b, therefore, of total length or contour length of $L_C = Nb$. The single units themselves are rigid. They are connected completely statistically which includes the (unrealistic) possibility of several units occupying the same point in space. Therefore, their orientation $\vec{r}_n$ follows a random walk which leads to an end-to-end vector $\vec{R}$ of

$$\vec{R} = \sum_{n=1}^{N} \vec{r}_n \tag{3.8}$$

and a mean end-to-end distance of

$$\left\langle \vec{R} \right\rangle = 0 \tag{3.9}$$

as the highest probability for a random walk is to end up at the initial point again. Therefore, a more suitable way to describe the size of a polymer is to regard the occupied space R_0 which is described by the standard deviation of the end-to-end vector

$$\left\langle \vec{R}^2 \right\rangle = \sum_{n,m=1}^{N} \langle \vec{r}_n \vec{r}_m \rangle = \sum_{n=1}^{N} \left\langle \vec{r}_n^2 \right\rangle = Nb^2 = R_0^2 \text{ with } b = |\vec{r}_n| \tag{3.10}$$

and therefore

$$R_0 = \sqrt{N} b \tag{3.11}$$

which shows us, that the size of a polymer grows with the square root of the number of its monomers.

Although the mean end-to-end vector $\left\langle \vec{R} \right\rangle = 0$ (equation 3.9), $\vec{R}$ follows a probability distribution. As the orientation of the monomers is governed by a random walk, the probability for the end-to-end vector $P_N(\vec{R})$ to obtain a certain value is gaussian distributed and becomes:

$$P_N(\vec{R}) = const. \cdot \exp(-\frac{3\vec{R}^2}{2Nb^2}) \tag{3.12}$$

with *const.* being a normalization constant.

Following the famous law formulated by Ludwig Boltzmann $S = k_\mathrm{B} \ln \Omega$ which gives us a connection between the microscopic configuration of a system and its entropy (which will be discussed in far more depth in the next section), we can calculate the entropy of a FJC-model polymer chain as

$$S(\vec{R}) = k_\mathrm{B} \ln(const. \cdot \exp(-\frac{3\vec{R}^2}{2Nb^2})) = -\frac{3k_\mathrm{B}\vec{R}^2}{2Nb^2} + const. \tag{3.13}$$

As any extension of the polymer is connected with less feasible microscopic configurations of the monomers, the entropy decreases with increasing extension of the molecule. This can be understood in a more quantitative way regarding

the free energy of a polymer $F = E - TS = -TS$ where E can be disregarded as the interaction of the monomers does not contain any energy (cf. the atoms of an ideal gas), therefore the free energy becomes

$$F = \frac{3k_{\mathrm{B}}T\vec{R}^2}{2Nb^2} \tag{3.14}$$

and the force $\vec{f}$, which is necessary to stretch the molecule is obtained by:

$$\vec{f}(\vec{R}) = \frac{\partial F}{\partial \vec{R}} = \frac{3k_{\mathrm{B}}T}{Nb^2}\vec{R} \tag{3.15}$$

This equation gives rise to the formulation of the "entropy spring"-behaviour of polymers as a comparison with Hooke's law $F = kx$ shows, that the "spring constant" k of a polymer is

$$k = \frac{3k_{\mathrm{B}}T}{Nb^2} \tag{3.16}$$

and therefore of purely entropic nature as it scales with $k_{\mathrm{B}}T$. Although this is a very simplifying and basic model with many shortcomings, it still describes some fundamental properties of polymers like e.g. the phenomenon of rubber elasticity, which is observed when a string of rubber is held under strain. If then the ambient temperature rises, the string will either shrink or more external force will be necessary to keep up the same elongation of the string. This derivation is inspired by and follows closely the one given in de Gennes (1979) where also more sophisticated polymer theories are presented. Nonetheless, the FJC-model will be sufficient to retrace the later on presented ideas.

3.4 A thermodynamic approach to biology

The hitherto presented theories, both on cell adhesion as well as polymer physics, state microscopic points of view. Starting from the smallest units of a system, they try to predict the behaviour of the whole system. Therefore they represent a reductionistic approach to science which is in danger of missing properties that emerge only due to the interactions within the whole system in the sense of Aristotle's famous "... the totality is not, as it were, a mere heap, but the whole is something besides the parts ..." (cf. Book VIII from Aristotle, cf. WebSource01 (2013)). Avoiding this problem and put into a more scientific language, Einstein advocates the idea of observing the whole system and only *concluding from the macroscopic observation to microscopic properties* like he e.g. does in his "*Theorie der Opaleszenz von homogenen Flüssigkeiten und Flüssigkeitsgemischen in der Nähe des kritischen Zustandes*" (Einstein (1910)). This is known as Einstein's reversion, a term which was originally coined by Erwin Schrödinger (cf. Schrödinger (1985)). In particular, the strength of thermodynamics lies in its macroscopic, purely phenomenological character and the fact, that it is based only on very few assuptions which made Einstein comment on it:

> A theory is the more impressive the greater the simplicity of its premises is, the more different kinds of things it relates, and the more extended is its area of applicability. Therefore the deep impression which classical thermodynamics made upon me. It is the

> only physical theory of universal content concerning which I am convinced that, within the framework of the applicability of its basic concepts, it will never be overthrown (for the special attention of those who are skeptics on principle).
>
> Quoted from Schilpp (1970)

It was Konrad Kaufmann who (re-)formulated a lot of these ideas in the recent decades and in particular introduced the idea of proper 2D interfacial entropy (cf. e.g. Kaufmann et al. (1989), where this concept is applied to lipid bilayers). As biological processes to a large extent take place at interfaces, he predicted that interfacial entropy should govern various biological phenomena like e.g. nerve pulse propagation and enzyme kinetics. Based on and inspired by these ideas, several fruitful experiments were conducted recently, e.g. lipid monolayer experiments as possible models for nerve pulse propagation (cf. Griesbauer et al. (2009), Steppich et al. (2010), Griesbauer et al. (2012a), Griesbauer et al. (2012b) and Fichtl et al. (2016)) and experiments on enzyme kinetics (cf. Nuschele (2010), Schneider (2010) and Fichtl (2015)). In the following, a short introduction into this thermodynamic approach to biology and a brief derivation is presented.

3.4.1 The first and second law of thermodynamics

The first law of thermodynamics states the conservation of energy:

$$dE = \delta Q + \delta W \tag{3.17}$$

with E representing the inner energy of a system, Q the heat and W the work. The second law gives a link between the heat Q and the entropy S of the system. The most general formulation of the second law is

$$\Delta S \geq 0 \tag{3.18}$$

For reversible processes, equation 3.18 becomes

$$dS = \frac{\delta Q}{T} \tag{3.19}$$

where T is the temperature of the system.

3.4.2 Entropy as a potential

In the following, we will regard an isolated system, which means, that the inner energy E of the system is constant and that no work W is performed by or due to the system. Therefore, $dE = 0$ and $\delta W = 0$. Together with the first and second law (equations 3.17 and 3.19), we obtain

$$\delta Q = 0 = TdS \tag{3.20}$$

Rudolf Clausius showed in his fundamental article "*Über verschiedene für die Anwendung bequeme Formen der Hauptgleichungen der mechanischen Wärme-*

theorie" where he also introduced the term "Entropie", that entropy is a function of state for systems in which only reversible changes occur (cf. Clausius (1865)). This leads to the formulation of

$$\oint dS = \oint \frac{\delta Q}{T} = 0$$

and allows us to develop entropy as a function of the variables since entropy is an analytical potential:

$$S = S(n_1, n_2, n_3, \ldots) = S_0 + \sum_i \frac{\partial S}{\partial n_i}\delta n_i + \sum_{i,j} \frac{1}{2}\frac{\partial^2 S}{\partial n_i \partial n_j}\delta n_i \delta n_j \tag{3.21}$$

with n_i being thermodynamic observables like e.g. particle number, the (generalized) volume (e.g. area, length for lower dimensional systems), the reaction coordinate of a chemical reaction or internal energy. A closer look on the differ-

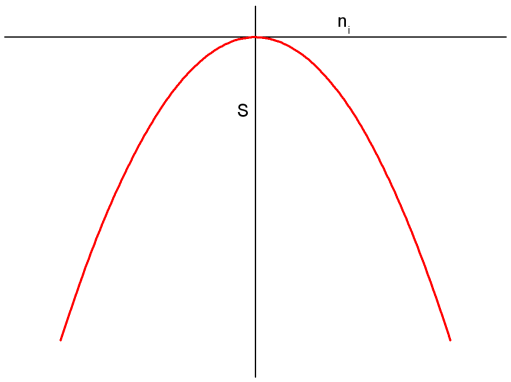

Figure 3.4: Illustration of the parabolic entropy potential.

ent parts of equation 3.21 gives insight into the system in thermal equilibrium, but it even allows to understand dynamics in an isolated system. Further on it provides a reasonable description of a system in a "non-equilibrium" state which is a vividly discussed topic nowadays (which is evident as there is even a specific "Journal of Non-Equilibrium Thermodynamics" by De Gruyter). The part $\sum_i \frac{\partial S}{\partial n_i}$ describes thermodynamic forces, that drive the system into equilibrium. Close to maximum entropy, the first derivatives vanish and the system is in thermal equilibrium. The part $\sum_{i,j} \frac{1}{2}\frac{\partial^2 S}{\partial n_i \partial n_j}$ describes thermodynamic fluctuations. Their intensity depends on the (inverse) curvature of the potential and they persistently take place, no matter which micro-states are realized in a given case. Interestingly, time does not occur in these equations, nevertheless, one can introduce time which is of practical importance since an experimenter is necessarily bound to perform his/her measurements *in time*. Lars Onsager

published the fundamental ideas for that approach in 1931 (cf. Onsager (1931)). Starting with the phenomenological observation, that the entropy of an isolated system beeing not in thermal equilibrium will increase in time, we introduce the entropy production σ defined by

$$\sigma := \frac{dS}{dt} > 0 \tag{3.22}$$

With S depending on several variables n_i in the most general case (cf. equation 3.21), we obtain

$$\frac{dS}{dt} = \sum_i \frac{\partial S}{\partial n_i}\frac{\partial n_i}{\partial t} \tag{3.23}$$

Here, we can identify the thermodynamic forces $\frac{\partial S}{\partial n_i}$ from equation 3.21 and the term $\frac{\partial n_i}{\partial t}$ which describes the development of the observable n_i in time (thermodynamic fluxes in Onsager's nomenclature). Together with the idea of a thermodynamic potential, we see that the slope of the potential (=the forces $\frac{\partial S}{\partial n_i}$) is "scaled" with the fluxes which means, that steeper slopes coincide with both, higher thermodynamic forces and a faster entropy production rate. This equivalence is quite obvious as it shows that a higher entropy production respectively higher thermodynamic forces both lead to a faster thermodynamic equilibration. This also gives insight into the nature of fluctuations. The steeper the slope of the potential, the smaller the inverse curvature of the potential and therefore the smaller the fluctuations. This approach is in particular of great importance in a novel description of enzyme kinetics which is e.g. discussed in Nuschele (2010) and Schneider (2010).

Ludwig Boltzmann formulated the connection between the macroscopic measure of entropy S and microscopic states:

$$S = k_\mathrm{B}\ln\Omega \tag{3.24}$$

Ω denotes here the number of feasible microscopic states that are in accordance with the macroscopic state. In Einstein's appreciation of physics (Einstein's reversion), one is able to obtain information about the microscopic states. But instead of a pretense of knowledge about the microscopic physical reality which is necessarily connected with a complete atomistic or microscopic theory of e.g. $\mathcal{O}(N_\mathrm{A})$ interacting particles, one is bound to obtain information about the macroscopic observables of the system (in particular S). Einstein questions in Einstein (1910) whether Boltzmann's principle is *of any sense* without a *complete molecular-mechanistic* theory and continues that it *lacks of content from a phenomenological point of view*[1].

Equations 3.21 and 3.24 together lead to:

$$\Omega = \exp\left(\frac{1}{k_\mathrm{B}}(S_0 + \sum_i \frac{\partial S}{\partial n_i}\delta n_i + \sum_{i,j}\frac{1}{2}\frac{\partial^2 S}{\partial n_i \partial n_j}\delta n_i \delta n_j)\right) \tag{3.25}$$

In the case of thermodynamic equilibrium, which means that entropy S is maximized with respect to all thermodynamic observables n_i

$$\frac{\partial S}{\partial n_i} = 0$$

[1] Translation by AH

one obtains:

$$\Omega = \exp\left(\frac{1}{k_\mathrm{B}}(S_0 + \sum_{i,j}\frac{1}{2}\frac{\partial^2 S}{\partial n_i \partial n_j}\delta n_i \delta n_j)\right) \tag{3.26}$$

In systems in thermal equilibrium, there still occur small fluctuations $\delta n_i \delta n_j$. The inverse curvature of the system is related to the statistical mean of the fluctuations via (cf. e.g. Steppich et al. (2010) and Landau and Lifshitz (1980))

$$\langle \delta n_i \delta n_j \rangle = -k_\mathrm{B}\left(\frac{\partial^2 S}{\partial n_i \partial n_j}\right)^{-1} \tag{3.27}$$

and is therefore an estimator for the probability of certain states to occur. In particular, that means that any microstate Ω_i constituting the thermodynamic potential S will necessarily occur, even if it constitutes a "non-equilibrium state". Only its probability and lifetime might be of negligible magnitude. Fig.

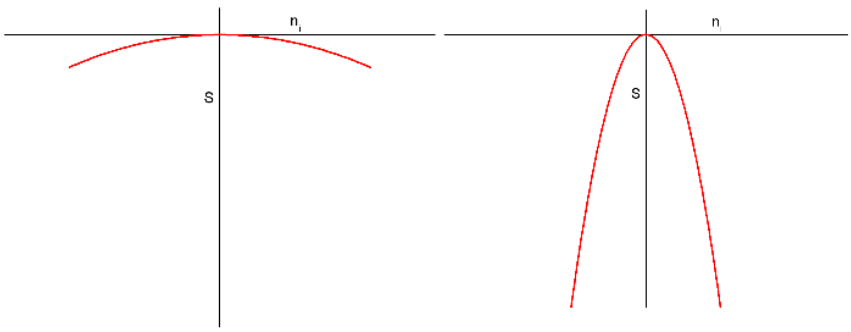

Figure 3.5: Illustration of two different curved entropy potentials. The left (wide) potential represents a situation with high fluctuations, e.g. like a lipid monolayer in its phase transition regime whereas the right (narrow) potential represents a situation with low fluctuations like e.g. a lipid monolayer far away from its transition regime.

3.5 shows two entropy potentials with different curvatures and slopes. For the system in Fig. 3.5 on the left one would expect large fluctuations and low thermondynamic forces. On the right side, the thermal fluctuations are small and large forces appear. These two parabolas could represent e.g. the entropy potentials of lipid monolayers at different ambient temperatures. The left parabola would represent the monolayer in its phase transition regime whereas the right side would be representative for the conditions within the fluid phase (cf. e.g. Wunderlich et al. (2009)). This will be elaborated in more detail in the following.

3.4.3 Measuring the entropy parabola

Following the logic of Einstein's reversion of the second law of thermodynamics, the only way to exploit it, is to measure the thermodynamic behaviour of the macroscopic system. The entropy parabola (and in particular its curvature) is experimentally accessible via observables using equation 3.27. For the above

given example of lipid monolayers, where this theory was already applied very successful (cf. e.g. Griesbauer et al. (2009), Steppich et al. (2010)), one e.g. obtains:

$$\left\langle \delta S^2 \right\rangle = k_{\mathrm{B}} c_\pi \tag{3.28}$$

and

$$\left\langle \delta A^2 \right\rangle = A k_{\mathrm{B}} T \kappa_T \tag{3.29}$$

with c_π being the isobaric heat capacity and κ_T being the isothermal compressibility of a lipid monolayer. Therefore, by measuring macroscopic parameters like c_π, T, A and κ_T, one can obtain microscopic information like area fluctuations δA *without* the initial assumption of a microscopic theory and even the shape of the entropy potential S which can be derived from the entropy fluctuations δS. For example, in the case of a lipid monolayer, the isothermal compressibility κ_T can be obtained via the following equation:

$$\kappa_T = -\frac{1}{A} \frac{\partial A}{\partial \pi}\bigg|_T \tag{3.30}$$

Following this approach and scaling it down to one dimension, which e.g. would be the case for a protein, one obtains:

$$\kappa_T = -\frac{1}{L} \frac{\partial L}{\partial F}\bigg|_T \tag{3.31}$$

Therefore, this is a possible approach to gain insight into microscopic properties resp. microstates via macroscopic means. A further possibility to obtain information about the entropy potential is to measure the lifetime τ of different states (which can can be interpreted as different microscopic configurations) of a system. Although the second law of thermodynamics is time-independent, via Onsagers approach, temporal observations become meaningful (cf. equation 3.23). In particular, a system in thermal equilibrium and therefore at the entropy maximum is still subject to small fluctuations. For a long term observation of duration T_∞, the lifetimes τ_i of the different states are therefore proportional to the probability $p(\Omega_i)$ for the system to occupy a certain state Ω_i.

$$p(\Omega_i) = \frac{\tau_i}{T_\infty} \propto \tau_i \propto \left(\frac{\partial S}{\partial n_i} \right)^{-1} \tag{3.32}$$

Equation 3.32 therefore enables one to reconstruct the entropy parabola and to assign certain microstates to certain positions on the parabola. From this perspective, there is no principal difference between the "lifetime of states" and the "relaxation time" of states if an experimentor prepared an unlikely state and measures the time until the system is in thermal eqilibrium (therefore, occupies mostly states around maximum entropy). This gives also insight into the term of "non-equilibrium" as it is reduced to an unlikely state of the system.

A very demonstrative experiment for the connection of the lifetime of states and the entropy parabola is published in Wunderlich et al. (2009). The gradient of the entropy parabola is obtained by differential scanning calorimetry. In the phase transition region, where area fluctuations δA are strongest, so-called black lipid membrane experiments (cf. e.g. Winterhalter (2000)) reveal a higher electric conductance of the membrane. This conductance is quantified and therefore interpreted as pores, that spontaneously emerge due to

the fluctuations. These are the microstates in the upper introduced terminology. From equations 3.21 and 3.32 follows, that due to the small slope of the entropy parabola of a system in the phase transition regime, the lifetimes τ of the different microstates should be higher. This could be perfectly confirmed in these experiments. Fig. 3.6 shows the current flowing over a lipd bilayer of a D15PC(1,2-dipentadecanoyl-sn-glycero-3-phosphocholine):DOPC(1,2-dioleoyl-sn-glycero-3-phosphocholine)- mixture of 95:5. The diagram on the left shows the behaviour of the membrane at 33 °C where the membrane is in the fluid state, whereas on the right, the membrane was kept at 31.5 °C which is in the phase transition regime of the membrane. One can clearly observe the longer lifetimes of the cunducting states on the right side. Further on, the quantisation which is observed could be interpreted as defined states that are occupied. These observations at lipid membranes together with the idea of

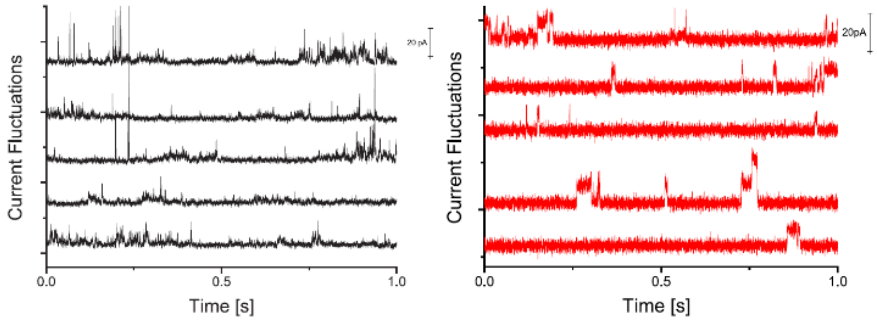

Figure 3.6: Current fluctuations over a lipid bilayer, taken from Wunderlich et al. (2009).

"scaling down" this thermodynamic approach from two-dimensional systems to one-dimensional ones (cf. equations 3.30 and 3.31) were the intellectual starting point for the experiments on the biopolymer von Willebrand factor which are presented in part 4.2. In particular, this approach leads to clear predictions offering the possibility of falsification which in this case are the occurrence of reversible fluctuations of the polymer connected with the necessity of sampling different thermodynamic states.

3.4.4 Gedankenexperiment

To make this so far quite uncommon approach more comprehensible, I will discuss a gedankenexperiment as an example. We assume a cubical box filled with water at standard conditions. At the very top, left, back corner, we position a spot of royal blue ink at $t_{initial} = 0$. From now on we close the box which then can be regarded as a completely isolated system that therefore can be described with an entropy potential like given in equation 3.21. From experience we know that the spot of ink will start to diffuse and after a certain time t_{final} will be completely equally distributed over the volume of the box. Initially, with the ink spot in one corner, the system is in a state that would be labeled "non-equilibrium" in common terms. Nevertheless, this state is *in principle* also reachable in equilibrium via fluctuations and is sampled with a certain probability P. Its number of microscopic possible realizations is only negligible

small in comparison to the huge amout of realizations that generate a more or less perfect equal distribution. Therefore, for practical considerations and in particular for an observer *in time*, the system will sample during $t_{initial} \rightarrow t_{final}$ more and more probable states on the parabola that constitutes the entropy potential until it reaches a close-to ideally equal distribution, where it only undergoes minor fluctuations around the equilibrium point. States further away than δn_i from equilibrium are exponentially suppressed. We will repeat now the very same (gedanken-)experiment under identical conditions except that the box is filled with heavy water (D_2O). The diffusion coefficient is given by

$$D = \frac{k_B T}{6\pi\eta R_0} \tag{3.33}$$

with R_0 being the radius of a spherical object suspended in a fluid and η the dynamic viscosity of the fluid (Einstein (1905)). Since η of D_2O is $\sim 25\%$ higher than of H_2O at standard conditions (Stöcker (2000)), we obtain

$$D_{D_2O} \approx 0.8 \cdot D_{H_2O} \,.$$

For an observer in time, that means that it will take longer until the system is equilibrated. In the picture of the thermodynamic potential, this means that the slope of the parabola is less steep. Therefore, the lifetimes of different microstates are longer (cf. Fig. 3.5). The extensive discussion and illustration of this topic is due to the fact, that although the preceding idea of an entropy potential is already $\sim$ 100 years old, this particular approach has penetrated the scientific community only partially. Further on, especially in part 4.2 and part 4.3 of this thesis, this approach will reveal its powerfulness.

Chapter 4

Results and Discussion

4.1 The De-Adhesion Number Investigator and Cell Adhesion on Implant materials

One major goal of this thesis was the development of a novel system to probe cell adhesion properties on arbitrary implant materials. The comparison with the present-state of cell adhesion probing devices at the beginning of this R&D work revealed several unsatisfying limitations on the experimental conditions and derivable parameters for cell adhesion research, in particular for *practical, applied issues* like material surface characterization for (human) implant research. The most prominent techniques for cell adhesion probing so far are both the spinning-disc method and flow chamber devices. For the spinning disc method, cells are grown on a substrate, kept in medium and a disc is rotated above them. This creates a shear field exerting forces on the cells with a magnitude proportional to the distance to the center of the disc (cf. e.g. Weiss (1961)). A big shortcoming of this method is that is allows only the observation of the initial and the final state of the cell population on the sample, but not its temporal evolution. Flow chambers in contrast are channel-like structures with a high aspect ratio. Via continuous changes of the diameter, interesting flow profile properties can be reached like large shear spectra (cf. e.g. Usami et al. (1993)). These systems are driven by external pumps (e.g. syringe pumps) and therefore necessarily state open systems. This is connected with the requirement of large amounts of lab consumables and the occurrence of sizeable dead volumes.

To overcome these limitations, the related research and development lead to a system called DANI - the De-Adhesion Number Investigator. It is a surface acoustic wave-based, closed microfluidic device which allows live observation of deadhesion experiments at physiological conditions making use of inverted optical microscopy and fluorescent techniques. The developed system will be described in detail in the following. A brief description and a selection of the earliest experimental results gained by the tool can be also found in Hartmann et al. (2013).

4.1.1 Materials and Methods

4.1.1.1 Surface Acoustic Wave driven microfluidics

A central problem to solve was the creation of an entirely closed measuring chamber where surface acoustic wave (SAW) driven microfluidics on an optical transperent chip are of major importance. Surface acoustic waves can be excited on piezo-electric materials (cf. e.g. Lew Yan Voon and Willatzen (2011)). This is performed via comb-shaped electrodes with periodicity p which are also called interdigital transducers (further on IDTs, cf. Fig. 4.1). These electrode structures are created and deposited using photolithography processes and metal deposition in a vacuum chamber. An early fundamental description of the creation and working principle of IDTs can be found in White and Voltmer (1965). These electrodes own a resonance frequency which emerges due to

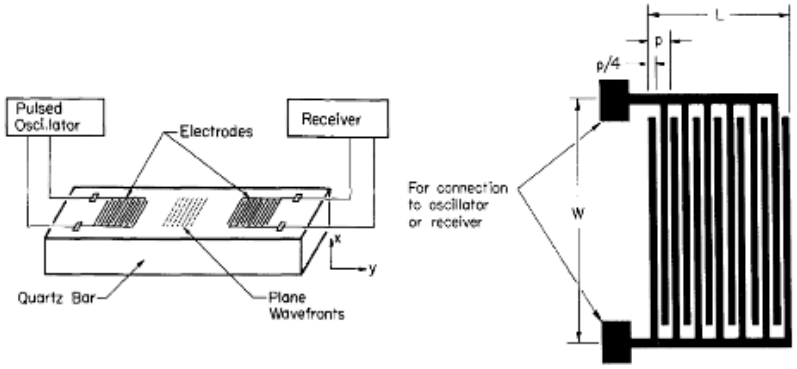

Figure 4.1: Original figures from the pioneering work of White and Voltmer (1965) showing the basic ideas and shape of interdigital transducer structures; left, a complete setup, right, a top view on the interdigital transducer (IDT) structure.

the piezo-electric effect. A voltage pulse applied to an electrode induces a line distortion in the substrate. This distortion propagates with the sound velocity v_{SAW} of the material along the surface and reaches further electrodes of the comb-shaped structure in a distance $\frac{p}{2}$, with $\frac{p}{2}$ being the distance between two opposing electrodes. If the arrival of the mechanical distortion coincides with an identical electrical stimulation , the wave is reinforced. Therefore, if a sine wave is applied to such a comb-structure, the condition for the resonance frequency f_{res} becomes

$$f_{\mathrm{res}} = \frac{v_{\mathrm{SAW}}}{p} \tag{4.1}$$

This principle allows the continuous excitation of surface acoustic waves which can be e.g. exploited for microfluidic purposes.

The application of SAW for microfluidics is a well established method (cf. e.g. Wixforth et al. (2004), Wixforth (2006), Frommelt et al. (2008), Fillafer et al. (2009), Wixforth (2009), Fallah et al. (2010), Friend and Yeo (2011), Schmid et al. (2011) and Ding et al. (2013)) and used either for internal mixing of droplets (acoustic streaming) as well as entire movement of them (SAW streaming, cf. Shiokawa et al. (1989)). Both effects are based on the same

principle of exponential attenuation of the SAW (cf. Fig. 4.2) and differ only in incoupling wave power. Since in the later on presented case, any lateral movement of the liquid is suppressed by geometrical confinement, the general distinction will not apply.

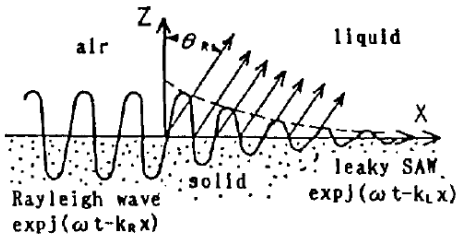

Figure 4.2: Schematic drawing of a SAW reaching an area with a liquid above where it is exponentially attenuated and causes movement of the liquid. The Rayleigh-angle Θ_R describes the direction of the incoupled energy; image taken from Shiokawa et al. (1989).

The angle Θ_R (cf. Fig. 4.2) is called the Rayleigh angle, indicates the angle, under which the microfluidic flow is excited and depends on the sound velocities in the related media:

$$\sin\Theta_\mathrm{R} = \frac{v_\mathrm{liquid}}{v_{\mathrm{LiNbO_3}}} \tag{4.2}$$

with v_liquid being the sound velocity in the liquid (e.g. water or cell culture medium) and $v_{\mathrm{LiNbO_3}}$ the sound velocity in the piezoelectric substrate lithium niobate. For water at 20°C, $v_\mathrm{liquid} = 1483\,\frac{\mathrm{m}}{\mathrm{s}}$, for $LiNbO_3$ rot 128°-Y cut X Prop., as used in the present work, $v_{\mathrm{LiNbO_3}} = 3980\,\frac{\mathrm{m}}{\mathrm{s}}$ (Strobl (2005)). Therefore, in the following systems, we obtain $\Theta_\mathrm{R} = 21,9°$.

An important quantity for the characterization of the fluid systems realized that way is the shear rate $\dot{\gamma}$ as it allows conclusions of the forces acting on the surfaces confining the flow. For Newtonian fluids (which follow the Navier-Stokes-equation) the force per area which is called the shear stress τ becomes

$$\tau = \eta\dot{\gamma} \tag{4.3}$$

with η being the viscosity of the fluid.

The shear rate for a fluid flow with layers of constant velocity (which is the case both in planes and in cylinder surfaces in a pipe flow) becomes

$$\dot{\gamma} = \frac{\mathrm{d}v}{\mathrm{d}z} \tag{4.4}$$

with v being the velocity in the layers and z being the direction perpendicular to the layers which is the height in the case of planes resp. the radius in case of a pipe flow. Using equation 4.3 and neglecting turbulent flow effects that might occur, when adherent cells interact with a laminar flow, the surface of the cell which is exposed to the flow gives at least a first approximation of the forces acting on adherent cells.

As surface acoustic wave microfluidics state a very versatile tool for the manipulation of small amounts of liquids, it became a vital tool for a broad range of biological applications, cf. e.g. Li et al. (2007), Li et al. (2009) and Ding et al. (2012).

4.1.1.2 Realization of DANI

The De-Adhesion Number Investigator DANI is realised as a completely closed microfluidic flow chamber. Its bottom consists of the $LiNbO_3$ substrate, where SiO_2 was sputtered on top for protection and durability issues. A cylindric shaped polydimethylsiloxane (PDMS) body constitutes the side walls. The chamber is closed by the implant material sample that is subject to the cell adhesion investigation (cf. Fig. 4.4). In most cases, a single standard set of parallel IDTs (in the following SIDT, cf. Fig. 4.3) with a resonance frequency of $f \approx 160$ MHz was used; the initial resonance frequency is subject to minor shifts ($\approx 2\%$) due to the initially deposited SiO_2 and residual persistent contaminations that occur as a result of usage.

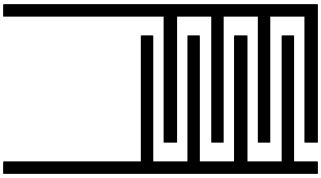

Figure 4.3: Schematic drawing of the standard IDT structure used for the cell deadhesion experiments.

Besides the SIDT, also more sophisticated sets of IDTs and therefore different resulting flow profiles were examined and applied. These IDTs are described closer in section 4.1.2.8. The $LiNbO_3$-chips are glued into a chip-carrier with two conduction copper-areas which are soldered with a SMA-socket (cf. Fig. 4.4). The chip-carrier again is mounted onto a sample holder board which is equipped with micrometer screws to allow fine positioning of the sample and ITDs relative to the view field of the microscope.

4.1.1.3 Implant samples

As a typical medical implant material sample (e.g. for artificial hip joints and dental implants), the medical titanium alloy Ti6Al4V (Ti Gr.5-ELI, purchased at Valbruna Edel Inox GmbH, Dormagen, Germany) was chosen. It is a titanium alloy with 6 wt.% aluminium and 4 wt.% vanadium. Samples were prepared as discs (radius = 5 mm, height = 2 mm) and sandblasted by Aesculap AG, Tuttlingen, Germany, which led to a surface roughness R_a of $\approx 5\mu$m. The samples are pictured in Fig. 4.5. Before useage in experiments, they were ultrasonicated in a bath (50°C, 1:1 aceton/isopropanol) for 20 minutes and sterilized in an autoclave at 121°C for 20 minutes. These samples were used in particular to assess and characterize the novel system in terms of suitable initial adhesion times for the cells and resulting deadhesion rates that provide a reasonable resolution between different systems that are to measure. Beyond characterization of the system, it was also already applied to support advanced implant material development, for instance in order to optimize Ag-doping of diamond-like-carbon (DLC) implant surfaces. DLC is reported to have good biocompatible and tribological properties (cf. e.g. Allen et al. (2001), Thorwarth et al. (2007)). To overcome the problem of postoperative inflammation (cf. Quirynen et al. (2002)), physicists at Experimental Physics IV, Augsburg

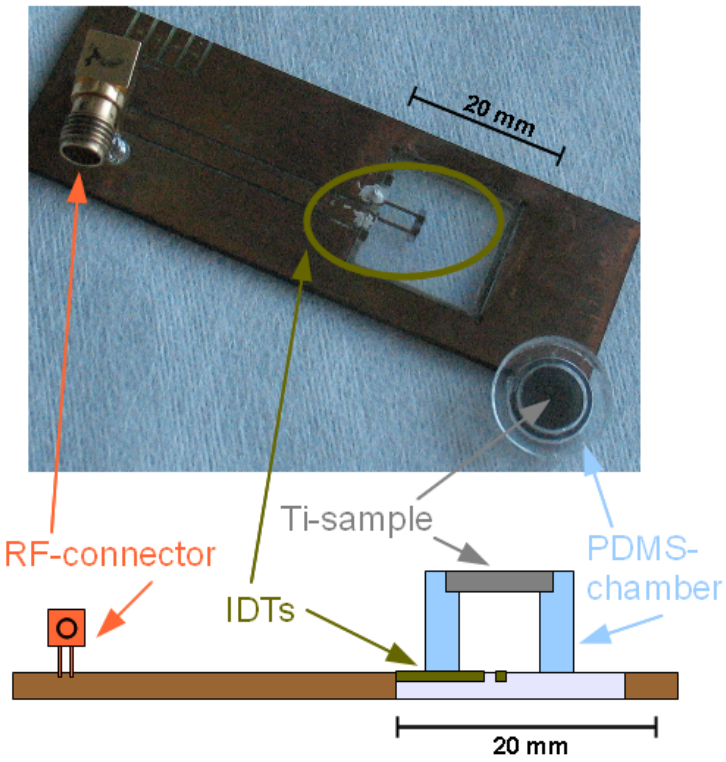

Figure 4.4: Photograph (top) and schematic drawing of the cross section of the sample holder (bottom).

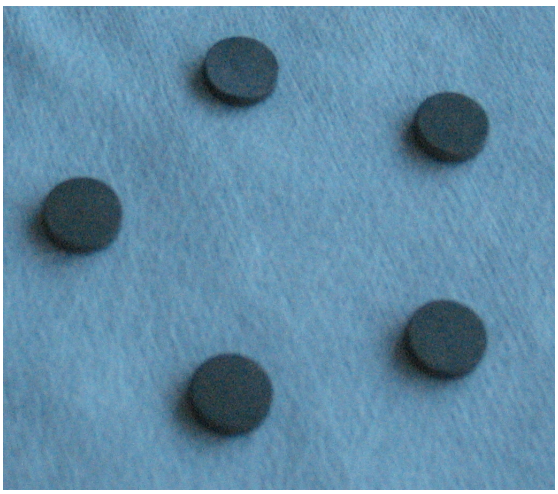

Figure 4.5: Titanium implant samples as used in the present study.

University, Germany, introduce nano-Ag-clusters into a DLC-matrix that coats a Ti6Al4V-surface (Schwarz et al. (2011)) as silver is well-known to exhibit antibacterial properties. Basically, this preparation procedure is based on a dip-coating process of the samples in a polyvinylpyrrolidone ($[C_6H_9NO]_n$, PVP) solution containing colloidal nano-Ag. This solution is based on a precursor solution that contains ethanol, acetone, benzoine and $AgNO_3$. The result for the coating mainly depends on the molar ratio of benzoin:$AgNO_3$ (in this study 1:2) and $AgNO_3$:polyvinylpyrrolidone(PVP), which was adjusted to 1:2, 1:10, 1:20 and pure PVP. In order to transform the PVP-coating into a DLC-matrix, the samples were subject to a plasma immersion ion implantation (PIII) with Ne and CH_4 as processing gases. The details of the preparation and a material characterization can be found in Schwarz et al. (2011). These advanced material samples were tested with DANI in terms of their dynamic cell adhesion behavior and are denoted in the following as "Ag:PVP 1:2", "Ag:PVP 1:10", "Ag:PVP 1:20" and "DLC PVP" for the Ag-free samples. In order to ensure realistic conditions of the samples like they occur with real implants that are applied with patients in clinics, the samples were sterilized according to medical standards. Therefore they were treated with a cobalt 60-source (1.1732 MeV and 1.3325 MeV) using a radiation dose of 26.5 kGy.

4.1.1.4 Measuring procedure and data acquisition

To measure the cell adhesion under flow conditions, the cultivated cells are harvested and suspended in cell culture medium with a density of $\approx 360\text{k}\,\frac{\text{cells}}{\text{ml}}$. For details of the cell culture, cf. Appendix 6.1. As the developed technique is intended to work with arbitrary materials, independent of their optical transparency, the cells are fluorescently stained with 1 μl of calcein green AM (Invitrogen$^{\text{TM}}$, 1 μg dissolved in 1 μl dimethyl sulfoxide) per ml of the cell suspension. Therefore, they are kept in an incubator with cell culture conditions (37 °C, 5 % CO_2) for t $>$ 30 min. In living cells, intracellular enzymes remove the acetoxymethyl-group (AM) and activate by that calcein green as a fluorescent dye (excitation wavelength $\lambda_{\text{ex}} = 470\,\text{nm}$, emission wavelength $\lambda_{\text{em}} = 509\,\text{nm}$ at pH = 7.4, Sigma-Aldrich (2013)). By that, cell viability is proven and detectability ensured. After staining, the suspension is stirred to assure a homogeneous distribution of the cells and $\approx 160\,\mu$l are filled into the inverted chamber. The sample to measure serves as its bottom side and on top, the 160 μl reach the limit of surface tension to keep the droplet cohesive. The sample is put back again into the incubator for an incubation time t_{inc} of typically 60 minutes, for initial gain of experience with the system, a spectrum of incubation times was measured ranging from 10 - 60 minutes. Following a Stokes' law estimate, the sedimentation time of a cell with a radius of 10 μm is $< 1\,min$ for the whole distance from top of the droplet which makes the sedimentation time negligible for practical issues. After the incubation time, the cell medium in the chamber gets exchanged which ensures that only sufficiently strong adhered cells remain on the sample and that there are (nearly) no cells in the suspension when the microfluidic flow is activated. The upside-down setup is then screwed together and mounted on the microscope where is gets connected to the heat bath and the frequency generator. Image acquisition is performed with a "Hamamatsu Orca 5G" camera, a 2.5x-objective and fluorescent light with a blue filter. As calcein green is susceptible to bleaching, the fluorescent

light is covered with a shutter which is only opened for capturing an image. The frequency generator gets switched on after a preparation time of 15 minutes and provides the IDTs with a power of 27 dBm (= 500 mW). Images are taken every 2 minutes for the first 10 minutes, later on every 5 minutes until one hour.

4.1.1.5 Data analysis

Image analysis was performed with "ImageJ" (http://rsb.info.nih.gov/ij/), a free software provided by the National Institute of Health (NIH). ImageJ allows automated recognition of "particles" which are divided apart from each other by contrast gradients. As the cells grow apart from each other as well as in smaller and larger accumulations, a heuristic was introduced to deduce the number of cells within an identified and analysed ImageJ-particle from its size (cf. Tab. 4.1).

# cells	radius (μm)	area (μm^2)
1	5,64 - 12,62	100-500
2	12,63 - 16,92	501-900
3	16,93 - 19,95	901-1250
4	19,96 - 22,57	1251-1600
5	22,58 - 25,23	1601-2000
6	25,24 - 28,21	2001-2500
7	28,22 - 30,90	2501-3000
8	30,91 - 33,37	3001-3500
9	33,38 - 35,68	3501-4000
10	35,69 - 39,89	4001-5000

Table 4.1: Heuristic assumption for the number of cells corresponding to a certain area (and aquivalent radius of a circle with the same area) of an automatically identified "particle".

Each image of a timeseries was processed that way which results in knowledge of the evolution of the cell population on the sample over time (cf. e.g. Fig. 4.12). Exemplarily, an image from the beginning and the end of an experiment (therefore, after 60 minutes of flow exposure) is shown in Fig. 4.6.

4.1.1.6 Characterization of the system - Particle Image Velocimetry PIV

The presented arrangement of DANI was analyzed in respect of its flow profile and the resulting shear rate distribution in particular close to the implant sample surface. Therefore, micro-spheres (diameter 10 μm, Polybeads® from Polyscience Inc., Warrington, PA) were dispersed with 0.2 vol.% in cell culture medium. The obtained liquid was introduced into the chamber and the microfluidic flow was driven under similar conditions (e.g. SAW-power, temperature regulation) as in the cell deadhesion experiments using the micro-spheres as tracer beads. Instead of an implant sample as top of the chamber (like in the cell adhesion experiments), here a glass sample of similar size and shape was used in order to allow the observation of the tracer beads. Their movement was documented taking $\approx$ 200 images with 125 frames per second in several planes

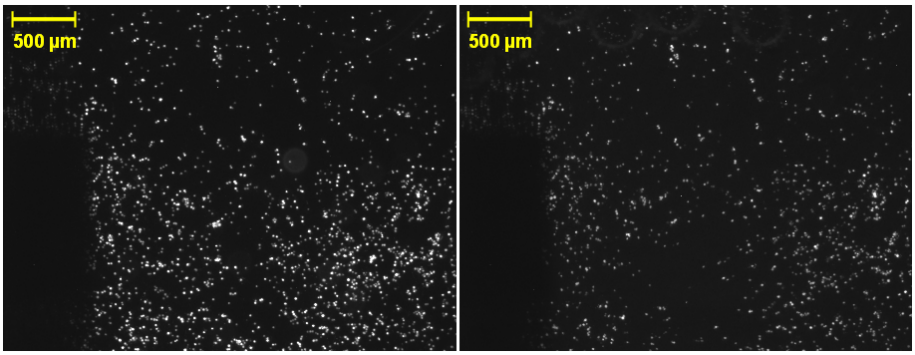

Figure 4.6: The images show a view into the measuring chamber with fluorescently stained SAOS-2 cells on medical titanium before and after 60 minutes of microfluidic flow exposure of the implant sample. To assess the number of cells, the bright areas were analyzed in terms of size using ImageJ and linked to a certain number of cells according to table 4.1.

of the chamber. These movies were taken in $\approx 54\mu$m distance beginning at the sample surface. For bead velocity evaluation, the planes were analyzed using the open source tool PIVlab (developed by Dipl. Biol. William Thielicke and Prof. Dr. Eize J. Stamhuis, provided online: http://pivlab.blogspot.de/; cf. Fig. 4.7). The analysis was performed on a 63 x 63 grid for the view field of the "Photron Fastcam 1024 PCI" camera of 6.963 mm x 6.963 mm. A comprehensive review on this so-called Particle Image Velocimetry (PIV) technique is given in Lindken et al. (2009).

For the SIDT, the flow profile given in Fig. 4.7 about 160 μm below the implant sample was obtained. The SIDT is a single IDT structure (shown in Fig. 4.3). This strucure was used for all cell deadhesion experiments unless differently denoted. The velocity fields of the top three closest planes to the sample ($\approx 0\,\mu$m & $54\,\mu$m & $108\,\mu$m) were processed with the open source software Scilab (http://www.scilab.org/) to calculate the shear rate $\dot{\gamma} = \frac{\mathrm{d}v}{\mathrm{d}z}$ and its distribution among the chamber (cf. Fig. 4.8). The shear-field near the surface exhibits a half-moon shaped geometry with two distinct maxima. The shear rates range from $0- \sim 35\,\mathrm{s}^{-1}$. The geometry originates in the typical flow-excitation characteristics of parallel IDTs which are "butterfly"-shaped with its principal plain rotated by the Rayleigh-angle of 21°(cf. part 4.1.1.1 and Fig. 4.2).

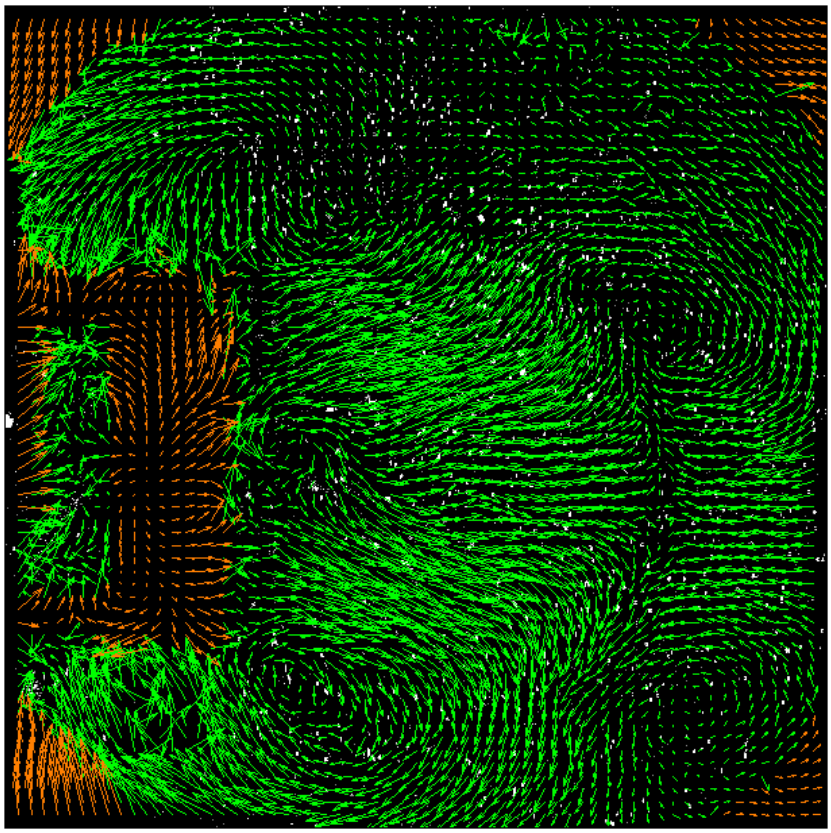

Figure 4.7: Exemplary output of the particle image velocimetry (PIV) analysis of the measuring chamber 160 μm below the sample; the green arrows show the movement of the latex micro-spheres whereas the red arrows constitute artifacts of the PIV analysis. They occur in areas, where there either are no beads as in the four corners, where the circular chamber already has ended or on the left side in the middle, where the view field of the camera is masked due to the IDT structures.

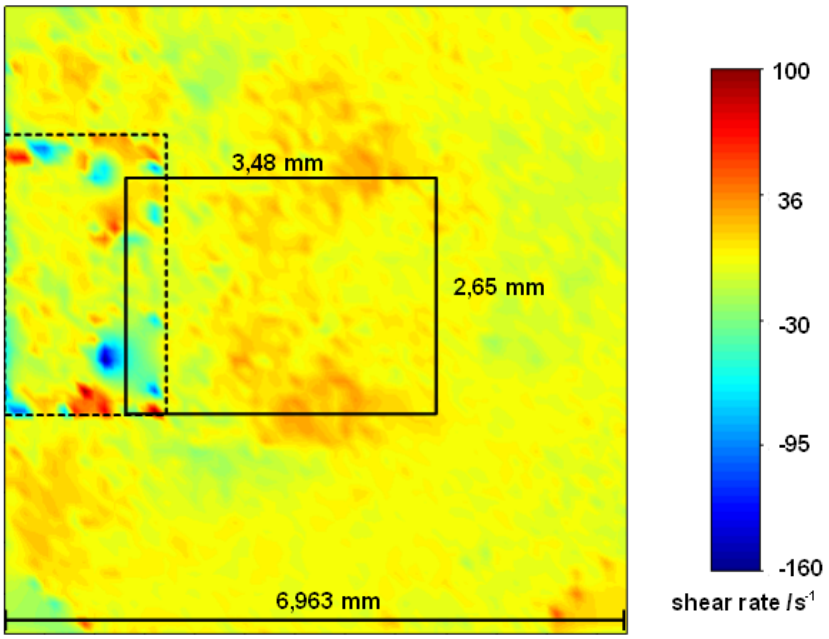

Figure 4.8: Shear rate distribution within the closest $\sim 100\,\mu$m to the implant sample in the DANI system. The shear rates are obtained from the velocity gradients $\dot{\gamma} = \frac{\mathrm{d}v}{\mathrm{d}z}$ of latex micro-spheres analysed via PIV-lab in 3 plaines in $0\,\mu$m, $54\,\mu$m and $108\,\mu$m distance from the sample; the dashed rectangle indicates the area of the IDTs where the PIV analysis creates artifacts; the continuous marked rectangle indicates the area in the chamber which is reached by the view field of the camera for the deadhesion experiments.

4.1.2 Cell adhesion measurements

4.1.2.1 Cell types

Primary human osteoblasts
The first test experiments with the novel developed DANI tool were performed with primary human osteoblasts (HOBs). HOBs were explanted from patients at "Klinikum rechts der Isar", München, Germany and provided by AG Dr. Burgkart. Experiments could be performed successfully as the cells adhered on titanium samples (cf. Fig. 4.9) and could be detached again by the microfluidic flow. Nevertheless, the extensive characterization of the system was performed

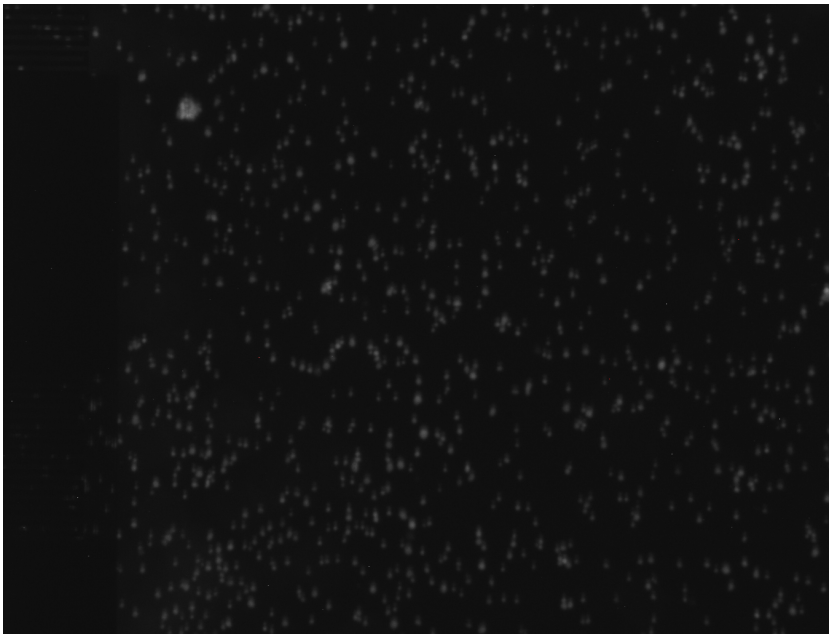

Figure 4.9: Primary human osteoblasts adhered on titanium. On the very left side the metal structures of the IDTs can be identified as the dark, black area.

with a cancer cell line as the cell division of the HOBs was very slow (doubling time $>$ 1 week) until it completely vanished which led to an insufficient supply with cells.

SAOS-2 cell line
A suitable cancer cell line in terms of type, function and cell division rate is the SAOS-2 cell line (cf. Fig. 4.10). It is an osteogenic sarcoma cell type which was obtained in 1973 from an eleven-year-old girl (DSMZ (2013)). It is a very commonly used osteoblast-like cell and regarded as a representative cell for osseointegration studies (cf. e.g. Allen et al. (2001), Okumura et al. (2001), Monsees et al. (2005)).

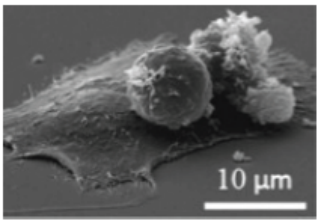

Figure 4.10: A SAOS-2 cell on an amorphous diamond substrate, image taken from Myllymaa et al. (2009).

4.1.2.2 Incubation time dependence of cell adhesion

In order to develop a proper protocol for further cell adhesion measurements with the novel system, the time dependence of cell adhesion and further deadhesion under flow conditions was assessed. Measurements were performed following the procedure described in part 4.1.1.4 with incubation times t_{inc} ranging from 10-60 min. The number of adhered cells increased from 159 - 546 $\frac{\mathrm{cells}}{\mathrm{mm}^2}$ where 1.2k $\frac{\mathrm{cells}}{\mathrm{mm}^2}$ in total were suspeded in the medium (cf. Fig. 4.11). The values are based on five measurements for each incubation time. The different

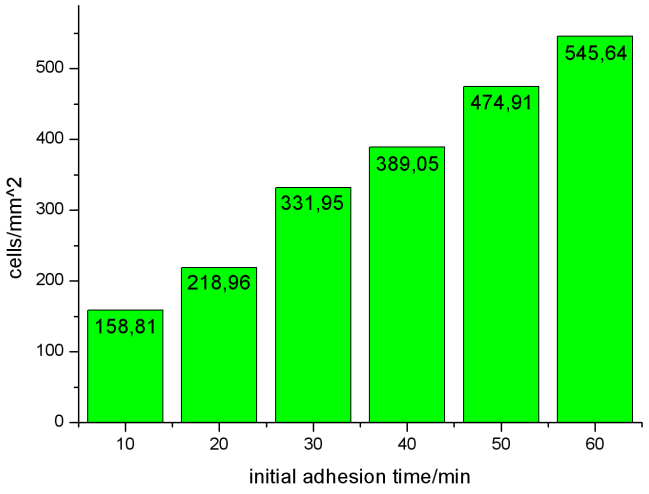

Figure 4.11: Initial adhesion of SAOS-2 cells on medical titanium with different incubation times t_{inc}. In total, 1.2k $\frac{\mathrm{cells}}{\mathrm{mm}^2}$ were suspended in the medium.

Ti samples were subject to measurements with DANI applying a microfluidic flow for 60 minutes (cf. part 4.1.1.4). In accordance with an intuitive guess, the deadhesion rates decreased with increasing initial adhesion times t_{inc} as the cells have more time to establish a stable interaction with the substrate. While for $t_{\mathrm{inc}} = 10$ min of incubation, 21 % of the cells could be detached again after 60 minutes of flow treatment, for $t_{\mathrm{inc}} = 60$ min only 8 % were detached again (cf.

Fig. 4.12). Each value reflects the average of five independent measurements. For further measurements, the protocol was standardized to an incubation time

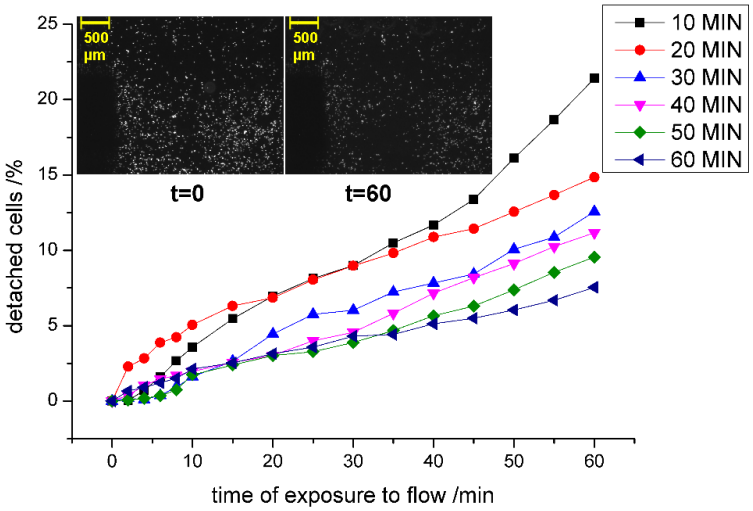

Figure 4.12: Detached cells for different incubation times t_{inc} on medical titanium over time.

t_{inc} of 60 minutes. Further on, the here presented measurements with Ti as a substrate and $t_{\mathrm{inc}} = 60\,\mathrm{min}$ will serve as a reference for various measurements presented further on.

4.1.2.3 pH dependence of cell adhesion

The De-Adhesion number investigator is capable of mimicing physiological conditions due to temperature control and the choice of a proper medium in the chamber. Beyond that, deviations of standard conditions can be realized which is easy in particular due to the small chamber volume. An interesting deviation of standard conditions is for example the change of temperature and pH value, as it is well-known that under conditions of an inflammation, the local pH is lowered and temperature rises. Further on, it is known that the pH value is significantly reduced during the first two weeks after a fracture at the fracture site (cf. Fig 4.13). Therefore, a series of experiments was performed to simulate osseointegration under inflammation conditions which is relevant in terms of implant surgery as inflammation conditions may accompany a surgical intervention. In the sense of a systematic approach, the two deviations from the standard conditions were analyzed independently from each other. In Fig. 4.14 the effect of differnt pH values on initial cell adhesion with $t_{\mathrm{inc}} = 60\,\mathrm{min}$ is shown. One can clearly see the decrease of initial adhesion with further distance from the physiological extracellular values of pH $\approx$ 7.4. Note that the maximum adhesion value shown represents the conditions within a pH spectrum ranging from pH = 7.2 - 8.7. Although the newly purchased medium has a pH of 7.2,

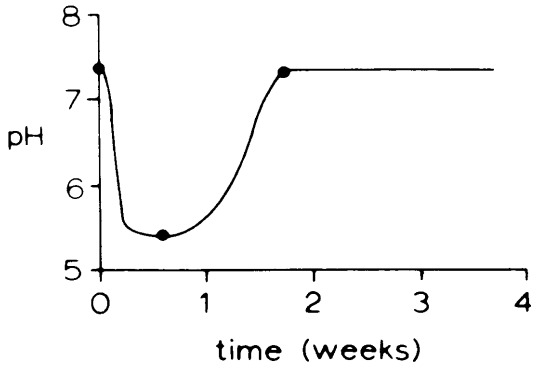

Figure 4.13: The pH of the fracture site versus the time after fracture. Within the first two weeks, the pH value is reduced up to two levels. Image taken from L. L. Hench (1982).

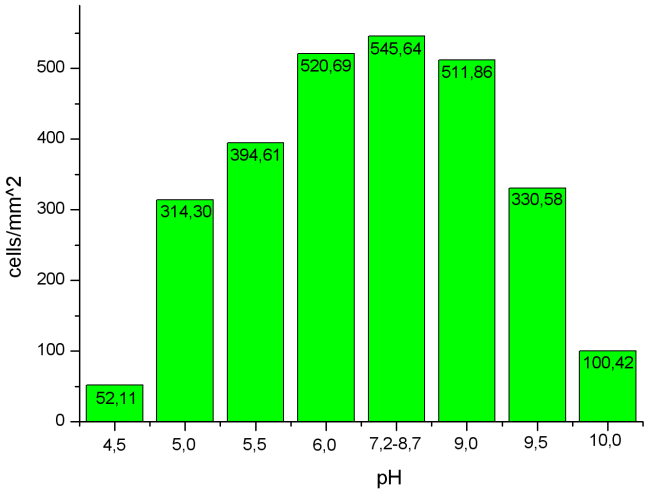

Figure 4.14: Initial adhesion of SAOS-2 cells on medical titanium under different pH values with $t_{\text{inc}} = 60\,\text{min}$. In total, 1.2k $\frac{\text{cells}}{\text{mm}^2}$ were suspended in the medium.

during storage, pH shifts occur. The adjustment of pH values of the medium was done with HCl resp. NaOH (each 3%). The deadhesion rate as well shows an increase with further distance from the physiological pH optimum as one could expect. There is an increase of deadhesion for small deviations from the physiological pH (pH=7.4) into the alkaline regime compared to the acidic regime (cf. Fig. 4.15). Note, that in order to avoid poor statistics, the two extreme cases depicted in Fig. 4.14 (pH=4.5 and pH=10) were omitted as they would have been connected with a very low amount of cells on the sample.

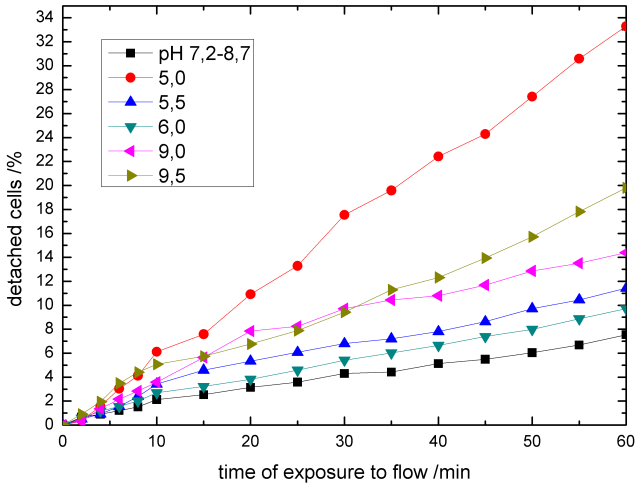

Figure 4.15: Cell detachment upon pH dependence over time. Small deviations from physiological pH=7.4 lead to a more prominent increase of deadhesion in case of alkaline conditions compared to the same deviations into the acidic regime.

4.1.2.4 Temperature dependence of cell adhesion

Besides pH changes, temperature deviations from the human physiological body core temperature (37°C) were addressed. Temperature deviations can occur due to inflammation, fever and also at implants that are due to their position in the body being not at core temperature. Figure 4.16 shows the effect of different temperatures during the adhesion process in the incubator. Interestingly, the affinity of initial adhesion is very robust with respect to temperature decrease. Even with a 10°C lower ambient temperature it decreases less than 10 %. For higher temperatures in contrast, the effect is by far more prominent. Changing temperature from 41°C to 43°C leads to a decrease of initial cell adhesion of more than 36 %. This is probably due to the denaturation of the cell adhesion molecules (e.g. integrins) that are transmembrane molecules that are considered to be responsible for cell adhesion.

In terms of cell deadhesion, one can observe two similar interesting effects. First, optimal adhesion is again connected with physiological conditions and

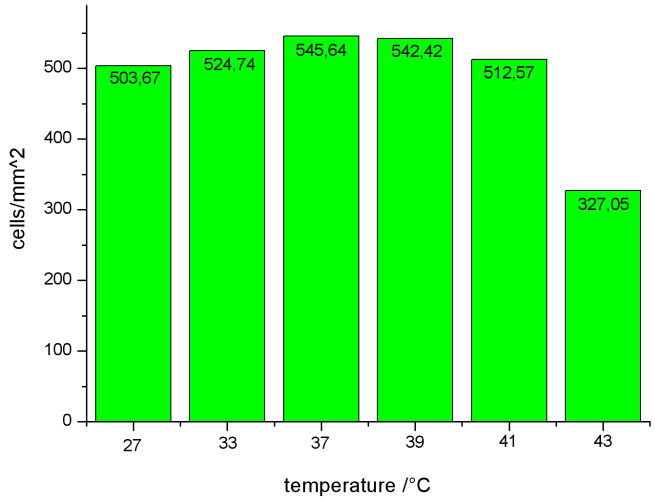

Figure 4.16: Initial adhesion of SAOS-2 cells on medical titanium with different temperatures during the incubation time $t_{\mathrm{inc}} = 60\,\mathrm{min}$. Deviations from body temperature (37°C) cause highly asymmetric results as can be seen comparing a lowering of 10°C with a rise of 6°C. In total, 1.2k $\frac{\mathrm{cells}}{\mathrm{mm}^2}$ were suspended in the medium.

deadhesion stays very low under conditions of decreased ambient temperature where again, deadhesion largely increases already with small temperature rises (cf. Fig. 4.17).

One might demand microscopic explanations for these macroscopic observations in particular as they are highly asymmetric with respect to deviations of the common ambient temperature T_{amb} of cells. One could argue that the two dominating systems in these cases are the cell membrane itself as well as proteins on or reaching through the surface of the cell. For proteins, one would expect a small stiffening resp. as small softening effect for small deviations ΔT from the ambient temperature T_{amb} as $\Delta T << T_{\mathrm{amb}}$ following equation 3.16 of the entropic spring model:

$$k(T_{\mathrm{amb}} \pm \Delta T) = \frac{3k_{\mathrm{B}}(T_{\mathrm{amb}} \pm \Delta T)}{Nb^2} \approx k(T_{\mathrm{amb}}) \tag{4.5}$$

This relation of course only holds within the regime of no denaturation of proteins taking place. The given situation nevertheless is on the edge of this regime which is the reason why protein denaturation might be a reason for the strong effect observed with slightly higher temperatures. The second system that needs to be regarded are the membranes which in contrast will exhibit a softening for lower ambient temperatures (!) whereas will become stiffer for higher temperatures. This is due to the fact that in living organisms, the cell membrane composition is adjusted in a way, so that the membrane is slightly above its phase transition temperature. Therefore, lower temperatures drive the system into its transition regime which is connected with very soft mechanical behaviour

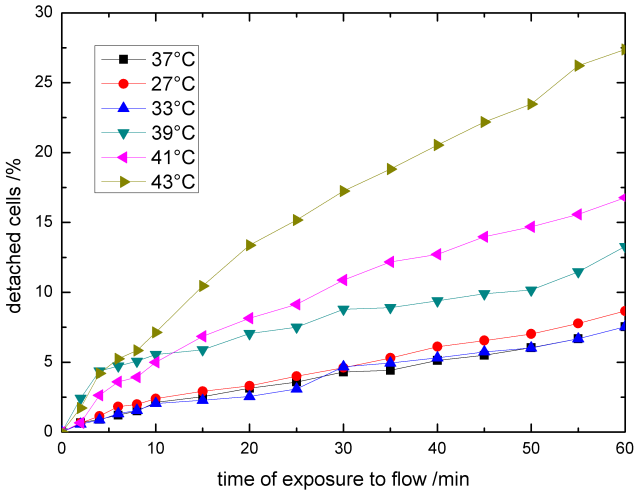

Figure 4.17: Cell detachment with respect to different temperatures over time. Even high deviations of temperatures below body temperature (37°C) do not effect deadhesion significantly whereas already a rise of 2°C results in a doubling of cell detachment.

(cf. Nuschele (2010)). The fact of these two counteracting effects of the (only supposed) two dominating subsystems for cell adhesion raises the question for the need of a theory and approach to describe the whole, integrated system as such.

4.1.2.5 Dependence of cell adhesion on antibiotics

Post-surgical inflammation is a major problem in implant medicine. To deal with this problem, some manufacturers offer implants equipped either with antibiotic-coated surfaces or reservoirs that release antibiotics over time. A typically applied substance for this purpose is Gentamicin, an aminoglycoside antibiotic (Hendriks et al. (2004)). In both cases, either if the surface is coated or it diffuses out of a reservoir, it might affect the process of cell adhesion as it occurs with locally high concentration at the position where cells and the surfaces interact. Therefore, its effect on cell adhesion was assessed. Gentamicin (10 mg/ml) was purchased from "Biochrom AG" and concentrations of 50 $\frac{\mu g}{ml}$ resp. 100 $\frac{\mu g}{ml}$ in the cell culture medium were implemented. The presence of Gentamicin caused a moderate decrease of initial adhesion of 4 % resp. 11.5 % compared to initial adhesion on titanium without presence of Gentamicin (cf. Fig. 4.18).

Deadhesion in the presence of Gentamicin showed a close to twice as high deadhesion rate compared to cells in untreated medium. The two tested concentrations of Gentamicin compared to each other exhibited no significant difference in the deadhesion rate (cf. Fig. 4.19).

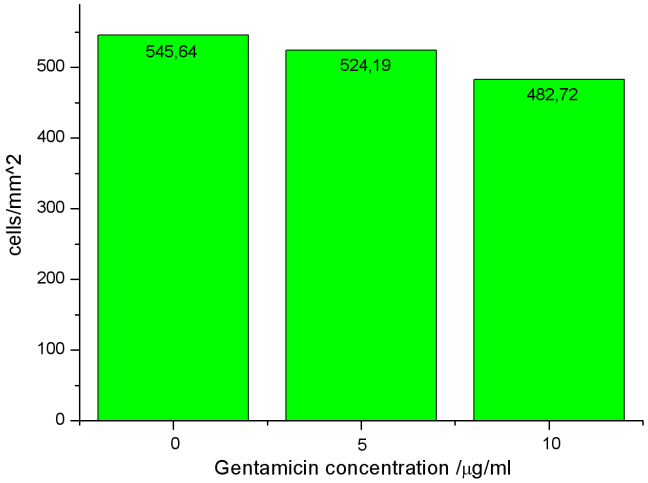

Figure 4.18: Initial adhesion of SAOS-2 cells on medical titanium with respect to the concentration of Gentamicin with an incubation time of $t_{\mathrm{inc}} = 60\,\mathrm{min}$.

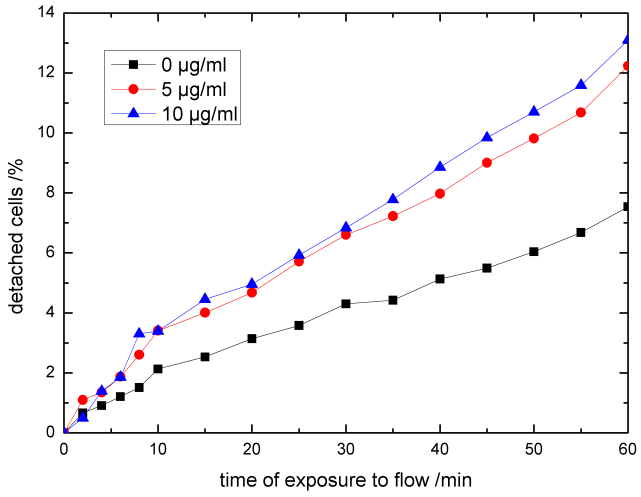

Figure 4.19: Cell detachment with different concentrations of Gentamicin over time.

4.1.2.6 Dependence of cell adhesion on the presence of nano particles

During recent years, the industrial usage of nano particles underwent a tremendous increase which led also to an increase of scientific attention. Titanium dioxide (TiO_2) e.g. is used as an UV-filter in sunscreen and silicon dioxide (SiO_2) is introduced e.g. in cosmetics and food. As these applications are connected with (potential) uptake and accumulation in living beings, attention on the relation between nano particles and health issues is growing (cf. e.g. Boisselier and Astruc (2009), Casals et al. (2012), Lu et al. (2013) and Strobl et al. (2014)). The present study therefore contributes to the question, whether the presence of nano particles might affect also cell adhesion processes. TiO_2 particles under the label "Eusolex T-Eco" were purchased from "Merck KGaA, Germany". These particles are also used in commercially available sunscreen and exhibit a needle-shaped geometry with a length of $\approx 80 - 120\,\text{nm}$ (cf. Fig. 4.20, left). The SiO_2 were synthesized at Experimental Physics I, Augsburg Uni-

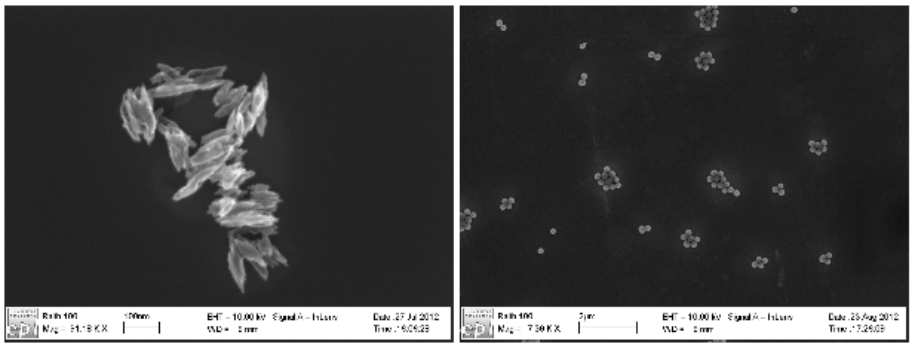

Figure 4.20: eBeam images of the TiO_2 (left image, needle-shaped, $\approx 80 - 120\,\text{nm}$ length) and SiO_2 (right image, spherical, $\approx 220\,\text{nm}$ diameter) nano particles used in the present cell adhesion study.

versity by Dr. Rudolf Herrmann and possess a spherical shape with a diameter of $\approx 220\,\text{nm}$ (cf. Fig. 4.20, right). For the analysis of the adhesion process, 10 μl of each nanoparticle suspension ($c(TiO_2) = 16.7\,\frac{\text{mg}}{\text{ml}}$, $c(SiO_2) = 22.9\,\frac{\text{mg}}{\text{ml}}$) were added to the cell suspension before the incubation time of 60 minutes. Figure 4.21 shows the effects of the presence of these nano particles on the initial cell adhesion. The effect of this rather high concentration is not prominent. In the solution with SiO_2, the initial adhesion is reduced by $\approx 5\,\%$, the solution with TiO_2 exhibits a decrease of $\approx 10\,\%$. Possible reasons for this decrease might be due to affection of intracellular processes by nano particles that penetrated the membrane, by nano particles covering the surface of the cell (altering the adhesion properties of the membrane as well as influencing the properties of adhesion molecules) and particles covering the surface of the implant leaving less residual area for cells to adhere. As the TiO_2 particles show a strong tendendy of agglomeration, their liquid-borne lifetime should be reduced in comparison to the SiO_2 particles which would result in a higher implant sample surface coverage and therefore would support the theory of steric hindrance of cell adhesion by the presence of nano particles on a surface. In terms of deadhesion, the presence of nano particles showes nearly no effect with around a half resp. one

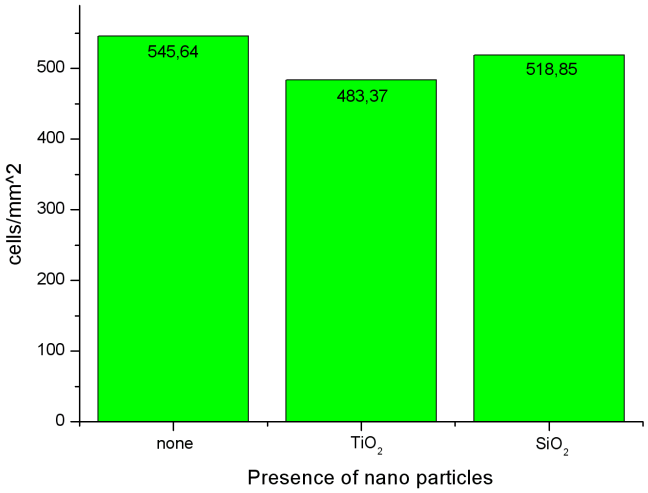

Figure 4.21: Initial adhesion of SAOS-2 cells on medical titanium in presence of nano particles after $t_{\mathrm{inc}} = 60\,\mathrm{min}$.

percentage point in the case of TiO_2 resp. SiO_2 (cf. Fig. 4.22). Therefore, the presence of nano particles seems to be of inferior importance for cell adhesion processes.

4.1.2.7 Cell adhesion on Ag-doped DLC surfaces

The main requirements for the development of DANI included the ability to be capable of measuring any arbitrary implant material. Therefore, also materials beyond medical titanium were examined in this study. The diamond-like-carbon (DLC) surfaces doped with silver (cf. part 4.1.1.3) revealed the initial adhesion properties depicted in Fig. 4.23 under the usual conditions with $t_{\mathrm{inc}} = 60\,\mathrm{min}$. First of all, it is interesting to see that the initial adhesion in comparison to medical titanium is significantly reduced. Under equal conditions, less than 50 % adhere on the DLC surfaces despite their well-documented proper biocompatibility (cf. Thorwarth et al. (2007)). Within the DLC samples, the silver-doped samples showed an increased adhesion affinity with increased silver content for "weak" dopings ranging from "DLC PVP" to "Ag:PVP 1:10" (cf. part 4.1.1.3). Nonetheless, for "Ag:PVP 1:2", no adhesion at all could be observed (not depicted in Fig. 4.23). Such a behaviour with a maximum affinity within a series indicates two counteracting effects. In this case, a reasonable interpretation of the data is connected with electrostatics and toxicity of silver. For low dopings, the net positive charge of the Ag^+-ions in the DLC matrix exerts an attractive force on the cells as cell membranes possess a net negative charge which leads to increased initial adhesion. With increased doping, the toxic effect of silver becomes more prominent and impedes adhesion resp. kills the cells. This hypothesis is fortified by the dynamic cell adhesion measurements (cf. Fig. 4.24). One can clearly see the highest deadhesion rate occurs for "Ag:PVP 1:10" which

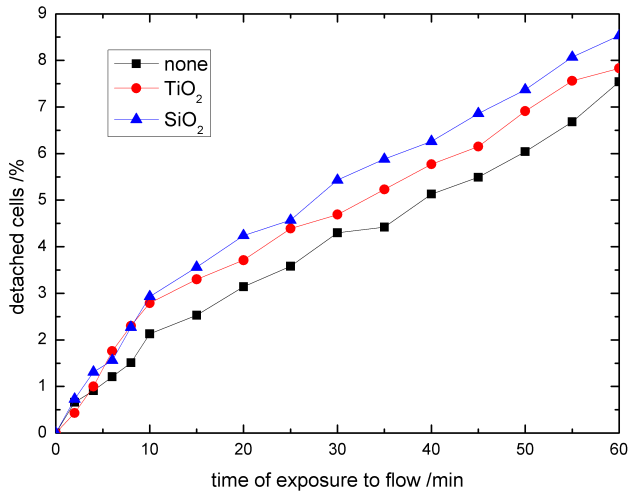

Figure 4.22: Cell detachment in environments of different nano-particle types over time.

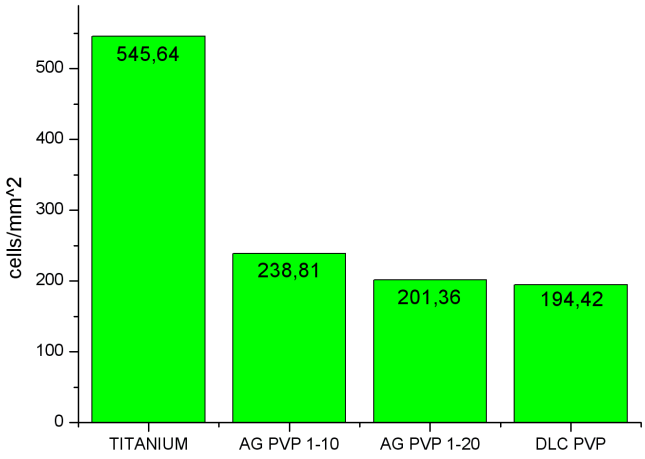

Figure 4.23: Initial adhesion of SAOS-2 cells on different substrates with an incubation time of $t_{\mathrm{inc}} = 60\,\mathrm{min}$.

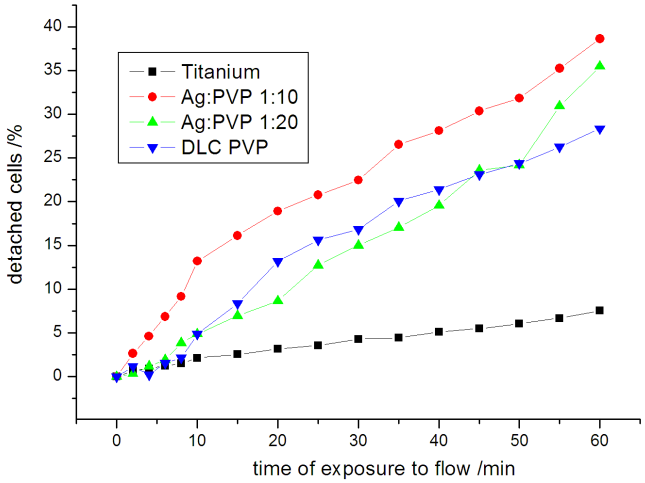

Figure 4.24: Detached cells on different substrates over time.

also had the highest initial adhesion. With lower resp. no Ag-doping, the deadhesion rate decreases. Therefore, within the DLC surface samples, *a higher initial adhesion* is connected with *a higher deadhesion rate* which is in contrast to the findings with medical titanium surfaces in part 4.1.2.2. This again is an indication for a harming effect of the silver-doping. Not only the fact, that high initial adhesion goes together with higher deadhesion, but also the fact that deadhesion is lower for the first 40 minutes at the "Ag:PVP 1:20" sample in comparison to "DLC PVP", but from 50 minutes on, deadhesion at "Ag:PVP 1:20" rapidly increases. This can be interpreted as a retarded effect of the silver as the concentration here is much lower compared with the other Ag-doped samples.

4.1.2.8 Cell adhesion measurements with different IDTs

The measurements presented so far were all performed with the standard set of IDTs (SIDT) presented in section 4.1.1.2. To prove the versatility of the presented technological solution for cell adhesion measurements, several different shaped IDTs were integrated into the DANI system and experiments were performed. The invented IDTs and the properties resulting for cell adhesion measurements are shown in the following paragraphs. The changes of the design of the IDTs aimed in two directions, either to create higher shear rates or broader spectra which of course also can be achieved together.

The double IDT - DIDT

The most obvious approach to increase the intensity of the flow and to focus it better is to double the present structure of the standard ITD and position its copy in a certain distance, so that the jets generated by the IDTs converge at the top of the chamber, where the implant sample with the adhered cells

is placed. Figure 4.25 shows a schematic drawing of the DIDT structure. A

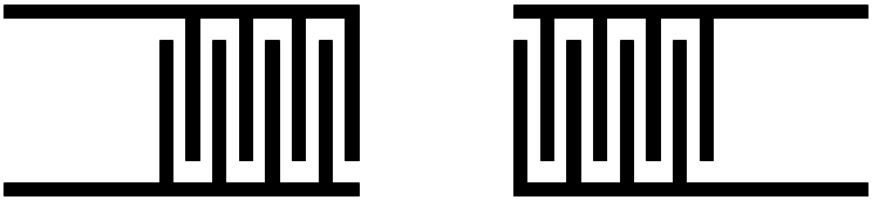

Figure 4.25: Schematic drawing of the double IDT (DIDT) structure.

clear drawback of this solution is that in this particular geometry, the intended constraint of the jets converging at the sample leads to a short distance between the two IDTs of 1.1 mm so that the view field is largely affected (cf. Fig. 4.26). Nonetheless, the intended goal of reaching higher maximum shear rates $\dot{\gamma}_{\max}$

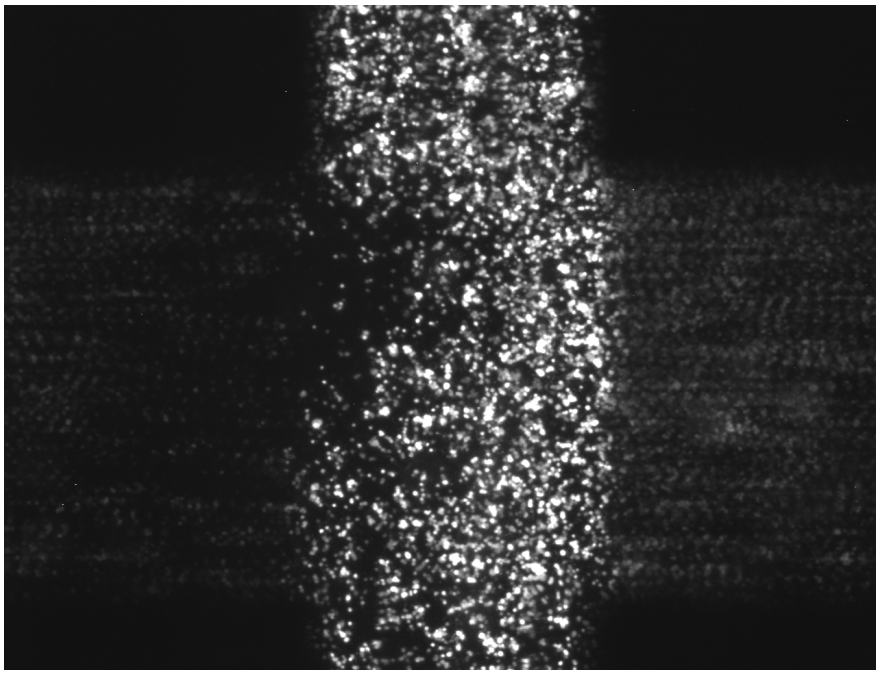

Figure 4.26: Exemplary image from a measurement performed with a DIDT structure. Despite higher shear rates that can be achieved, a largely reduced field of view is a clear drawback of the DIDT structure.

could be achieved with $\dot{\gamma}_{\max}(\text{DIDT}) = 74.2\,\text{s}^{-1}$(cf. Fig. 4.27) in contrast to $\dot{\gamma}_{\max}(\text{SIDT}) = 31.9\,\text{s}^{-1}$ with the SIDT (cf. section 4.1.1.6).

The tapered IDT - TIDT

Another, more sophisticated way to design IDT structures and therefore to alter the flow profile is the technique of so-called tapered IDTs (cf. Fig. 4.28). By changing the distance $\frac{p}{2}$ between the conducting metal stripes along their longitudinal axis, the resonance frequency f_{res} changes following $f_{\text{res}} = \frac{v_{\text{SAW}}}{p}$

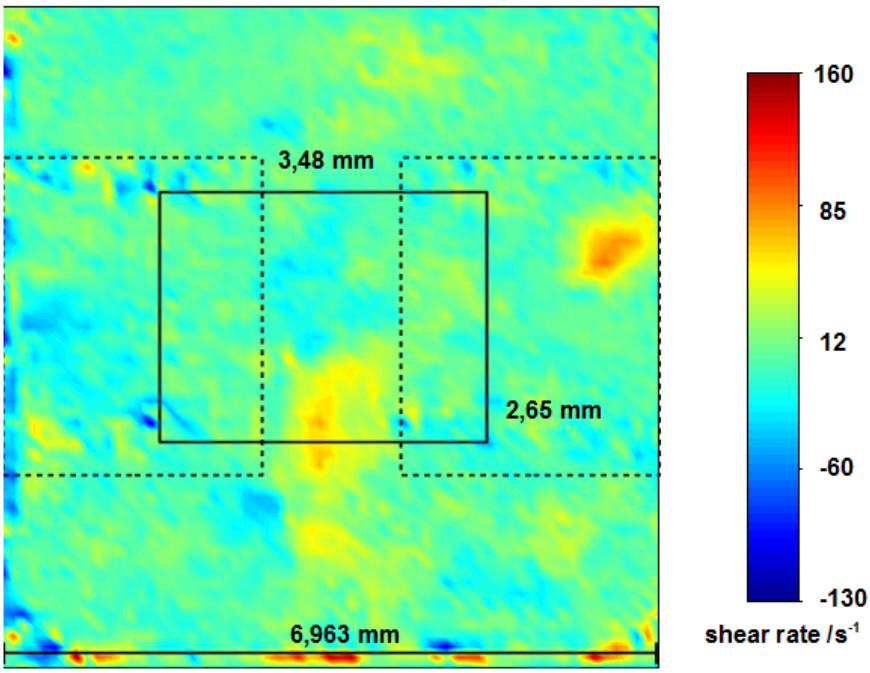

Figure 4.27: Shear rate distribution of the DIDT obtained from the velocity gradients $\dot{\gamma} = \frac{\mathrm{d}v}{\mathrm{d}z}$ in 3 plaines in 0 - 108 μm distance from the sample.

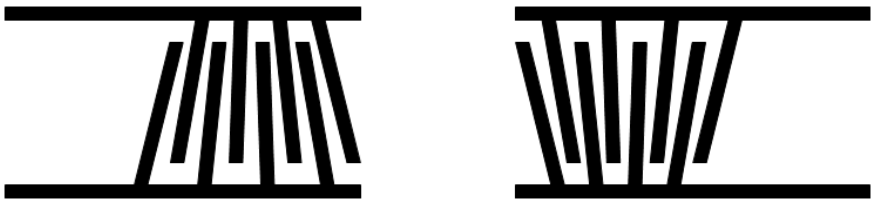

Figure 4.28: Schematic drawing of the tapered IDT (TIDT) structure.

(Eq. 4.1). Therefore, a whole spectrum of resonance frequencies $f_{\mathrm{res,high}}$ to $f_{\mathrm{res,low}}$ is capable of inducing SAWs, and even more interesting for this particular application, the point of excitation along the electrode changes with the frequency. This splendidly offers possibilities to manipulate the flow patterns within the chamber. To overcome the problem of the reduced field of view (cf. Fig. 4.26) discussed in the context of the DIDTs, the tapered IDT structures where placed further apart of each other (3 mm from front edge to front edge). The geometry of the IDTs was chosen in a way, that frequencies from 151 to 166 MHz could be used for excitation. Despite this variety of possible excitations and flow patterns, the maximum shear rates close to the sample keep in the same range as with the SIDT with $\dot{\gamma}_{\max}(\mathrm{TIDT}-166) = 24.4\,\mathrm{s}^{-1}$, $\dot{\gamma}_{\max}(\mathrm{TIDT}-151) = 36.6\,\mathrm{s}^{-1}$ and $\dot{\gamma}_{\max}(\mathrm{TIDT}-158.5) = 25.5\,\mathrm{s}^{-1}$.

The focused IDT - FIDT

Another approach for increasing the maximum shear rate was realized by a curved IDT design (cf. Fig. 4.29). Despite an anticipated worse power transduction characteristics, the governing idea for this approach was a more focused flow pattern in the chamber.

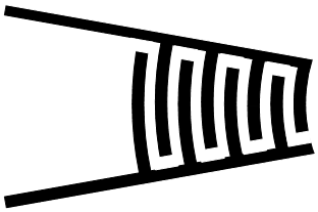

Figure 4.29: Schematic drawing of the focused IDT (FIDT) structure.

Although the power transduction revealed to be much worse compared to the other IDTs (cf. table 4.2) with less than 50 % power incoupling, the maximum shear rate that could be reached was the highest of the designed IDTs with $\dot{\gamma}_{\max}(\mathrm{FIDT}) = 104.1\,\mathrm{s}^{-1}$. Further on, the pattern of cell deadhesion followed in a very comprehensible way the shear rate profile of the FIDT with its radial shape (cf. Fig. 4.31).

Summarizing, the experiments with the different IDTs revealed a very interesting point. The reachable maximum shear rate $\dot{\gamma}_{\max}$ depends to the largest extent on the *geometry* of the IDTs and therefore also on the geometric structure of the flow but not on the *power* introduced to the system. All experiments were operated with an input power of 27 dBm, nonetheless, the power transduction properties of the IDTs exhibit remarkable differences, in particular the FIDT (cf. Tab. 4.2). The power uptake of the fluid is assumed to be the complete power that is not reflected as ohmic losses should be of minor magnitude. With reflections of all IDTs ≤ -15 dB except the FIDT, the incoupled power is therefore > 96 % which equates to ≈ 500 mW. The FIDT on the other hand only transduced 42 % of the power. Despite this poor incoupling behaviour, the FIDT reached by far the highest shear rates with $\dot{\gamma}_{\max}(\mathrm{FIDT}) = 104.1\,\mathrm{s}^{-1}$ in contrast to the DIDT with $\dot{\gamma}_{\max}(\mathrm{DIDT}) = 74.2\,\mathrm{s}^{-1}$, but at the cost of a largely limited view field and the other IDTs that only reach about $30\,\mathrm{s}^{-1}$.

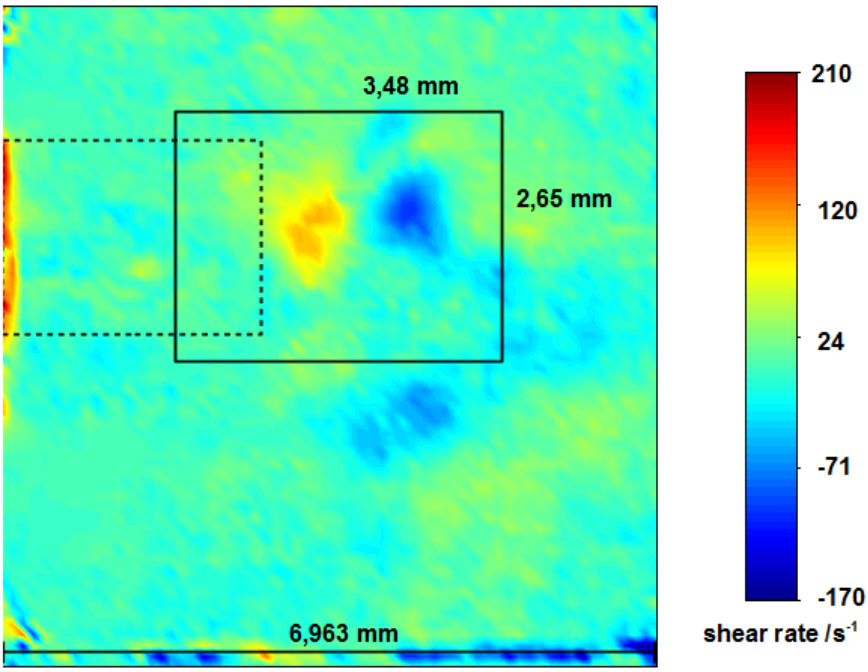

Figure 4.30: Shear rate distribution of the FIDT obtained from the velocity gradients $\dot{\gamma} = \frac{\mathrm{d}v}{\mathrm{d}z}$ in 3 plaines in 0 - 108 μm distance from the sample.

IDT	attenuation (dB)
SIDT	-17.5
DIDT	-18.5
TIDT (151 MHz)	-15
TIDT (158.5 MHz)	-15
TIDT (166 MHz)	-18
FIDT	-2.3

Table 4.2: Reflexion behaviour of the different IDTs; the attenuation compares the intensity of an input signal with its reflexion. Assuming negligible ohmic losses, the reflexion is a measure for the power that is incoupled into the microfluidic system.

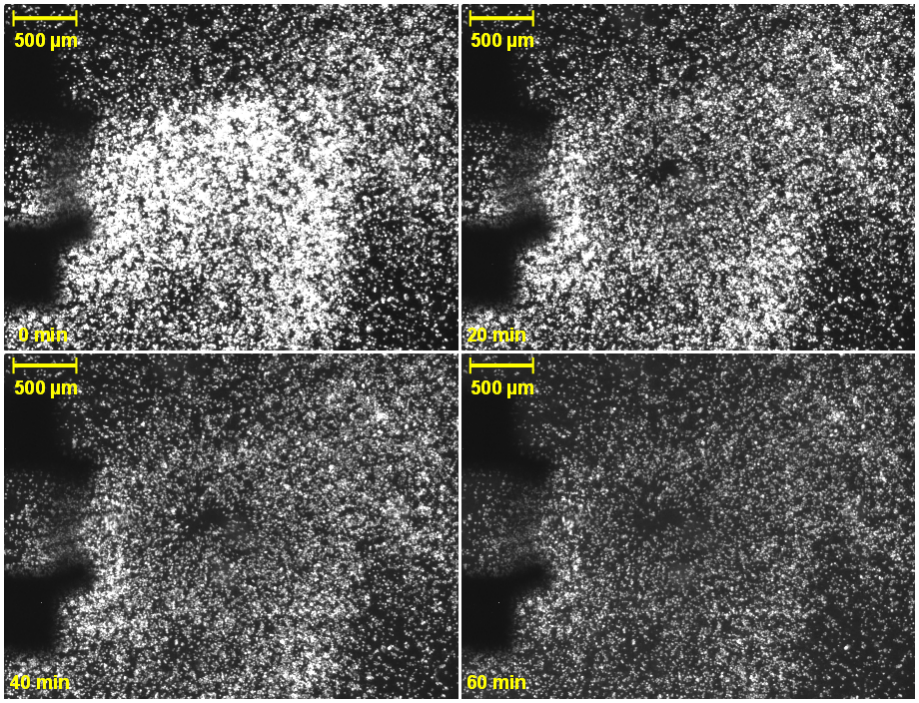

Figure 4.31: SAOS-2 cell population on medical titanium treated with the FIDT over time (upper left: initial conditions, upper right after 20 min, lower left after 40 min, lower right after 60 min); the cell deadhesion exhibits a radial pattern with the focus point of the IDTs in the middle.

4.1.2.9 Visualization of cell displacement without deadhesion

Beyond the capability of DANI to quantify cell deadhesion, it also allows to visualize and study cell displacement on the sample-surface which seems to be connected with a semi-bound state of the cell and occurs as a kind of rolling on the surface (cf. Fig. 4.32, cell displacement made visible via Colocalization analysis tool of the NIH software ImageJ, cf. section 4.1.1.5). Questions about cell dislocation were not in the focus of the present work and therefore not subject to systematical studies. Nevertheless this feature holds great potential for cell adhesion studies e.g. in contexts like adaptation of the cells to flow profiles or surface interaction studies with (biological) coatings.

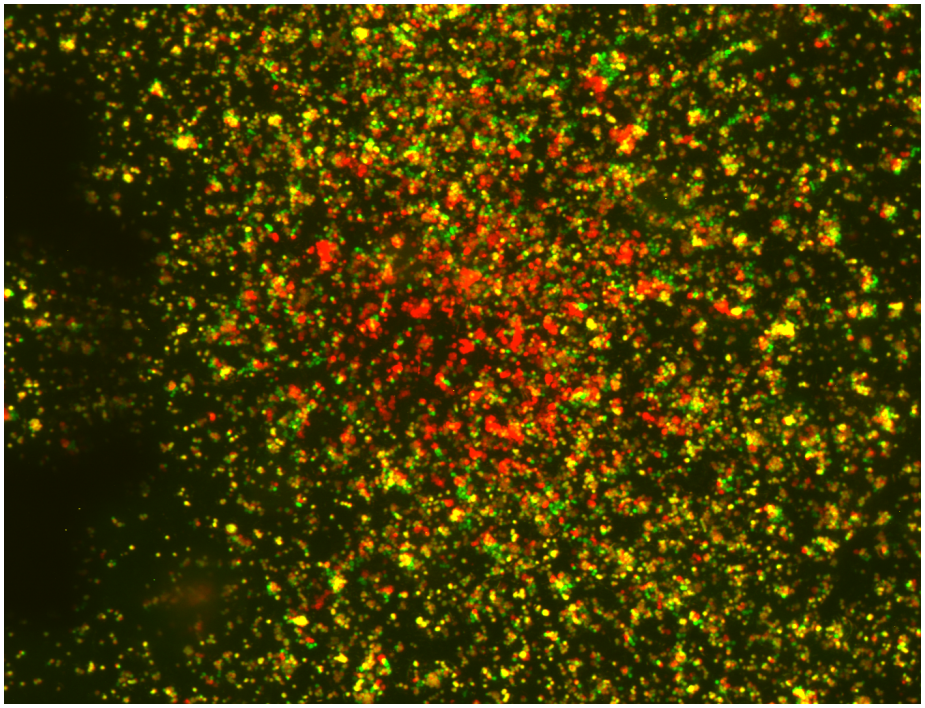

Figure 4.32: Visualization of cell displacement using DANI. By image post-processing with ImageJ (provided by the NIH) spots can be highlighted where no change took place between two image frames, therefore, the cells stayed at their position (yellow), as well as spots where cells where in the first frame but not in the second (red) and reversely (green).

4.2 Entropic fluctuations of von Willebrand factor

4.2.1 The physiological role of von Willebrand factor

The von Willebrand factor (vWF) is a blood-borne glycoprotein that is essestially involved in hemostatis. It was initially predicted by the Finnish hematologist Erik Adolf von Willebrand in 1926 (originally published in Finnish, available as English translation in Willebrand (1999)). Von Willebrand discovered an inherited hemophilic disease among residents of the Åland Islands in the Gulf of Bothnia. In the subsequent decades the disease was identified to originate from the lack of a "blood plasma factor" like it is called in the medical jargon (Sadler (1991)). In recent years, it also became evident, that vWF plays an important role in the process of metastasis of tumor cells (cf. e.g. Terraube et al. (2006)). Besides its medical importance, vWF is in particular interesting to physicists as this large molecule is capable to serve as a nanomechanical sensor. It senses shear stress and undergoes a reversible conformational transition at a critical shear rate $\dot{\gamma}_{\mathrm{crit}}$ (cf. Schneider et al. (2007) and Fig. 4.33). vWF exhibts hier-

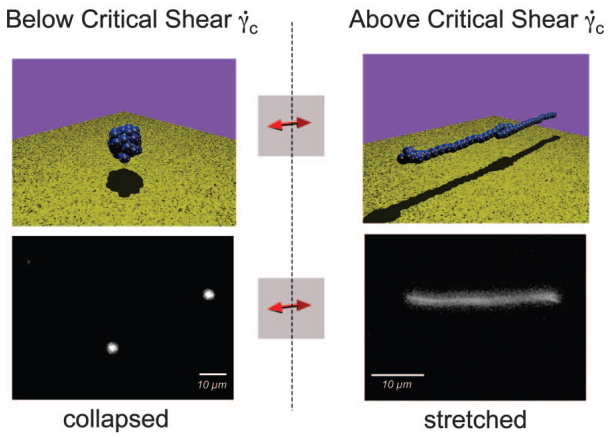

Figure 4.33: Cartoon and fluorescent microscopy image of the conformational change von Willebrand factor undergoes depending on the surrounding shear rate regime. Image taken from Schneider et al. (2007).

archical structure properties. It consists of monomeric units of 60 nm length. However, the smallest units found in the body (except in the endoplasmic reticulum, where the monomers are merged) are dimeric units (protomers) of 120 nm length and about 250 kDa. These dimers polymerize to multimers of more than 2000 kDa and therefore, vWF reaches lengths in the μm-range (cf. Fowler et al. (1985), Sadler (1998)). This makes it one of the largest polymers found in the human body. To gain closer insight into the magnitude of relevant forces for vWF and its response to those external forces, several force spectroscopy experiments on vWF were performed so far (e.g. atomic force microscopy: Westerhausen (2012); optical trap: Ying et al. (2010), Springer (2011)). More details on single molecule force spectroscopy will be presented in part 4.2.2.1. Despite the numerous vWF experiments available so far, to the author's knowledge, all

these measurements were performed in a "dynamic force spectroscopy"-setting. That means, that a certain load, e.g. from 10 to 100 $\frac{\mathrm{pN}}{\mathrm{s}}$, is applied to a relaxed vWF molecule and the force-distance progression during the stretching of the molecule is observed. Dips in these progressions are interpreted as the unfolding of a domain within the molecule (cf. Fig. 4.34). The unfolding of a domain

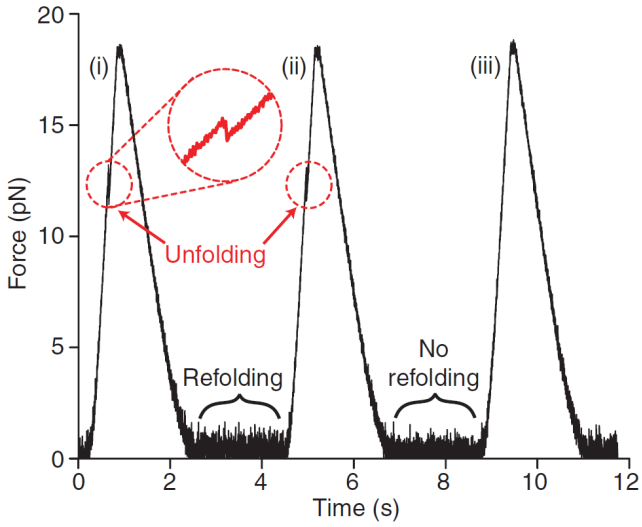

Figure 4.34: The graph shows the force over time of von Willebrand factor stretched with an optical trap with constand load. The red circles mark sudden reductions in force which are interpreted as so-called domain unfolding events; graph taken from Springer (2011).

here means the following. As seen in section 3.3, polymers can be described as entities made up of subunits that are arranged following a random walk. This consideration led to equation 3.15 which reveals the entropic character of the extension of a polymer. In particular, this means that parts of a large polymer are coiled up. By chance, some of these agglomerations (called domains) are thermodynamically pretty stable and unwind only under high threshold forces. After exceeding this threshold by external means, a domain unfolds which spontaneously releases "additional" contour length which leads to a force reduction at the force sensor (here, the optical trap). In this manner, people measure domain unfolding characteristics (of vWF and in general of arbitrary molecules) and try to learn from these extreme non-equilibrium, highly perturbated systems about the equilibrium properties of a system following ideas like presented in Jarzynski (1997). The present work, in contrast, treads a different path as it presents data gained from experiments that minimize external perturbations. A passive way of investigating vWF was implemented by straining it between two points and observing its (thermal) fluctuations. The intention of the experiments performed is in particular to gain insight into vWF equilibrium properties as well as in general to gain insight into the behaviour of polymers in thermal equilibrium.

4.2.2 Materials and Methods for passive fluctuation probing

4.2.2.1 BioForceProbe technique

The BioForceProbe (BFP) technique was developed by Evan Evans and first described in Evans et al. (1995). It serves for single molecule force spectroscopy, like e.g. also Atomic Force Microscopy (AFM) and Optical Traps (OT) do. BFP is very useful in particular to address questions in biological environments. It uses glass pipettes to fasten the relevant objects in the measuring chamber. Those are either glass beads coated with the molecule to investigate and specific antibodies or even real cells. Further on, an erythrocyte (red blood cell, RBC) aspirated with a pipette is used as a soft force sensor with an equivalent spring constant adjustable from $\sim 0.1 - 1\ \frac{\mathrm{pN}}{\mathrm{nm}}$ (cf. Fig. 4.35).

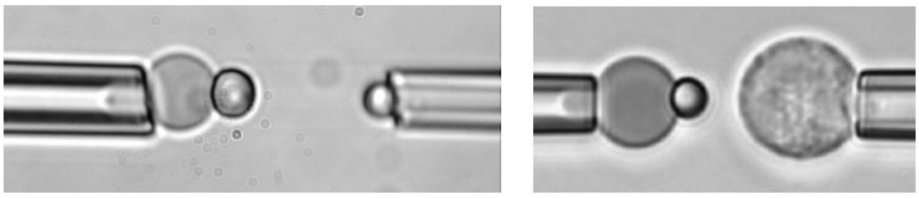

Figure 4.35: Images of initial BFP setups; in both cases, on the left pipettes an erythrocyte is aspired where a glass bead is glued on using a biotin-streptavidin binding; in the left case, the right pipette holds another glass bead, in the right case, the surface of a real cell, here a leucocyte, is probed; right image taken from Evans et al. (2005).

On the erythrocyte, another glass bead with an antibody to the molecule of interest is glued via a streptavidin-biotin bonding. The spring constant k_{RBC} of the RBC basically depends on geometrical constraints and the suction pressure:

$$k_{\mathrm{RBC}} \approx \frac{\pi R_{\mathrm{P}} \Delta p}{(1 - \frac{R_{\mathrm{P}}}{R_0}) \ln(\frac{4R_0^2}{R_{\mathrm{P}} R_{\mathrm{C}}})}$$

with the pipette radius R_{P}, the RBC radius (outer part) R_0, the radius of the adhesive contact between RBC and glass bead R_{C} and the aspiration pressure Δp which is controlled via hydrostatically connected water tanks (cf. Evans et al. (2005)).

The "spring constant" here has the meaning of a necessary force per distance for deforming the RBC along the longitudinal axis running through the pipette and the RBC. The actual detection of the force is in fact the optical measurement of the deformation of the RBC. This is carried out by focussing the camera on the dark separator which occurs at the position, where the glass bead is glued onto the RBC (cf. Fig. 4.35). The position of this separator is measured by following the moving brightness minimum (cf. Fig. 4.36). The minimum is fitted by a second-order polynom whereat the vertex position changes get translated into the force signal.

BFP allows loading rates in the broad range from $10 - 10^4\ \frac{\mathrm{pN}}{\mathrm{s}}$. Further on, it can be operated with a noise level close to the thermal noise limit. For a RBC

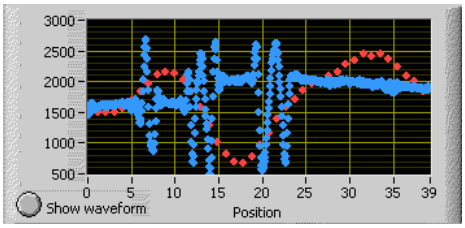

Figure 4.36: Image section of the graphical interface of the LabView control software. The blue line shows the brightness distribution (in a.u.) along the whole camera view area, the red dots are a zoom onto the separator between the erythrocyte membrane and the glass bead. The fitted minimum position and its movement gives information about the membrane deformation and therefore about the acting forces.

adjusted to 0.5 $\frac{\mathrm{pN}}{\mathrm{nm}}$, using the equipartition theorem

$$\frac{1}{2}k_{\mathrm{P}}\mathrm{var}X = \frac{1}{2}k_{\mathrm{B}}T$$

one would expect a mean thermal displacement $\Delta X_{th} = 2.85\,\mathrm{nm}$.

The total noise ΔX_{tot} on the particular BFP system used for the subsequently shown experiments could be reduced down to $\Delta X_{tot} \sim 4.4\,\mathrm{nm}$ which corresponds to 2.2 pN with the given spring constant. Compared to AFM where noise levels are usually one order of magnitude higher, this allows investigation also of very little conformational changes of single molecules that are related to force changes on the probe. Optical traps on the other hand allow much more sensitive measurements than AFM and also BFP, but suffer of the problem, that the spring constant is defined by a laser-induced electro-magnetic potential. This leads to local heating and thermal gradients and therefore might alter a molecules behaviour. For that reason, the BFP technique ideally bridges the gap between sensitivity requirements and force requirements that both are necessary in particularly for the passive fluctuation probing of a very large molecule like vWF while ensuring stable and representative thermal conditions. For further information about AFM, OT and BFP and their use in biophysics see also Sackmann and Merkel (2010).

The setup used for the measurements consists of an inverted microscope (Zeiss Axiovert 100) which is adapted for the BFP-specific requirements. It is equipped with a 40X/0.75 objective and two cameras, a high-speed camera ($\sim$ 1500 fps, SensiCam) and a regular speed camera ($\sim$ 30 fps, Dage MTI). The high-speed camera serves for high spatiotemporal resolution detection of the RBC movement, in particular, it is focused on the edge between RBC and the glass bead, that is glued on the RBC (cf. Figs. 4.35 and 4.36). A mercury lamp together with a green band pass filter served as light source. The fine mechanical positioning of the pipettes is carried out via micrometer screws, where they are attached on, and a piezo-controller (PI), that is connected to a computer with a software system (LabView) that integrates both, optical detection as well as mechanical control.

The glass beads and RBCs were functionalized via NHS (N-Hydroxy-succinimid)- and maleimide-coupling-chemistry which are biochemistry stan-

dard. Further on, biotin and streptavidin are used to enable the positioning of a glass bead on a RBC and finally, vWF and vWF-antibodys are coupled to the beads. The procedures and protocolls can be found in detail in the Appendix 6.2. Nota bene, there was performed an interesting study on reversible aggregates of vWF and glass beads which were functionalized with vWF-antibody (cf. Chen et al. (2013)). These functionalized beads were the very same ones as used for vWF interaction presented in this study. The preparation of an experiment works as described in the following. First, two narrow (~ 3 mm) glass slides are cut off a coverslip. These are glued with vacuum grease on top and bottom of a metal holder (height ~ 1.5 mm). This forms a measuring chamber which is open on two sides and allows the insertion of the pipettes. Water resp. buffers rest in the chamber only due to surface tension (cf. Fig. 4.37). After the chamber preparation $\sim 115\,\mu$l of HEPES buffer (cf. Appendix 6.2.2) are filled into the chamber filling it up $\sim 85\,\%$. Further on, three pipettes get filled with HEPES buffer and are positioned within the chamber. On the left-hand side pipette, the so-called probe pipette, the RBC will be aspired later on. The so-called target pipette is positioned in opposition to it. A third pipette, the helping pipette, is positioned in an angle of $\sim 150^\circ$ to the probe pipette. It does not take part in the actual experiment, but is required in order to glue the probe bead with the specific antibodies of the molecule to investigate onto the RBC. A droplet of the two kinds of beads and the RBCs are injected into the chamber at different spots. Step by step, the "target bead" and the RBC gets fixed at the pipette tips via suction. The probe bead first is fixed at the helping pipette via suction, is transferred to the RBC and then "glued" at coaxial position onto the RBC. This delicate preparation procedure is supported by usage of micromanipulators and leads to an initial state of the experiment shown on the left in Fig. 4.35. Figure 4.37 shows the BFP setup with the microscope, the three pipettes and the measuring chamber which holds the liquid only due to surface tension.

From this starting configuration on, no further manual intervention takes place anymore. The position of the target pipette is controlled via the piezo-controller, everything else stays fixed.

4.2.2.2 Experimental procedure

The experiments are performed following a protocol defined by four phases that are carried out by the piezo-controller via software control. First, the probe- and target-bead are brought together and with a certain probability, a vWF-antibody-binding develops. The surface density of vWF and its antibody are adapted in the bead preparation procedure in such a way, that only in around $10\,\%$ of all impingement cases, a binding develops. This adjustment is done in order to have a high probability of only having *one single* binding in case of a successful binding following a Poisson-statistics consideration. In case of such a binding, the measurements result in a plot like e.g. depicted in Fig. 4.38, which is also used for further explanation of the different experimental phases.

The four phases depicted in Fig. 4.38 specifically are:

- impingement (I): the target bead is driven towards the RBC until a force of $-20\,$pN is detected. It is held there for 0.2 seconds.
- stretching (II): the pipette is retracted 240 nm resp. 200 nm from the

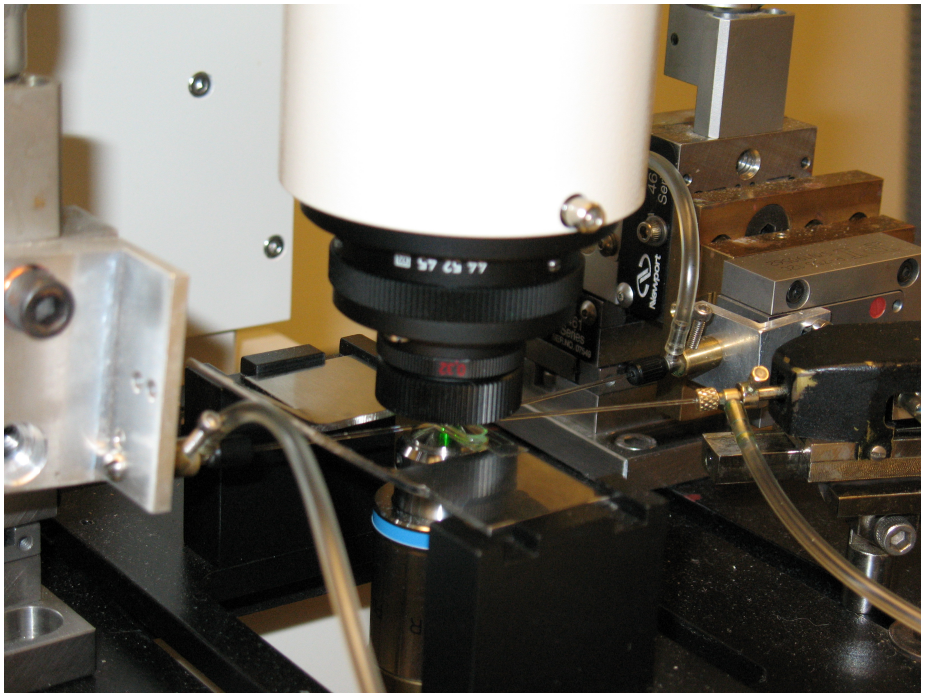

Figure 4.37: The BioForceProbe in its initial state for experiments. In the middle, above the objective, a measuring chamber which consists of two narrow glass slides separated by a metal holder is situated. It is filled with a hypotonic buffer that is kept in the chamber only due to surface tension. From the sides, three hydrostatically coupled glass pipettes reach into the chamber.

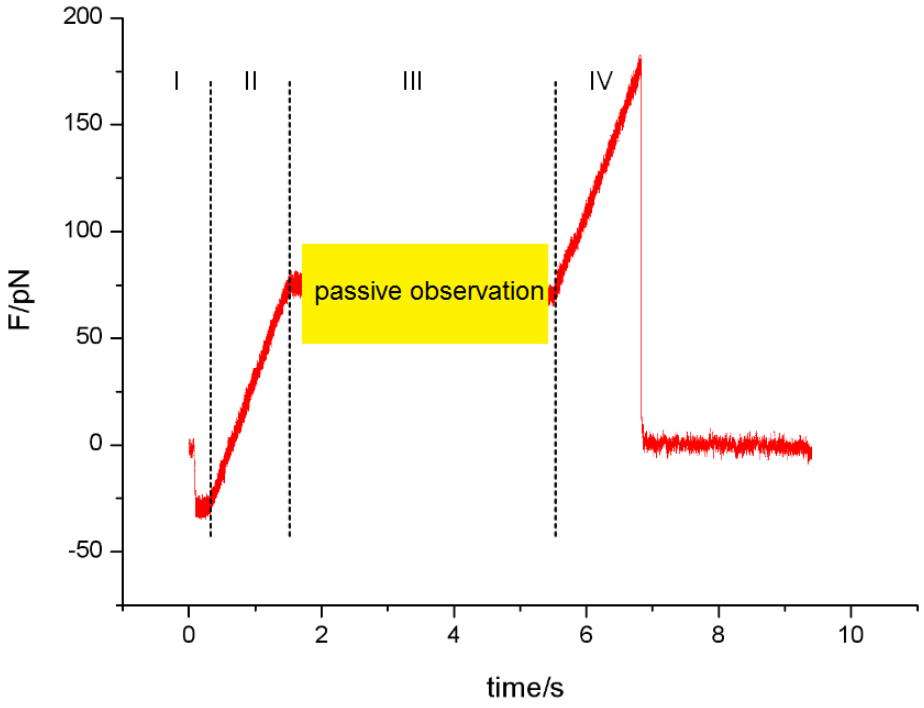

Figure 4.38: The four phases in a passive vWF fluctuation experiment - I: impingement, II: stretching, III: passive observation, IV: retracting phase.

zero force position with a loading rate of 100 $\frac{\text{pN}}{\text{s}}$. In case of a successful binding, the membrane of the RBC is pulled out of its zero position which is translated into a force signal. This process is similar to the numerous "dynamic force spectroscopy" experiments performed so far on vWF and therefore reveals also cases of "domain unfolding" as a matter of course. The final force level of this phase defines the initial force for the observation of the fluctuations in the passive setting.

- passive observation (III): this is the main part of the experiment; the piezo is kept in an idle position; any deformation of the RBC therefore is due to changes in the state of the vWF molecule clamped between the two glass beads; the experiments were performed with observation times t_{obs} of 4, 5 and 10 seconds.

- retracting phase (IV): the target bead is removed 1 μm again with a loading rate of 100 $\frac{\text{pN}}{\text{s}}$ in order to ensure, that the vWF-antibody-binding is broken.

In this manner, several successful experiments where performed - successful here in a sense of having had an interaction between vWF and its antibody which lead to a displacement of the erythrocyte membrane as described above within a complete run of the four mentioned phases. The force/elongation-time curves gained this way were analyzed using an algorithm written in SciLab which is described in details in the Appendix (c.f. 6.2.4). Note, that by necessity of

the technique, the observable in these measurements is the position of the edge of the erythrocyte which causes the results to be either elongation-time curves or force-time curves as they can be converted into each other using the spring constant $k_{\mathrm{RBC}} = 0.5\frac{\mathrm{pN}}{\mathrm{nm}}$ of the erythrocyte. It has to be clarified, that with the presented experimental setup, there is no possibility for the experimenter to further influence the way, how probe and target bead hit each other. This implies that the vWF antibody and the vWF molecule will *randomly* catch up each other and form a binding - in case they do. Therefore, each successful run of an approach-stretch-rest-retract cycle in general states an independent thermodynamic situation. Therefore, over time with many runs, this setup should sample vWF in different thermodynamic phases possibly including a phase transition regime.

4.2.3 Experimental results

4.2.3.1 "Active" polymer behaviour in a passive setting

According to the established polymer theories (cf. section 3.3 and equation 3.15), at a given set of ambient conditions (T, N, b) and a fixed external loading force $\vec{f}$, polymers have a certain *specific and fixed* extension or end-to-end vector $\vec{R}$ which is therefore an exact analogon to a mechanical spring. This in particular includes the fact, that without external manipulation, the system remains unchanged. Occurring changes are explained by energy take-up from the surrounding heat bath that lead to the occupation of different states following a Boltzmann-statistics. This model which is often referred to as "entropic spring" is based on a microscopic derivation. In contrast, the thermodynamic approach presented in section 3.4 is a macroscopic theory. The most striking difference in these two approaches is the role of entropy as in the later, entropy plays an active role which leads to the prediction of "activity" in a system despite of a passive ambient setting. This "activity" is due to the fact, that a system in equilibrium will undergo by sheer necessity different states (cf. e.g. section 3.4 and Fig. 3.5).

Indeed, within several experiments including hundreds of single cycles, such an "active" behaviour of vWF could be observed manifold (c.f. Fig. 4.39 and in the Appendix 6.2.5). This in particular includes *reversible* fluctuations in length of vWF even though there is an external force which might suppress contractions of vWF as one could naively think. This being not the case is a central prediction of the theory presented in part 3.4. The occurrence of reversible fluctuations clearly could be confirmed.

In the Appendix (Section 6.2.5), further examples are shown for the sake of an impression of the broad variety of reversible fluctuations with and against the outer force of the erythrocyte. Note, that only the "passive phase III" will be depicted.

To the authors knowledge, there are already at least a few experiments out there that show similar observations, yet the authors of these studies draw (completely) different conclusions resp. work with different models. As examples, there shall be shown the fluctuation behaviour of DNA hairpins (e.g. described in Woodside et al. (2006)) and the fluctuation behaviour of the molecule calmodulin described in Stigler et al. (2011).

Figure 4.40 shows the extension fluctuations of a DNA hairpin under a given

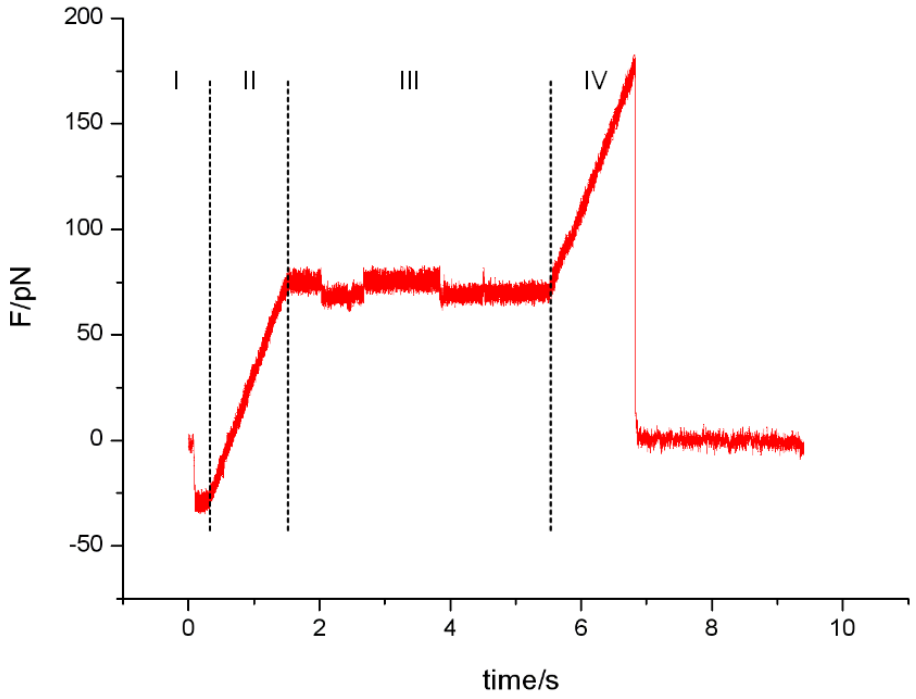

Figure 4.39: vWF undergoing *reversible* fluctuations in length against an external force during the phase of passive observation, denoted III.

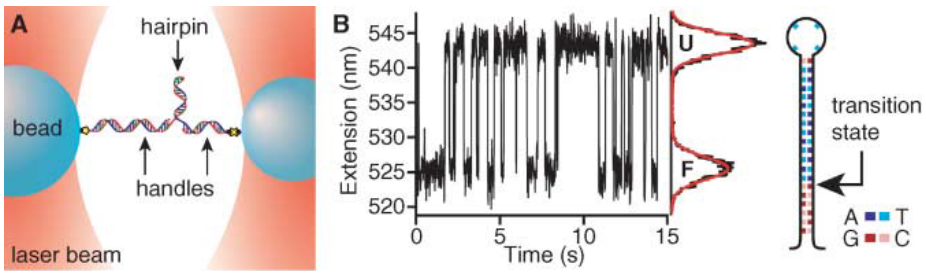

Figure 4.40: Fluctuations in length of a DNA hairpin measured with an optical trap in the work of Woodside et al. (2006).

external force, which is in principal a similar experiment as the earlier described one performed with vWF. The theoretical approach which is used to describe these results are free-energy landscapes which basically work with a mechanical spring obtaining different states following Boltzmann statistics. A further experiment with (in principal) the same observations and same theoretical framework is shown in figure 4.41.

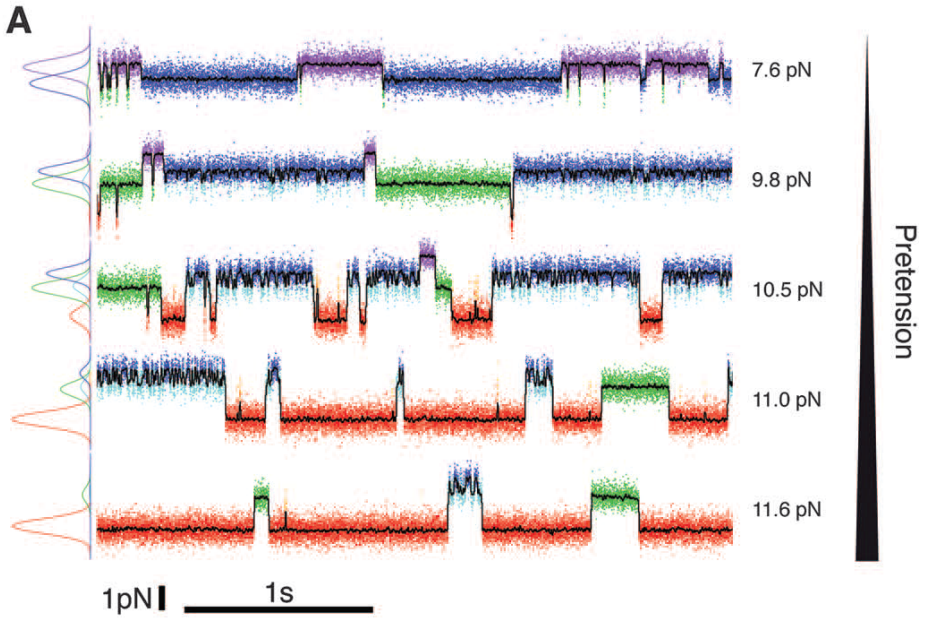

Figure 4.41: Fluctuations in length of calmodulin under different fixed external forces measured with an optical trap in the work of Stigler et al. (2011).

In this particular experiment, calmodulin is observed in a passive manner using different initial "clamp forces". This makes this experiment very interesting as well from a thermodynamic point of view as it shows a molecule under defined constraints, therefore in principle allowing to observe the molecule in different thermodynamic phase states and relate it with the occurring fluctuations (which should be maximal in the phase transition regime). Therefore, from a thermodynamic perspective, one could interpret Fig. 4.41 in a way, that at the given external forces, calmodulin is in different phase states resp. transition, as the fluctuation strengths and the timescales differ significantly regarding the different external forces (cf. the differently sloped parabolas in Fig. 3.5 as explicated in section 3.4.2).

Reflecting these two approaches on polymer physics, the macroscopic point of view seems to be more convincing, as it already initially predicts this type of "active" behaviour and does not depend on an initial mechanical model of polymers with a thermodynamic model "on top". In particular the fact, that significant contractions of vWF against an outer force occur harmonizes very well with the idea of regarding the system of vWF and the erythrocyte as *one* thermodynamic system which samples different states over time.

4.2.3.2 Distribution of fluctuation strength

In the following, different thermodynamic observables characterizing the states of vWF and their distribution shall be regarded closer. In order to show the generality of the observations, three completely independent experiments will be shown (denoted as A, B and C). The experiments contain overall 1174 states (identified by the algorithm described in 6.2.4) with 525 states in experiment A, 318 in experiment B and 331 in experiment C.

The regarded observables are the average force of a state F_{avg}, the force difference between different states F_{diff} and the persistence time of a state t_{pers}. The force F_{avg} assigned to a certain state is gained by building the average force during the whole persistence of the state. As sometimes, the states identified by the algorithm are not completely flat, but have a certain slope, it might happen, that the force difference F_{diff} is very close to zero against intuition which is a result of the analysis algorithm that identifies the transition between to states by maximum force differences within a short period. Therefore, the fact that the transition is identified by a "short-range" criterion, but the force difference between states is reasonably calculated using the average of the whole state, in case of sloped curves, very tiny steps (F_{diff}) occur. The problem can be visualized by a sloped saw tooth profile. The persistence time t_{pers} is the time between two identified state transitions (c.f. also the closer description of the algorithm in 6.2.4 in the Appendix).

Distribution of force differences between different states
The distribution of F_{diff} is an indicator for the fluctuations occurring in the *statistically* prepared states of the thermodynamic system. The three experiments A, B and C exhibit force differences in positive as well as negative direction (meaning both, a release as well as contraction of free contour length). They cluster around $5 - 10\,\text{pN}$. Still, all experiments reveal rare, but existent force differences in the range of several ten Piconewton which take place in positive as well as negative direction, again meaning release and contraction of free contour length (c.f. Figures 4.42 -4.44).

These observations perfectly harmonize with the idea of vWF sampling different (in principle) accessible states given on its entropy parabola. As a matter of fact, the amount of small fluctuations is largely higher than giant leaps which is a result of either the system being already in equilibrium and undergoing small fluctuations or being prepared *by chance* far from its maximum entropy and sampling several more probable states in small steps. Huge differences in contrast can be only expected in the case of the preparation in a low probable state and a giant leap towards equilibrium or in case of a close-to-equilibrium state fluctuating into a highly improbable state (and back again either through one or several transitions).

Distribution of average forces of different states
As already explained, the experimental design leads to random initial vWF states. It is therefore interesting to see, that the system was realized in most of the cases in a more or less "relaxed" state with only low tension on vWF in the range of less than $30\,\text{pN}$ (*which might be a consequence of a hypothetical higher binding probability in case of "relaxed" conditions*). Nevertheless, still a significant amount of realizations could be observed, where vWF fluctuated

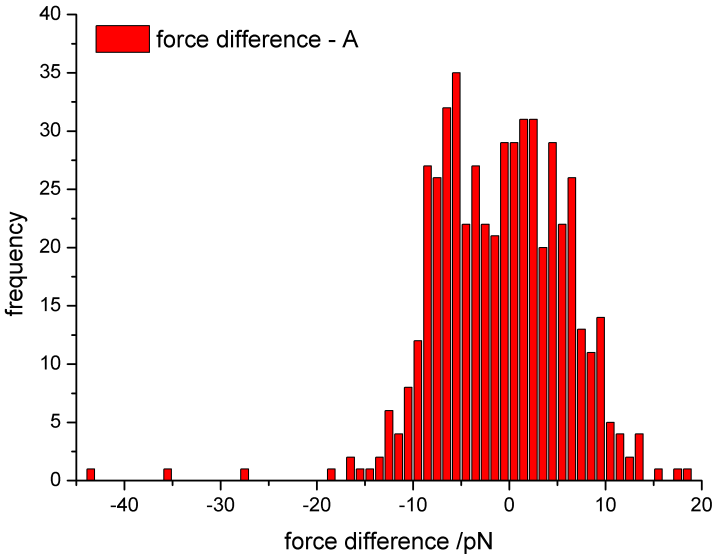

Figure 4.42: Distribution of the force differences F_{diff} that occur at the end of a state - experiment A (525 states) - binsize: 1 pN.

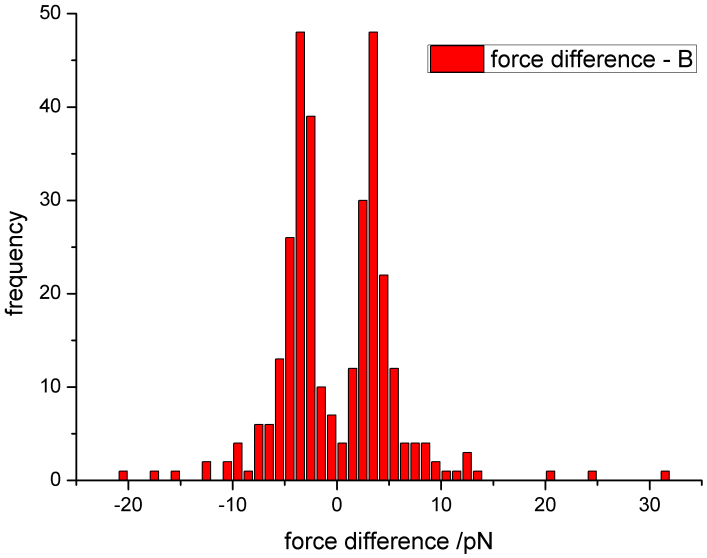

Figure 4.43: Distribution of the force differences F_{diff} that occur at the end of a state - experiment B (318 states) - binsize: 1 pN.

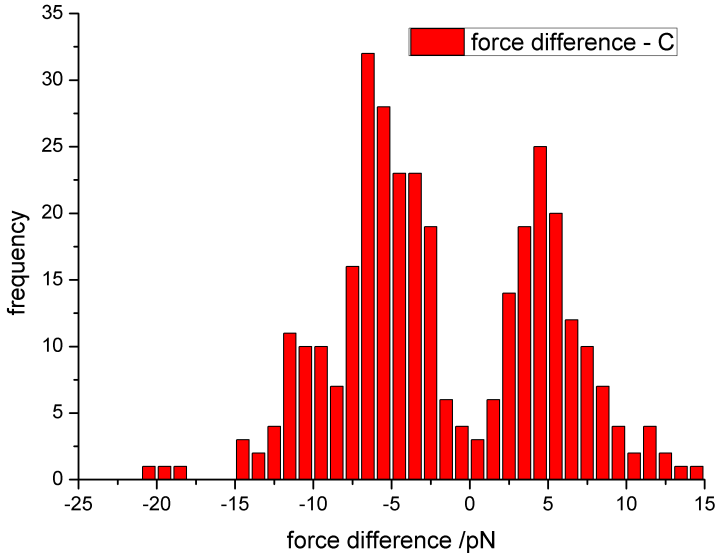

Figure 4.44: Distribution of the force differences F_{diff} that occur at the end of a state - experiment C (331 states) - binsize: 1 pN.

between different states at a high level of external force in the range of $30-80$ pN (c.f. Figures 4.45 -4.47).

These fluctuations taking place under different external forces can be interpreted as the fluctuations occuring in different phase states of vWF. This is due to the fact, that the external force for a molecule (as a 1-dimensional entity) has the same thermodynamic role as the lateral pressure π has e.g. for lipid membranes (2-dimensional systems) or the pressure p has for 3-dimensional systems. Therefore, this experiment can be understood and visualized as if on a film balance, one would restrict a random amount of lipids on a certain area. This would lead to various different phase states of the lipid monolayer which would be connected with different fluctuation strengths (note, that in this picture of the lipid monolayer, the barriers of the film balance would be part of the system participating in the fluctuation process). Therefore, the clusters of events (e.g. in Fig. 4.46 around 40-50 pN) could be interpreted as the states of maximum entropy for the given set of thermodynamic variables around which the fluctuations take part.

Distribution of different persistence times of different states

Also in terms of persistence times t_{pers}, there occur besides the majority of the states that last less than 0.5 s at least a few events that last from 0.5 s up to 2 s (c.f. Figures 4.48 -4.50). According to the idea of the system sampling the entropy parabola, one would expect different fluctuation strengths depending on the thermodynamic state of the system with a certain distribution of the persistence time of different states.

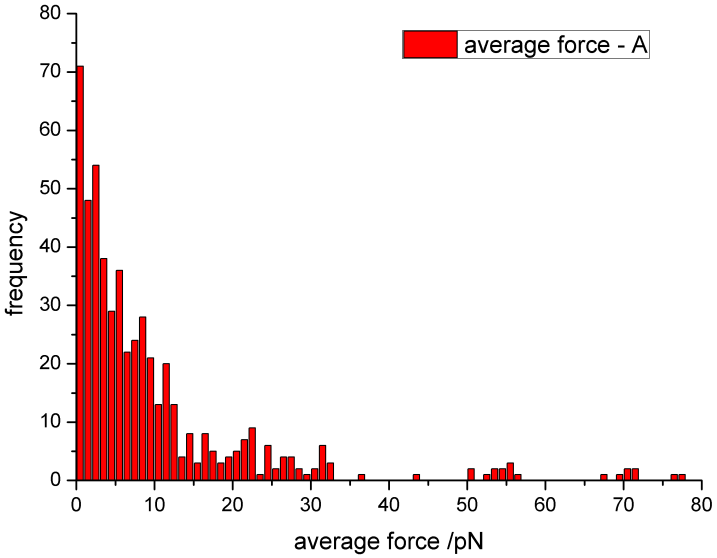

Figure 4.45: Distribution of the average external force on the vWF molecule F_{avg} at a given state - experiment A (525 states) - binsize: 1 pN.

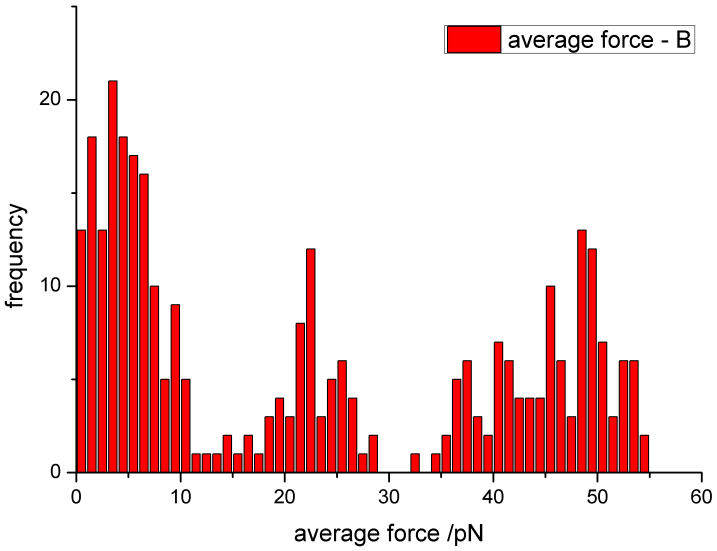

Figure 4.46: Distribution of the average external force on the vWF molecule F_{avg} at a given state - experiment B (318 states) - binsize: 1 pN.

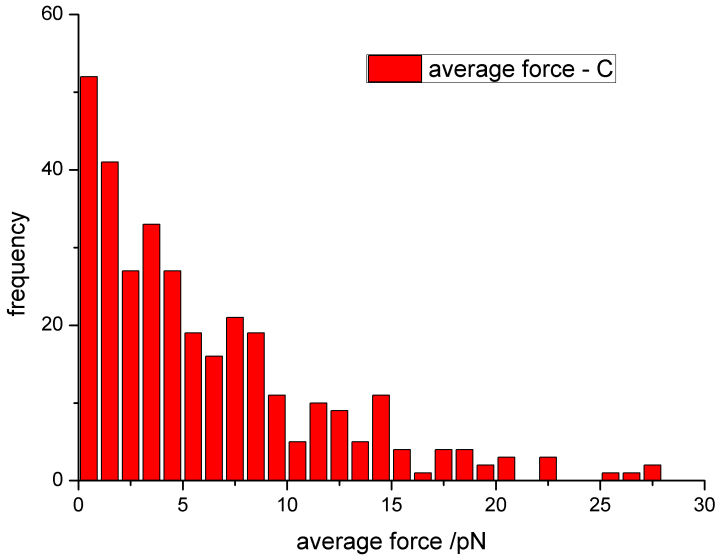

Figure 4.47: Distribution of the average external force on the vWF molecule F_{avg} at a given state - experiment C (331 states) - binsize: 1 pN.

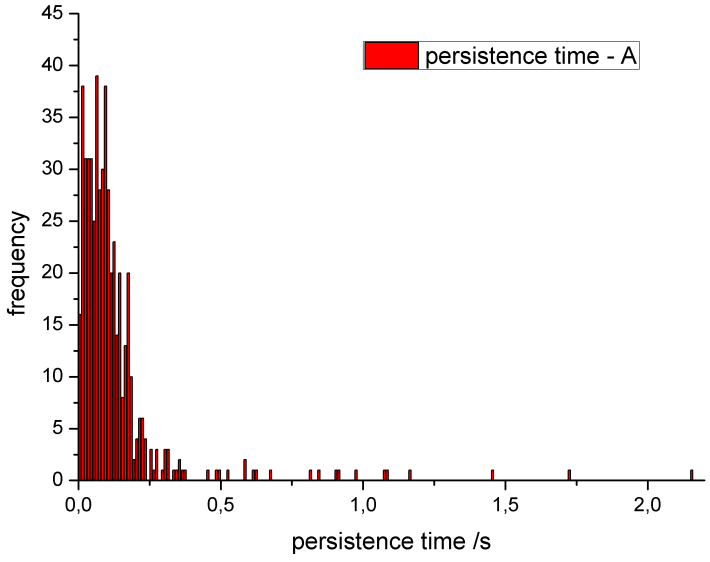

Figure 4.48: Persistence time t_{pers} of the different states - experiment A (525 states) - binsize: 0.01 s.

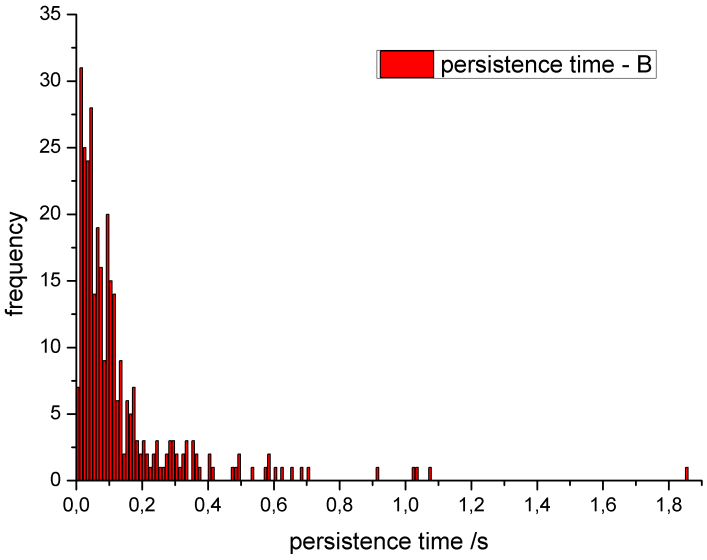

Figure 4.49: Persistence time t_{pers} of the different states - experiment B (318 states) - binsize: 0.01 s.

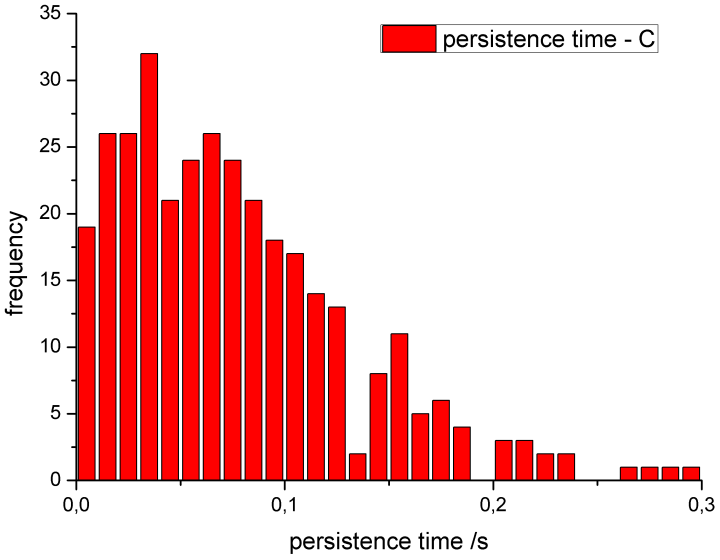

Figure 4.50: Persistence time t_{pers} of the different states - experiment C (331 states) - binsize: 0.01 s.

4.2.3.3 Conclusion of vWF experiments

Overall, all of the presented data harmonize very well with the presented idea of a thermodynamic description and model of polymer physics (cf. section 3.4). Further on, two central predictions of this theory which are reversible transitions between different states (even against an external force from the point-of-view of the vWF molecule) and different fluctuation strengths, both in time and forces, clearly could be observed. Therefore, the author wants to motivate further research in the direction of a thermodynamic description of polymer physics with the viewpoint of polymers constituting a tube-shaped, 2-dimensional (hydrated) interface where the rule of entropy (and the second law) governs the physical processes.

4.3 2D interfacial entropy and cell adhesion

Besides the described approach to polymer physics in terms of 2-dimensional interfaces and entropy fluctuations taking place at those, cell adhesion is a process with very similar physical conditions as it takes place as well at 2-dimensional, hydrated interfaces. Therefore, proper observations on these systems should provide similar outcomes in the patterns of physical observables which is the case as shown in the following.

Cell adhesion is a process that obviously takes place at interfaces. Either between two biological systems (e.g. two different cells) which is usually explained with "receptor-binding" or between biological and non-biological matter where the term of "non-specific interactions" is applied. Both explanations refer to microscopic pictures of physical reality (cf. 3.2). Based on the idea of proper 2D interfacial entropy presented in section 3.4, the question emerges whether cell adhesion in general can be described with such a macroscopic and phenomenological approach. A major characteristics of this theory is the omnipresence of fluctuations, whether the observed system is in equilibrium or not. Therefore, a striking indicator for the suitability of this theory to explain cell adhesion processes beyond pure reasoning was the publication Marx et al. (2002). Fig. 4.51 (b) shows the fluctuations of the distance between an artificial membrane and a substrate (therefore, we observe nothing else but the fluctuation of entropy with regard to distance as the thermodynamic variable).

These patterns strongly remind to the patterns observed regarding polymer length (cf. part 4.2.3.1 and in particular Fig. 4.39), to the patterns observed in terms of (blinking) enzyme activity at 2-dimensional hydrated interfaces (cf. Fig. 4.52, Lu et al. (1998) and Nuschele (2010) where this observation is embedded into the theory of enzyme activitiy from a thermodynamic perspective) and even to the patterns observed in the behaviour of so-called ion channels (cf. e.g. Fig. 3.6 and Wunderlich et al. (2009)) which are as well proteins embedded into membranes and therefore again a system of 2-dimensional hydrated interfaces.

Most of the present, commonly accepted approaches to the systems described above state microscopic points of view in the sense of either regarding molecular behaviour (ion channels, polymers, enzymes) or single specific interaction mechanisms (cell adhesion).

A phenomenological approach that would fulfill the requirements of Einstein's reversion (see section 3.4) in contrast would make use of macroscopic

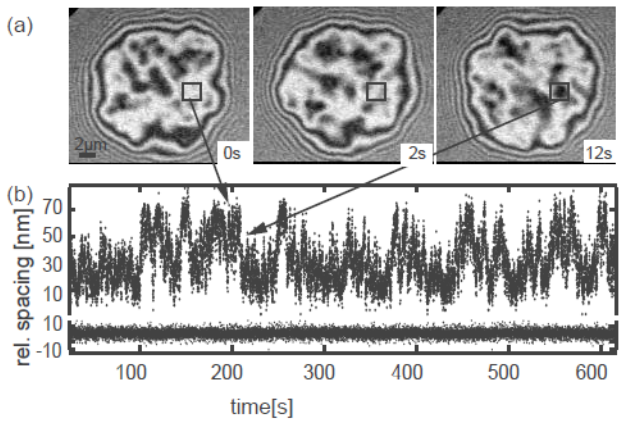

Figure 4.51: Fluctuations of the distance between a membrane and a substrate. Picture (a) shows a reflex interference contrast microscopy (RICM) image of the whole vesicle, (b) shows the fluctuations between membrane and substrate at a certain point in space over time. Image taken from Marx et al. (2002).

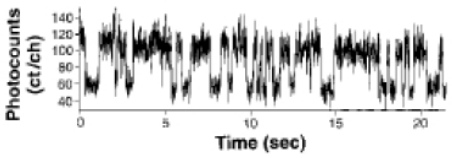

Figure 4.52: Photocounts over time of the enzyme cholesterol oxidase. The emitted photons are connected with enzyme activity ("blinking" enzyme activity), cf. Lu et al. (1998).

observations of a whole system instead of microscopic ones. Now, as all these systems take place at 2-dimensional hydrated interfaces and in all systems the observations are similar, this is a strong hint for a common underlying physical law which might be seen in the idea of proper 2D interfacial entropy as described in section 3.4. Therefore, also the integration of the phenomenon of cell adhesion into the framework of this theory seems to be a promising idea.

Although the studies performed with DANI so far are far away from confirming this approach, there still are already several hints pointing out into this direction. In particular, the following experiments (cf. section 4.1.2) suit very well with these ideas.

Initial adhesion time and time of flow exposure
Regarding initial adhesion time, the results show that for longer initial adhesion time the number of attached cells becomes bigger. Further on, the longer the cells are exposed to the flow, the more will be detached and the shorter the initial adhesion time, the higher the detach rate. All these observations seem to be pretty intuitive but still it is to state that they also fit very well with the idea of sampling different states on the entropy parabola. Initial adhesion here would constitute a (artificially prepared) very improbable state. For a given set of external thermodynamic variables, the cell will sample different states of higher entropy until it finally reaches the entropy maximum. Therefore, the more time an ensemble of cells is placed on the sample surface, the more will (statistically) reach the entropy maximum. Deadhesion again works very well in this picture as an outer force will flaten the parabola significantly. The thermodynamic system of adhered cells will now undergo very high fluctuations and therefore, the probability of reaching a nearly non-bound state increases. Therefore, the longer the cell ensemble is exposed to the flow, the more cells can reach states far away from the maximum. For shorter initial adhesion times, the ensemble is already wider distributed when the switching-on of the flow changes the parabola and therefore, the far-out states can be reached faster. Notice, that the very moment of detaching eliminates the whole thermodynamic system and therefore is a critical event which eludes from a description by this theory.

Different implant sample materials
From the materials point of view within the present study, one can only state, that for the four different materials one finds different initial adhesion values that could be interrelated to the slope of the entropy parabola. In terms of deadhesion, as already explained above (cf. part 4.1.2.7) there probably occurs a toxic effect (in case of Ag-doped surfaces) for the cells which again would destroy the thermodynamic system as regarded in the beginning. Therefore, a critical experiment which would be able to falsify the presented theory, would be to test the fluctuation strength of cells on various surfaces (with uncritical properties for the cell metabolism!) and compare initial adhesion with fluctuation strength. The higher the fluctuations, the lower the initial adhesion affinity and vice versa. This experiment indeed would be highly interesting in order to check, whether to tread this path of cell adhesion description further on or not.

pH value variations
The pH measurements give a strong hint into the direction of the necessity of a thermodynamical view on these experiments. Within a moderate range of $\Delta\text{pH} \leq 2.1$ around the physiological conditions of $\text{pH} = 7.4$ the initial adhesion values are for the same pH deviation into the acidic direction slightly higher than for the deviation into the alkaline regime. The same effect, even more prominent to observe occurs in the deadhesion measurements. Deviations into the alkaline regime tend to cause a higher deadhesion rate which might be a result of a thinkable state change of the 2-dimensional interface (and therefore a significant change in the slope of the entropy parabola).

Changes in ambient temperature
Probably the most interesting results with regard to thermodynamic variables are those about temperature changes. Both, initial adhesion as well as deadhesion under flow exhibit strongly asymmetric behavior with respect to temperature changes away from physiological conditions with $T = 37°\text{C}$. For a temperature change of $T = \pm 6°\text{C}$, initial adhesion reaches 96% compared to physiological conditions in the case of cooling. In the case of a temperature rise, initial adhesion ends up at only 60%. As stated above, commonly this would be explained by the denaturation of membrane proteins ignoring the effects on the cell membrane.

Therefore, a theory which integrates proteins and the membrane, but much more, all the other possible external variables like e.g. pH, substrate (for adhesion) and time would be a significant progress in cell adhesion research. The crucial experiment described above providing the possibility of falsification is therefore highly desirable.

Chapter 5

Summary and Outlook

Adhesion and biological interfaces were studied from two different points of view. Driven by the desire of improved implant surface materials, a novel device for implant research was developed which allows the study and dynamic analysis of cell adhesion and detachment processes, the De-Adhesion Number Investigator DANI. It makes very short measuring times accessible, enables the operator to simulate various altered physiological conditions, is very flexible in terms of implant sample material (no requirements e.g. on optical, mechanical or electrical properties) and is very cost-effective, which all states an enormous advantage compared to present-state animal tests which are often applied in clinical research. The tool is based on the well-established surface acoustic wave (SAW)-driven microfluidics technology (cf. also Hartmann et al. (2013)). Several adhesion experiments with respect to different implant samples as well as to altered physiological conditions were carried out *en passant* serving as a proof-of-principle. Based on the initial design, further geometries of the actuators for the microfluidic flow were tested which opens a wide range of potential applications as the properties of the flow (e.g. homogeneous, inhomogeneous) can be adapted to the particular requirements of a given experiment.

A quite different approach to study biological interfaces was taken by single-molecule force spectroscopy experiments using the BioForceProbe (BFP) technique (cf. Evans et al. (1995)). Here, the blood-borne protein vWF was fixed at two spots, set under a certain pre-tension and observed with respect to the force which it applies to an external force sensor. This setup was interpreted as a tube-shaped, 2-dimensional interface between the molecule and the surrounding water. Following this idea, the system was analyzed from the point of view of thermodynamics whereat a thermodynamic approach was chosen which is based on the ideas of Einstein's reversion and proper 2D entropy at interfaces. Central predictions of this approach include, that the system would undergo various fluctuations in thermodynamic observables depending on its thermodynamic state. These predictions clearly could be confirmed which opens the possibility of integration of polymer physics into the quoted thermodynamic model.

Beyond that, cell adhesion experiments with altered physiological conditions were carried out with the DANI system (cf. above) which as well exhibited potential for a deeper insight of the physical foundations of cell adhesion again using the described idea of thermodynamics at interfaces. From the point of

view of integration of cell adhesion into this model, these first experiments, in particular those with temperature and pH variations, showed promising results. For a more thorough foundation of this hypothesis of being able to integrate cell adhesion into this model, a crucial experiment was suggested which includes clear predictions and therefore the *chance* of falsification.

Chapter 6

Appendix

6.1 De-Adhesion Number Investigator DANI - Cell culture media

The cell cultures used for the presented studies were primary human osteoblasts and SAOS-2 cells (c.f. section 4.1.2.1). The human osteoblasts were sustained using a culture medium which friendly was provided by AG Dr. Burgkart, "Klinikum rechts der Isar", München, Germany.

The medium for the SAOS-2 cells consisted of 500 ml DMEM medium with stable glutamine, 3.7 $\frac{g}{l}$ $NaHCO_3$, 1.0 $\frac{g}{l}$ D-glucose from Biochrom with several additives that were:

- 50 ml fetal calf serum (FBS Superior, S 0615, Biochrom)
- 10 ml HEPES 1 M (L 1613, Biochrom)
- 5 ml L-glutamine 200 mM (K 0283, Biochrom)
- 5 ml MEM vitamins 100x (K 0373, Biochrom)
- 1 ml Primocin (ant-pm-2, Invivogen)

6.2 BioForceProbe (BFP) technique

6.2.1 Glass pipettes

Each experiment on the BFP requires three glass pipettes with a narrowing tip and a termination diameter of $\approx 2\,\mu$m (cf. Fig.6.1). They were pulled using glass tubes (Single Barrel Borosilicate Capillary Glass, outer diameter 0.75 mm, A-M Systems Inc.) on a micropuller (Model P-87, Sutter Instruments Co., CA) and a micro forge which was hand-crafted by the Prof. Evan Evans crew from the University of British Columbia, Vancouver & Boston University, Boston, MA.

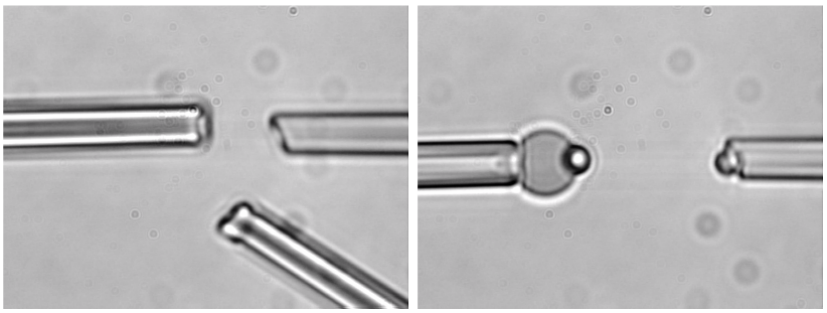

Figure 6.1: Exemplary set of glass pipettes for the performance of a BFP experiment; left: three pipettes where the lower right only serves for preparation purposes, namely to place the probe bead on the surface of the red blood cell; right: initial situation of a BFP experiment with the red blood cell and the probe bead on the left side and the target bead on the right side.

6.2.2 Erythrocyte preparation

As described in section 4.2.2.1, the force sensor for the BFP technique is a (physico-chemically altered) human erythrocyte or red blood cell (RBC). It is prepared by the following procedure:

1. 8-10 μl (one droplet) of fresh blood is obtained using a lancet on the fingertip. The blood was obtained from a 27-year-old, male Bavarian-Swabian human donor of Roman Catholic denomination, living on vegetarian diet. Donor could take up nutrients *ad libitum*. No permanent harm was caused due to this process.

2. the blood is washed three times using a 0.1M carbonate-bicarbonate buffer of pH = 8.5; after mixing the blood with the buffer, the liquid mixture is spinned at 4000 rpm for $\approx$ 45 seconds in a micro-centrifuge after each step and further on resuspended in the buffer; after the last wash, the RBCs are left as a pellet by removing all supernatant.

3. the RBCs are **biotinylated** by incubation with 1 ml of a 0.28 mM solution of NHS-PEG3500-biotin (JenKem; m.wt. $\approx$ 3600) in coating buffer for 30 minutes at room temperature. The solution is gently mixed using a vertical spinning disc which rotates with $\approx$ 0.5 Hz.

4. after biotinylation, the RBCs are washed again three times following the same procedure as described above (step 2).

5. the biotinylated RBCs are **streptavidinated** by adding a pellet of 2 μl RBCs to a solution consisting of 50 μl HEPES buffer (10 mM, pH=7.4) with NaCl (158 mOsm) and 5 % bovine serum albumin (BSA) (further on HEPES-158-BSA) and 5 μl streptavidin solution (2 $\frac{\text{mg}}{\text{ml}}$).

6. the solution is gently mixed and incubated for 30 minutes again on a vertical spinning disc according to step 3.

7. the streptavidinated RBCs are washed (according to step 2) three times with HEPES-158-BSA.

8. for storage, the RBCs are resuspended in 50 μl HEPES-158-BSA and kept at 4°C until use.

The RBCs treated this way are able to undergo a very strong binding to glass beads treated with biotin via a biotin-streptavidin-biotin binding which is one of the strongest non-covalent bindings known in biochemistry (cf. Green (1975)).

6.2.3 Bead preparation

As shown in section 4.2.2.1, the BFP experiments require two kinds of glass beads, one coated with the molecule of interest and the other one with a corresponding antibody. The one kind for the probe side which is glued on the RBC additionally needs to be treated with biotin, cf. also the precedent described erythrocyte preparation. Both kinds of beads need an initial surface treatment in order to enable the biochemical coating. This initial surface treatment in thoroughly described in Merkel et al. (1999). In short, the glass beads are silanized using 3-mercapto-propyl-trimethoxysilane (MPTMS) in an acetic acid acidified reaction. This aims to covalently anchor -SH-groups to the glass surface to enable further chemical bonding.

6.2.3.1 Probe side

The beads on the probe side used in the presented experiments were prepared the following way:

1. 2 μl of a vWF stock solution ($c = 0.672\,\frac{\mathrm{g}}{\mathrm{l}}$; vWF (wild type) friendly was provided by the group of Prof. Dr. Reinhard Schneppenheim, Universitätsklinikum Hamburg-Eppendorf, Germany) are diluted in 48 μl of carbonate-bicarbonate buffer of pH = 8.5.
2. 10 % of this solution gets mixed with each 2.5 μl of polyethylene glycol (PEG) linkers (Maleimide-PEG-N-Hydroxysuccinimide (MAL-PEG3.5k-NHS) and Maleimide-PEG-Biotin (MAL-PEG3.5k-Biotin), both JenKem Technology, USA) and diluted with 40 μl of carbonate-bicarbonate buffer (pH = 8.5).
3. this mixture reacts chemically for 30 minutes under gentle mixing at room temperature.
4. in a new tube, 0.5 mg of silanized glass beads get suspended in 250 μl of straight phosphate buffer (pH = 6.9).
5. the 50 μl of the solution with the PEG linkers prepared before are added to the glass beads and react at room temperature for $t > 12$ h.
6. after this reaction time, the beads are spinned in a micro-centrifuge for 10 minutes at $T = 4$°C.
7. the supernatant gets removed and the beads are washed with HEPES buffer (10 mM, pH=7.4) with NaCl (158 mOsm) and get spinned again under cool conditions; this step is repeated two times.
8. finally, the beads get resuspended in 50 μl HEPES buffer and stored at $T = 4$°C until use.

6.2.3.2 Target side

The beads for the target side are created in principle in the same way except that they don't get biotinylated and that instead of vWF, its antibody is covalently bond to the surface. As antibody, vWF Polyclonal Rabbit Anti-human von Willebrand factor from Dako GmbH, Germany was used. $5\,\mu$l of the stock solution of $c = 3.1\,\frac{\mathrm{g}}{\mathrm{l}}$ was diluted in $45\,\mu$l of carbonate-bicarbonate buffer of pH = 8.5. $2.66\,\mu$l of this solution was mixed with another $2.34\,\mu$l of carbonate-bicarbonate buffer and $5\,\mu$l of polyethylene glycol (PEG) linkers (MAL-PEG3.5k-NHS, JenKem Technology, USA) were added. To this solution, another $40\,\mu$l of carbonate-bicarbonate buffer was added. From this very point on, the procedure is exact the same as from bullet point 3 on described in the probe bead preparation above.

6.2.4 Algorithm for data analysis

The algorithm for the analysis of the data and in particular for the passive phase (cf. phase III, Fig. 4.38) was written in SciLab. The basic version was initially designed for analysis of vWF stretching data obtained from AFM experiments. The basic version and to a large extent the adaptation to the new data structure was friendly provided by Dominik Breyer, EP I, Augsburg University. In order to detect distinct states of vWF during the passive phase, a sequence of criteria is applied to the data. There are three types of events defined in the passive phase. "Up-steps", "down-steps" and "plateau phases". Plateau phases are defined as the periods between steps; the steps are identified as explained in the following in bullet point form:

- calculation of the STDV of the experiment in the state with no external force on the erythrocyte-bead pair.
- check $\Delta x > 3.7 \cdot STDV$ for two points within $\Delta t = 13.33\,\mathrm{ms}$.
- check $\Delta\overline{x} > 1.7 \cdot STDV$ for the local mean values $\overline{x}_1$ and $\overline{x}_2$ within $t = 10\,\mathrm{ms}$.
- combine steps to one event in case they appear within $t = 60.66\,\mathrm{ms}$.
- identify min/max within the event which finally defines step size, time and kind (up/down).

This algorithm leads to a series of steps which define the plateaus in between. This might lead to "sloped" plateaus. Further on, there were cases of non-identified jumps that a human observer would have identified, which leads to the omission of events (type I error). Nonetheless, this omission assures high quality of the remaining data. Further on, a final quality check for the data was applied which considered and filtered out obvious meaningless data. The criteria were a positive value for the average force plateau, a "drift limit" for the data which requires plateaus with slopes constrained to $\frac{\Delta F}{\Delta t} < \left|100\,\frac{\mathrm{pN}}{\mathrm{s}}\right|$ and the necessity of a force relaxation $\Delta F > 15\,\mathrm{pN}$ in the retracting phase (phase IV, cf. Fig. 4.38) to ensure of *having had* a binding between vWF and its antibody and of *having broken* this binding at the end of the experiment. This series of criteria serves for considering only "high quality" cycles for data analysis, yet

to the price of omitting several cycles which seem to be trustworthy to a human observer.

6.2.5 Exemplary vWF measurements

In the following, a reasonable selection of representative passive observations of fluctuating vWF shall be given (only phase III, the passive observation will be depicted). One can observe a broad variety of vWF behaviour ranging from long persistent states and high external forces to very large fluctuations and low external forces (cf. Fig. 6.2 - Fig. 6.21).

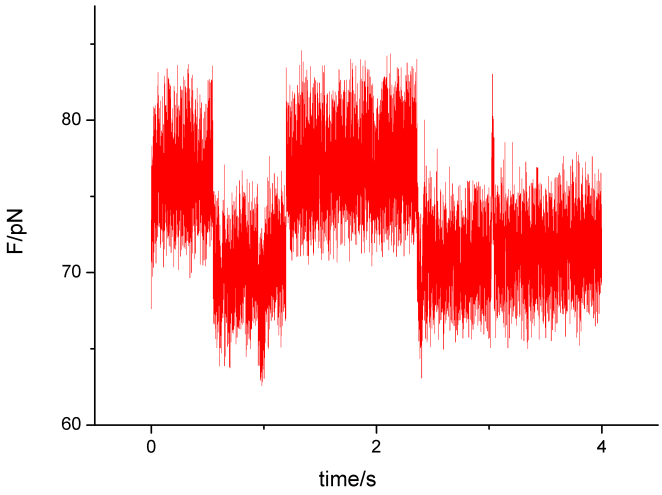

Figure 6.2: A representative passive fluctuation phase from experimental set A; this particular measurement is the one already shown in part 4.2.3.1, note, here only phase III is depicted; this case exhibits relatively long, stable states at a relatively high external force.

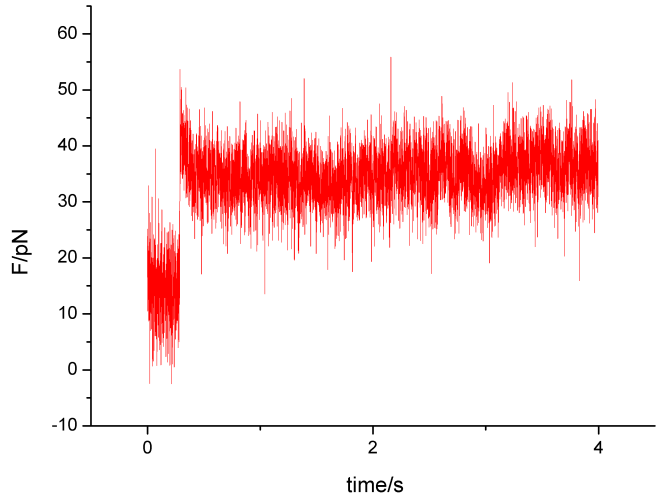

Figure 6.3: A representative passive fluctuation phase from experimental set A; this case exhibits a large force increase at the sensor meaning a reduction of vWF length *against* an external force leading to a relatively long, stable state at a medium high external force.

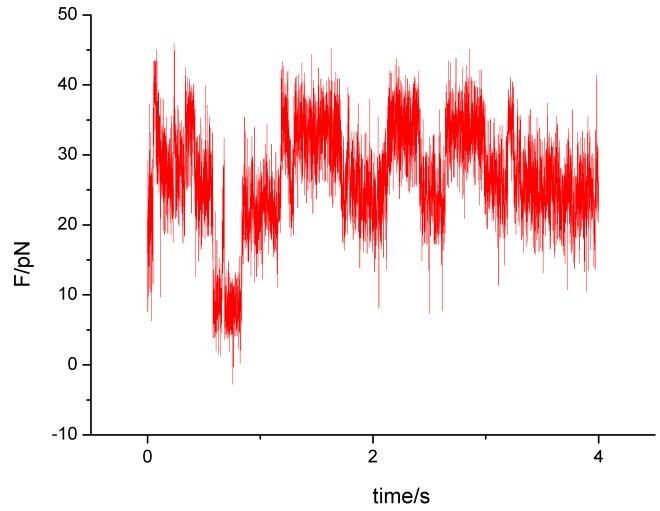

Figure 6.4: A representative passive fluctuation phase from experimental set A; this case exhibits states of medium stability in time at medium large external forces.

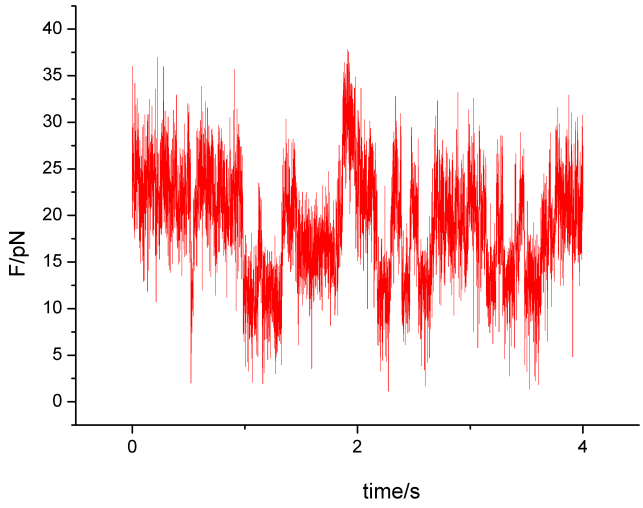

Figure 6.5: A representative passive fluctuation phase from experimental set A; this case exhibits pretty fast fluctuations between different states at rather low external forces.

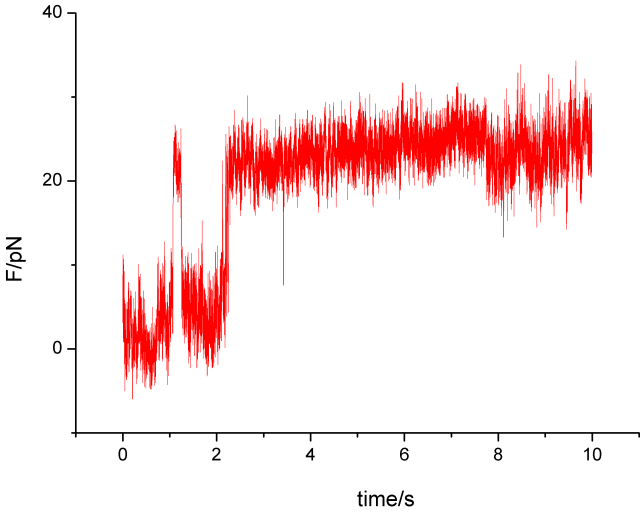

Figure 6.6: A representative passive fluctuation phase from experimental set B; a conclusive interpretation of this case is that vWF occupies a rather stable state which is reached against external force.

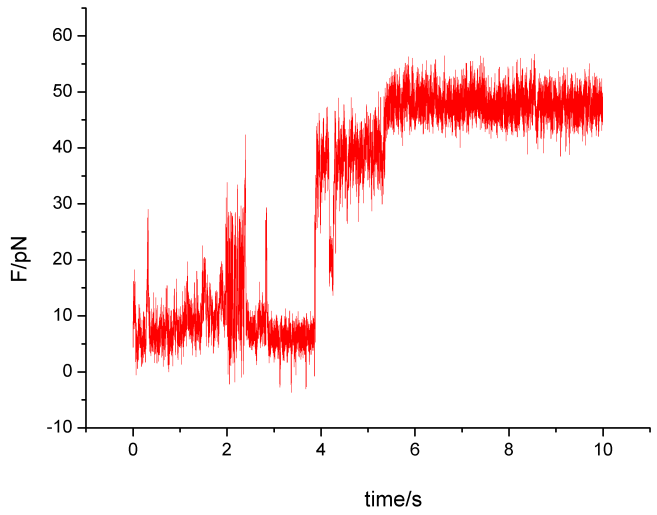

Figure 6.7: A representative passive fluctuation phase from experimental set B. This case reminds of the preceding one with the same effect but even more prominent.

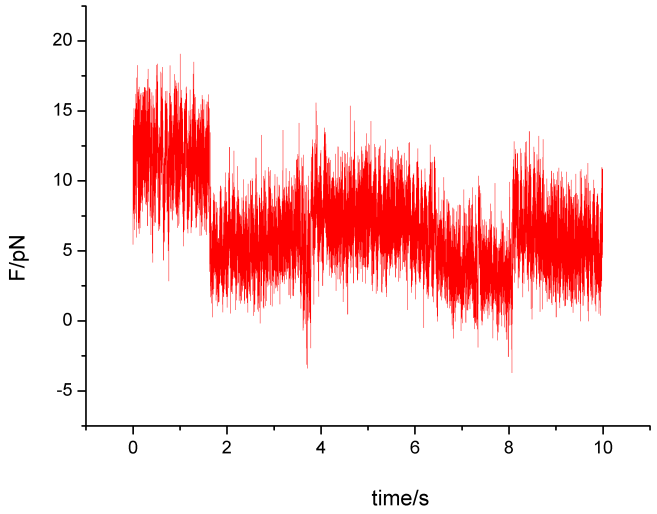

Figure 6.8: A representative passive fluctuation phase from experimental set B; quite stable states with respect to time.

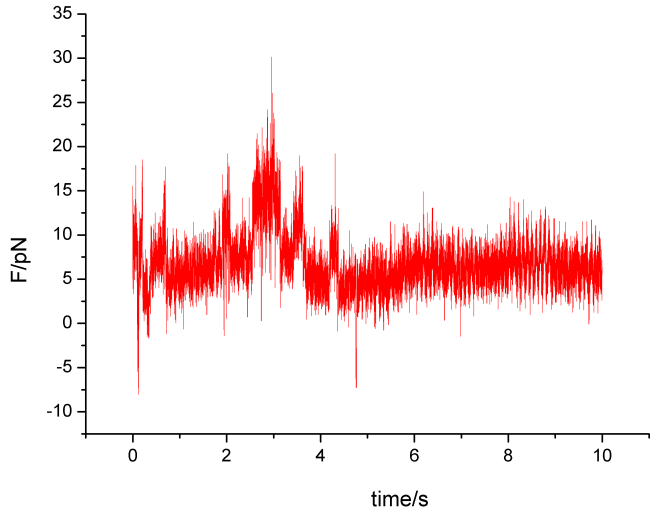

Figure 6.9: A representative passive fluctuation phase from experimental set B; pretty high fluctuations at low external force.

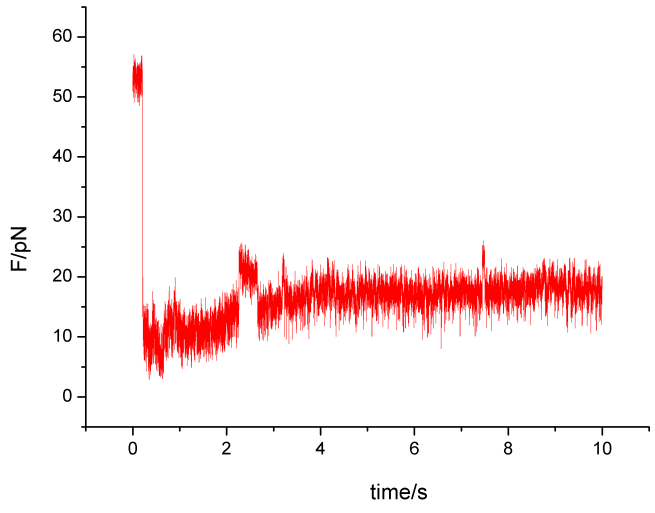

Figure 6.10: A representative passive fluctuation phase from experimental set B.

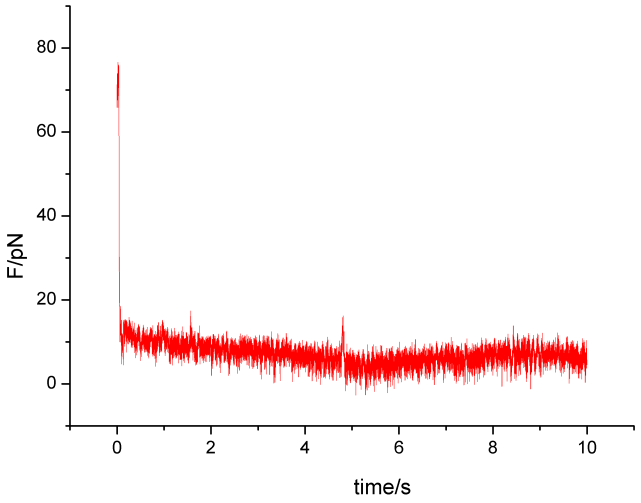

Figure 6.11: A representative passive fluctuation phase from experimental set B.

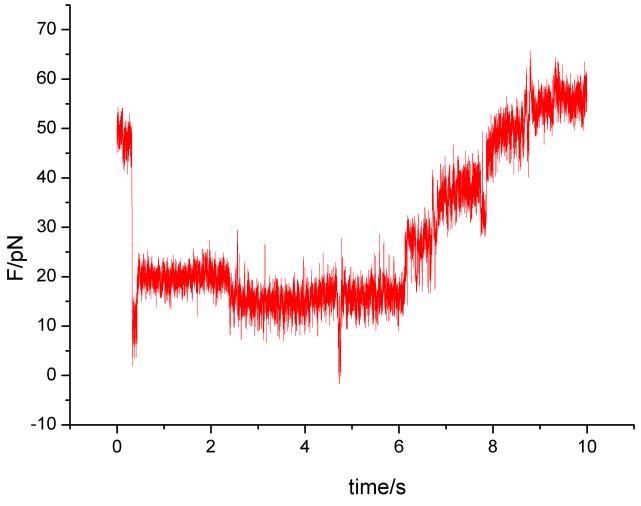

Figure 6.12: A representative passive fluctuation phase from experimental set B; this case exhibits first a large transition between two states which is later on again occupied via several small transitions.

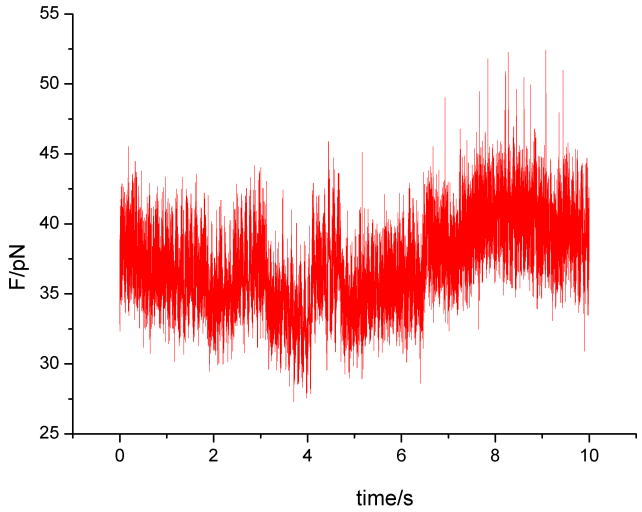

Figure 6.13: A representative passive fluctuation phase from experimental set B; note the pretty high external force.

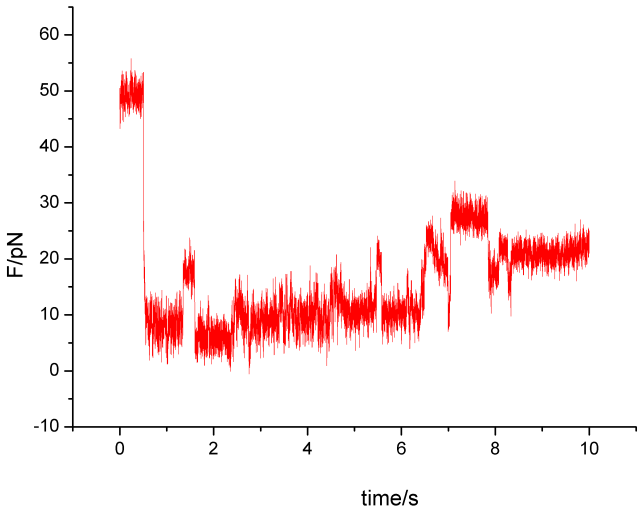

Figure 6.14: A representative passive fluctuation phase from experimental set B.

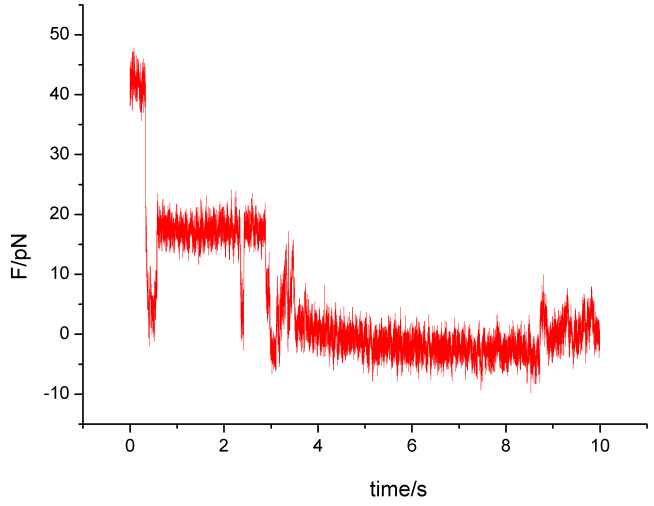

Figure 6.15: A representative passive fluctuation phase from experimental set B.

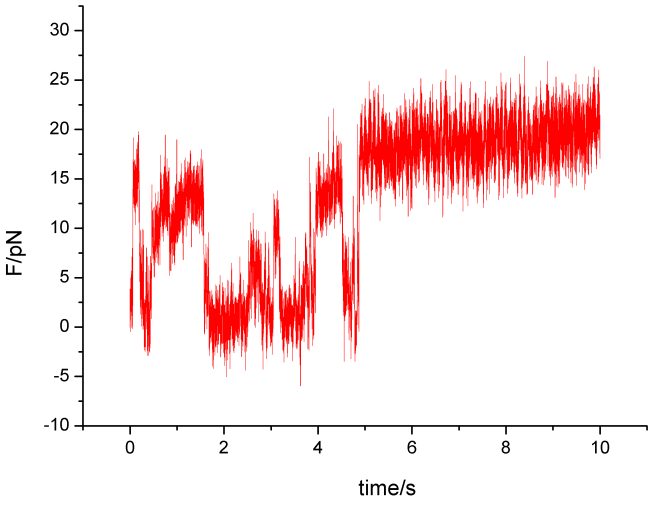

Figure 6.16: A representative passive fluctuation phase from experimental set B.

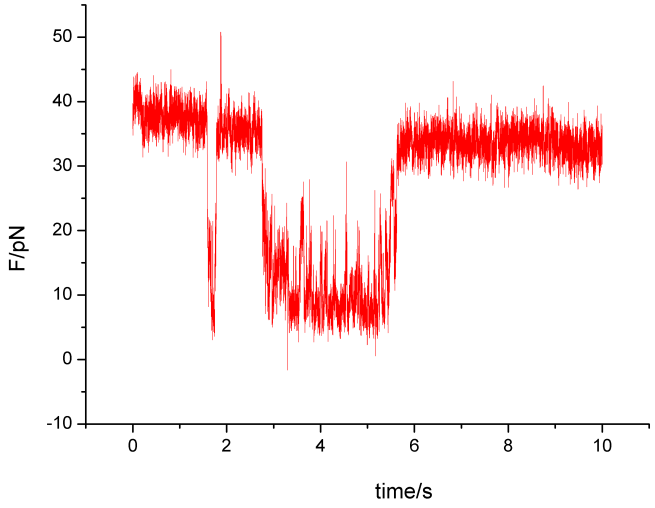

Figure 6.17: A representative passive fluctuation phase from experimental set B.

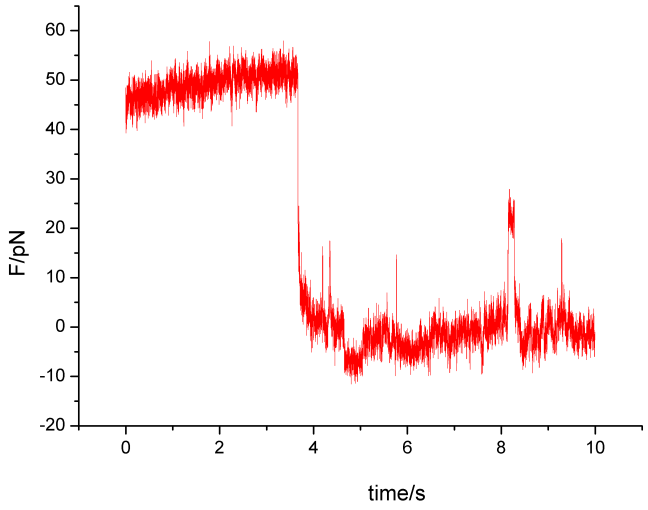

Figure 6.18: A representative passive fluctuation phase from experimental set B.

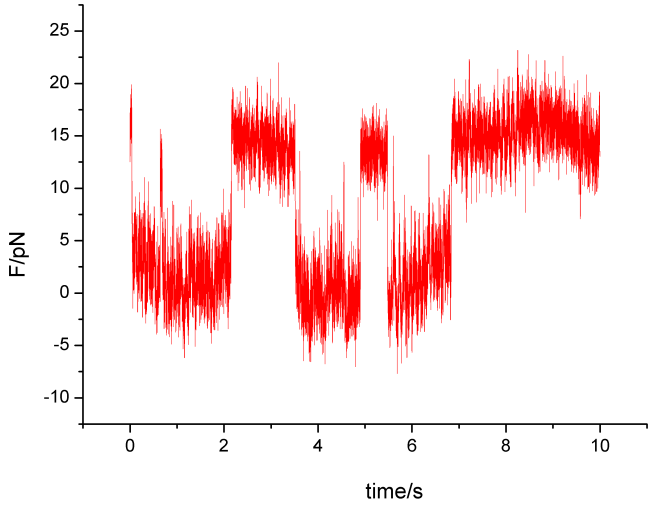

Figure 6.19: A representative passive fluctuation phase from experimental set B.

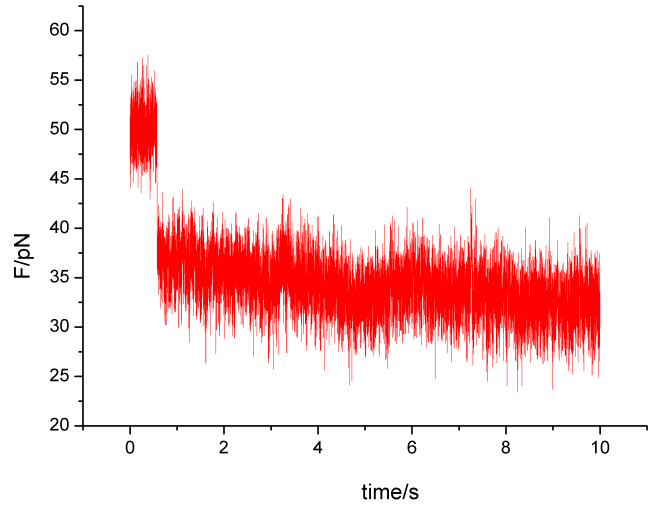

Figure 6.20: A representative passive fluctuation phase from experimental set B.

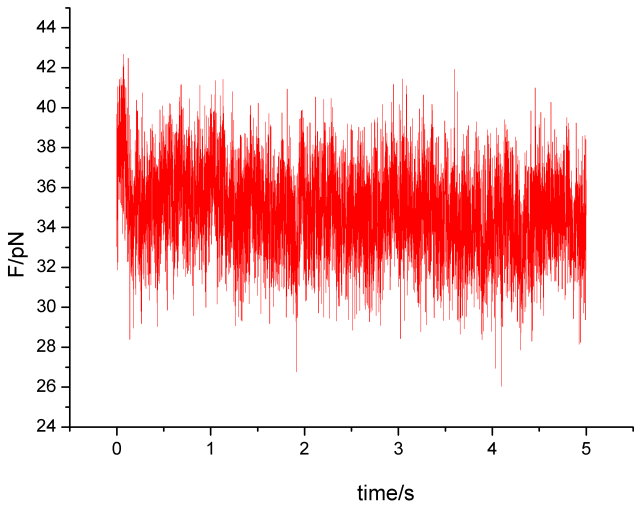

Figure 6.21: A representative passive fluctuation phase from experimental set C; this case exhibits a quite stable situation at medium high external forces.

Bibliography

Allen, M., Myer, B., and Rushton, N. (2001). In Vitro and In Vivo Investigations into the Biocompatibility of Diamond-Like Carbon (DLC) Coatings for Orthopedic Applications. (DLC):319–328.

Boisselier, E. and Astruc, D. (2009). Gold nanoparticles in nanomedicine: preparations, imaging, diagnostics, therapies and toxicity. *Chemical Society Reviews*, 38(6):1759–1782.

Bruinsma, R., Behrisch, a., and Sackmann, E. (2000). Adhesive switching of membranes: experiment and theory. *Physical review. E, Statistical physics, plasmas, fluids, and related interdisciplinary topics*, 61(4 Pt B):4253–4267.

Casals, E., Gonzalez, E., and Puntes, V. F. (2012). Reactivity of inorganic nanoparticles in biological environments: insights into nanotoxicity mechanisms. *Journal of Physics D: Applied Physics*, 45(44):443001.

Chen, H., Fallah, M. a., Huck, V., Angerer, J. I., Reininger, A. J., Schneider, S. W., Schneider, M. F., and Alexander-Katz, A. (2013). Blood-clotting-inspired reversible polymer-colloid composite assembly in flow. *Nature communications*, 4:1333.

Clausius, R. (1865). Über verschiedene für die Anwendung bequeme Formen der Hauptgleichungen der mechanischen Wärmetheorie. *Annalen der Physik*, pages 353–400.

Cummings, R. K. (1922). *The Girl in the Golden Atom*.

de Gennes, P.-G. (1979). *Scaling Concepts in Polymer Physics*. Cornell University Press, Ithaca.

Despopoulos, A. and Silbernagl, S. (2003). *Color Atlas of Physiology*, volume 5. Georg Thieme Verlag.

Ding, X., Li, P., Lin, S.-C. S., Stratton, Z. S., Nama, N., Guo, F., Slotcavage, D., Mao, X., Shi, J., Costanzo, F., and Huang, T. J. (2013). Surface acoustic wave microfluidics. *Lab on a chip*, 13(18):3626–49.

Ding, X., Lin, S.-C. S., Kiraly, B., Yue, H., Li, S., Chiang, I.-K., Shi, J., Benkovic, S. J., and Huang, T. J. (2012). On-chip manipulation of single microparticles, cells, and organisms using surface acoustic waves. *Proceedings of the National Academy of Sciences of the United States of America*, 109(28):11105–9.

DSMZ (2013). Cell line: SAOS-2, http://www.dsmz.de/catalogues/details/culture/ACC-243.html, 11.02.2013.

Einstein, A. (1905). Über die von der molekularkinetischen Theorie der Wärme geforderte Bewegung von in ruhenden Flüssigkeiten suspendierten Teilchen. *Annalen der Physik*, 17:549 – 560.

Einstein, A. (1910). Theorie der Opaleszenz von homogenen Flüssigkeiten und Flüssigkeitsgemischen in der Nähe des kritischen Zustandes. *Annalen der Physik*, 33:1275–1298.

Evans, E., Heinrich, V., Leung, A., and Kinoshita, K. (2005). Nano- to microscale dynamics of P-selectin detachment from leukocyte interfaces. I. Membrane separation from the cytoskeleton. *Biophysical journal*, 88(3):2288–98.

Evans, E., Ritchie, K., and Merkel, R. (1995). Sensitive force technique to probe molecular adhesion and structural linkages at biological interfaces. *Biophysical journal*, 68(6):2580–7.

Fallah, M. a., Myles, V. M., Krüger, T., Sritharan, K., Wixforth, a., Varnik, F., Schneider, S. W., and Schneider, M. F. (2010). Acoustic driven flow and lattice Boltzmann simulations to study cell adhesion in biofunctionalized mu-fluidic channels with complex geometry. *Biomicrofluidics*, 4(2):1–10.

Fichtl, B. (2015). Integration der Biochemie in die Physik der Grenzfläche. *Dissertationsschrift Universität Augsburg*.

Fichtl, B., Shrivastava, S., and Schneider, M. F. (2016). Protons at the speed of sound: Predicting specific biological signaling from physics. *Scientific Reports*, 6:22874.

Fillafer, C., Ratzinger, G., Neumann, J., Guttenberg, Z., Dissauer, S., Lichtscheidl, I. K., Wirth, M., Gabor, F., and Schneider, M. F. (2009). An acoustically-driven biochip - impact of flow on the cell-association of targeted drug carriers. *Lab on a chip*, 9(19):2782–8.

Fowler, W. E., Fretto, L. J., Hamilton, K. K., Erickson, H. P., and McKee, P. a. (1985). Substructure of human von Willebrand factor. *The Journal of clinical investigation*, 76(4):1491–500.

Friend, J. and Yeo, L. Y. (2011). Microscale acoustofluidics: Microfluidics driven via acoustics and ultrasonics. *Reviews of Modern Physics*, 83(2):647–704.

Frommelt, T., Kostur, M., Talkner, P., and Hänggi, P. (2008). Flow Patterns and Transport in Rayleigh Surface Acoustic Wave Streaming : Combined Finite Element Method and Raytracing Numerics versus Experiments. 55(10):2298–2305.

Gekle, S. (2015). Wasser in Grenzen. *Physik Journal*, 14(11).

Glaser, R. (1986). *Biophysik*. Gustav Fischer Verlag, Stuttgart, third edition.

Goennenwein, S. (2003). Generic and Specific Cell Adhesion: Investigations of a Model System by Micro-Interferometry. *Dissertationsschrift Technische Universität München*.

Goennenwein, S., Tanaka, M., Hu, B., Moroder, L., and Sackmann, E. (2003). Functional incorporation of integrins into solid supported membranes on ultrathin films of cellulose: impact on adhesion. *Biophysical journal*, 85(1):646–55.

Green, N. M. (1975). *Advances in Protein Chemistry Volume 29*, volume 29.

Griesbauer, J., Bössinger, S., Wixforth, a., and Schneider, M. F. (2012a). Propagation of 2D Pressure Pulses in Lipid Monolayers and Its Possible Implications for Biology. *Physical Review Letters*, 108(19):198103.

Griesbauer, J., Bössinger, S., Wixforth, a., and Schneider, M. F. (2012b). Simultaneously propagating voltage and pressure pulses in lipid monolayers of pork brain and synthetic lipids. *Physical Review E*, 86(6):061909.

Griesbauer, J., Wixforth, a., and Schneider, M. F. (2009). Wave propagation in lipid monolayers. *Biophysical journal*, 97(10):2710–6.

Guttenberg, Z. (2001). Zelladhäsion als Benetzungsübergang. *Dissertationsschrift Technische Universität München.*

Hartmann, A., Stamp, M., Kmeth, R., Buchegger, S., Stritzker, B., Saldamli, B., Burgkart, R., Schneider, M. F., and Wixforth, A. (2013). A novel tool for dynamic cell adhesion studies - the De-Adhesion Number Investigator DANI. *Lab on a chip*, pages 542–546.

Hendriks, J. G. E., van Horn, J. R., van der Mei, H. C., and Busscher, H. J. (2004). Backgrounds of antibiotic-loaded bone cement and prosthesis-related infection. *Biomaterials*, 25(3):545–556.

Israelachvili, J. N. (2010). *Intermolecular and Surface Forces Third Edition.*

Jarzynski, C. (1997). Equilibrium free-energy differences from nonequilibrium measurements: A master-equation approach. *Physical Review E*, 56(5):5018–5035.

Kaufmann, K., Hanke, W., and Corcia, A. (1989). *Ion channel fluctuations in pure lipid bilayer membranes: control by voltage.*

L. L. Hench, E. C. E. (1982). *Biomaterials - An Interfacial Approach.* Academic Press Inc., New York, NY.

Landau, L. D. and Lifshitz, E. M. (1980). *Course of Theoretical Physics Vol. 05 Statistical Physics.* Pergamon Press Ltd.

Lew Yan Voon, L. C. and Willatzen, M. (2011). Electromechanical phenomena in semiconductor nanostructures. *Journal of Applied Physics*, 109(3):031101.

Li, H., Friend, J., Yeo, L., Dasvarma, A., and Traianedes, K. (2009). Effect of surface acoustic waves on the viability, proliferation and differentiation of primary osteoblast-like cells. *Biomicrofluidics*, 3(3):34102.

Li, H., Friend, J. R., and Yeo, L. Y. (2007). A scaffold cell seeding method driven by surface acoustic waves.

Lindken, R., Rossi, M., Grosse, S., and Westerweel, J. (2009). Micro-Particle Image Velocimetry (microPIV): recent developments, applications, and guidelines. *Lab on a chip*, 9(17):2551–67.

Lorz, B. G. (2003). Etablierung eines Modellsystems der Zelladhäsion über spezifische Bindungen geringer Affinität eine mikrointerferometrische Studie. *Dissertationsschrift*.

Lu, H. P., Xun, L., and Xie, X. S. (1998). Single-molecule enzymatic dynamics. *Science (New York, N.Y.)*, 282(5395):1877–1882.

Lu, X., Liu, Y., Kong, X., Lobie, P. E., Chen, C., and Zhu, T. (2013). Nanotoxicity: A growing need for study in the endocrine system. *Small*, 9(9-10):1654–1671.

Marx, S., Schilling, J., Sackmann, E., and Bruinsma, R. (2002). Helfrich Repulsion and Dynamical Phase Separation of Multicomponent Lipid Bilayers. *Physical Review Letters*, 88(13):138102.

Merkel, R., Nassoy, P., Leung, a., Ritchie, K., and Evans, E. (1999). Energy landscapes of receptor-ligand bonds explored with dynamic force spectroscopy. *Nature*, 397(6714):50–3.

Monsees, T. K., Barth, K., Tippelt, S., Heidel, K., Gorbunov, a., Pompe, W., and Funk, R. H. W. (2005). Effects of different titanium alloys and nanosize surface patterning on adhesion, differentiation, and orientation of osteoblast-like cells. *Cells, tissues, organs*, 180(2):81–95.

Myllymaa, K., Myllymaa, S., Korhonen, H., Lammi, M. J., Tiitu, V., and Lappalainen, R. (2009). Interactions between Saos-2 cells and microtextured amorphous diamond or amorphous diamond hybrid coated surfaces with different wettability properties. *Diamond and Related Materials*, 18(10):1294–1300.

Nuschele, S. (2010). The Role of Interfaces in Enzyme Activity and Cell Adaptation. *Dissertationsschrift Universität Augsburg*.

Okumura, A., Goto, M., Goto, T., Yoshinari, M., Masuko, S., Katsuki, T., and Tanaka, T. (2001). Substrate affects the initial attachment and subsequent behavior of human osteoblastic cells (Saos-2). 22:2263–2271.

Onsager, L. (1931). Reciprocal relations in irreversible processes. I. *Physical Review*, 37:405–426.

Quirynen, M., De Soete, M., and van Steenberghe, D. (2002). Infectious risks for oral implants: a review of the literature. *Clinical oral implants research*, 13(1):1–19.

Sackmann, E. (2004). Mikromechanik der Zelle. *Physik Journal*, 3(2):35–42.

Sackmann, E. (2006). Haftung fur Zellen. *Physik Journal*, 5(8):27–34.

Sackmann, E. and Bruinsma, R. F. (2002). Cell adhesion as wetting transition? *Chemphyschem : a European journal of chemical physics and physical chemistry*, 3(3):262–9.

Sackmann, E. and Merkel, R. (2010). *Lehrbuch der Biophysik*. Wiley-VCH, Berlin.

Sadler, J. E. (1991). von Willebrand Factor (Minireview). *The Journal of Biological Chemistry*, 866(34):22777–22780.

Sadler, J. E. (1998). BIOCHEMISTRY AND GENETICS. pages 395–424.

Schilpp, P. A., editor (1970). *Albert Einstein Philosopher-Scientist*. MJF Books, New York, NY.

Schmid, L., Wixforth, A., Weitz, D. a., and Franke, T. (2011). Novel surface acoustic wave (SAW)-driven closed PDMS flow chamber. *Microfluidics and Nanofluidics*, 12(1-4):229–235.

Schneider, M. F. (2010). Thermodynamische Zustände und Übergänge als Grundlage biologischer Funktionen - Habilitationsschrift an der Universität Augsburg.

Schneider, S. W., Nuschele, S., Wixforth, a., Gorzelanny, C., Alexander-Katz, a., Netz, R. R., and Schneider, M. F. (2007). Shear-induced unfolding triggers adhesion of von Willebrand factor fibers. *Proceedings of the National Academy of Sciences of the United States of America*, 104(19):7899–903.

Schrödinger, E. (1944). *What is Life?* Cambridge University Press, Cambridge.

Schrödinger, E. (1985). *Mein Leben, meine Weltansicht*. Verlag Zsolnay, Wien.

Schwarz, F. P., Hauser-Gerspach, I., Waltimo, T., and Stritzker, B. (2011). Antibacterial properties of silver containing diamond like carbon coatings produced by ion induced polymer densification. *Surface and Coatings Technology*, 205(20):4850–4854.

Schwarz, U. (2015). Physik der Zelladhäsion. *Physik Journal*, 14(7).

Shiokawa, S., Matsui, Y., and Ueda, T. (1989). Liquid streaming and droplet formation caused by leaky Rayleigh waves. *Ultrasonics Symposium, 1989*, pages 643–646.

Sigma-Aldrich (2013). Calcein green, http://www.sigmaaldrich.com/catalog/product/sigma/c0875?lang=de&region=DE, 07.03.2013.

Singer, S. J. and Nicolson, G. L. (1972). The fluid mosaic model of the structure of cell membranes. *Science (New York, N.Y.)*, 175(4023):720–31.

Springer, T. a. (2011). Biology and physics of von Willebrand factor concatamers. *Journal of thrombosis and haemostasis : JTH*, 9 Suppl 1:130–43.

Steppich, D., Griesbauer, J., Frommelt, T., Appelt, W., Wixforth, a., and Schneider, M. (2010). Thermomechanic-electrical coupling in phospholipid monolayers near the critical point. *Physical Review E*, 81(6):061123.

Stigler, J., Ziegler, F., Gieseke, A., Gebhardt, J. C. M., and Rief, M. (2011). The complex folding network of single calmodulin molecules. *Science (New York, N.Y.)*, 334(6055):512–6.

Stöcker, H. (2000). *Taschenbuch der Physik*. Verlag Harri Deutsch, Frankfurt am Main, 4., korrig edition.

Strobl, C. J. (2005). Mikro- und Nanofluidik auf piezoelektrischen Substraten. *Dissertationsschrift Ludwig-Maximilians-Universität München*.

Strobl, F. G., Seitz, F., Westerhausen, C., Reller, A., Torrano, A. a., Bräuchle, C., Wixforth, A., and Schneider, M. F. (2014). Intake of silica nanoparticles by giant lipid vesicles: influence of particle size and thermodynamic membrane state. *Beilstein journal of nanotechnology*, 5:2468–2478.

Terraube, V., Pendu, R., Baruch, D., Gebbink, M. F. B. G., Meyer, D., Lenting, P. J., and Denis, C. V. (2006). Increased metastatic potential of tumor cells in von Willebrand factor-deficient mice. *Journal of thrombosis and haemostasis : JTH*, 4(3):519–26.

Thorwarth, G., Saldamli, B., Schwarz, F., Jürgens, P., Leiggener, C., Sader, R., Haeberlen, M., Assmann, W., and Stritzker, B. (2007). Biocompatibility of Doped Diamond-Like Carbon Coatings for Medical Implants. *Plasma Processes and Polymers*, 4(S1):S364–S368.

Usami, S., Chen, H. H., Zhao, Y., Chien, S., and Skalak, R. (1993). Design and construction of a linear shear stress flow chamber. *Annals of biomedical engineering*, 21(1):77–83.

WebSource01 (2013). Metaphysics, http://classics.mit.edu/Aristotle/metaphysics.8.viii.html 08.04.2013.

WebSource02 (2013). Wikimedia, http://bit.ly/25du6UK, 20.05.2016.

Weiss, L. (1961). The measurement of cell adhesion. *Experimental Cell Research*, 153:141–153.

Westerhausen, C. (2012). On the role of soft interfaces for the understanding of blood clotting. *Dissertationsschrift Universität Augsburg*.

White, R. M. and Voltmer, F. W. (1965). Direct Piezoelectric Coupling To Surface Elastic Waves. *Applied Physics Letters*, 7(12):314.

Willebrand, E. V. (1999). Hereditary pseudohaemophilia. *Haemophilia*, 5(3):223–231.

Winterhalter, M. (2000). Black lipid membranes. *Current Opinion in Colloid & Interface Science*, 5(3-4):250–255.

Wixforth, A. (2006). Acoustically Driven Programmable Microfluidics for Biological and Chemical Applications. *JALA - Journal of the Association for Laboratory Automation*, 11(6):399–405.

Wixforth, A. (2009). Acoustically driven microfluidic applications for on-chip laboratories. In *2009 IEEE International Frequency Control Symposium Joint with the 22nd European Frequency and Time Forum*, pages 778–783.

Wixforth, A., Strobl, C., Gauer, C., Toegl, A., Scriba, J., and Guttenberg, Z. V. (2004). Acoustic manipulation of small droplets. *Analytical and Bioanalytical Chemistry*, 379(7-8):982–991.

Woodside, M. T., Anthony, P. C., Behnke-Parks, W. M., Larizadeh, K., Herschlag, D., and Block, S. M. (2006). Direct measurement of the full, sequence-dependent folding landscape of a nucleic acid. *Science (New York, N.Y.)*, 314(5801):1001–4.

Wunderlich, B., Leirer, C., a L Idzko, Keyser, U. F., Wixforth, a., Myles, V. M., Heimburg, T., and Schneider, M. F. (2009). Phase-state dependent current fluctuations in pure lipid membranes. *Biophysical journal*, 96(11):4592–7.

Ying, J., Ling, Y., Westfield, L. a., Sadler, J. E., and Shao, J.-Y. (2010). Unfolding the A2 domain of von Willebrand factor with the optical trap. *Biophysical journal*, 98(8):1685–93.

Chapter 7

Acknowledgments

Mit dem Fertigstellen meiner Dissertation geht eine erfüllte und erfüllende Zeit ihrem Ende entgegen. Viele Menschen haben mich in diesen Jahren positiv begleitet - ihnen allen gebührt mein Dank, dessen sie sich sicher sein dürfen. Ganz besonders seien an dieser Stelle erwähnt:

Prof. Dr. Matthias F. Schneider
Sehr früh während meines Studiums sind wir bereits aufeinander getroffen, als Du für meine ersten Physik-Klausuren zuständig warst und ich durch Dich einen Einblick in die faszinierende Welt der Biophysik erhielt. Nachdem ich in verschiedene Bereiche der Physik einen Blick geworfen hatte, hast Du mir die Möglichkeit gegeben, in Deiner Gruppe als Doktorand zu arbeiten. Herzlichen Dank für die unglaubliche Freiheit, in der ich in Deiner Gruppe wirken durfte. Neben der reinen Forschung im Labor hast Du immer in vielfältiger Weise (Maßbach, Laborvorträge an der Boston University u.v.m.) ermöglicht, dass ich meinen Horizont erweitern konnte, in wissenschaftlicher wie auch sonstiger Hinsicht. Danke für Deine wertvolle Unterstützung und viele inspirierende Gespräche all die Jahre über!

Prof. Dr. Achim Wixforth
Vielen Dank dafür, dass Du Deinen großen Erfahrungshorizont und Dein Wissen mit mir geteilt hast - ebenfalls bereits seit Beginn meines Studiums in der Grundvorlesung bis hin zum Doktorandendasein. Ich durfte an Deinem Lehrstuhl viel Lernen über Physik und deren Übersetzung in technologische Anwendungen, das "System Wissenschaft" und hervorragende Personalführung. Vielen Dank für das große Vertrauen, dass Du mir immer entgegengebracht hast und die vielfältigen Entfaltungsmöglichkeiten, die Du mir eingeräumt hast - an Deinem Lehrstuhl arbeiten zu dürfen habe ich stets als ein großes Privileg empfunden!

Prof. Dr. Armin Reller
Vielen herzlichen Dank Ihnen für die Bereitschaft, das Zweitgutachten dieser Arbeit anzufertigen. Daneben gilt mein Dank für die Einblicke in die Biomineralisation und (Bio-)Chemie, die ich durch Sie gewonnen habe, wertvolles Wissen nicht nur, aber auch während der Doktorandenzeit. Darüber hinaus möchte ich Ihnen danken, dass Sie mir das zweite große Thema (neben der Biophysik) meiner Zeit an der Universität erschlossen haben, die Thematik der "Ressourcenstrategie".

Dr. Konrad Kaufmann
Herzlichen Dank für unzählige Diskussionen, meist über Wissenschaft und Philosophie, mitunter auch über diverse Niederungen des normalen Lebens. Deine *unvergleichlichen* Vorträge haben immer großen Eindruck auf mich gemacht. Danke für das Teilen all Deiner Einsichten über Thermodynamik, Einstein, Hirn-Theorie und Philosophie. Falls ich je die Fähigkeit erworben habe, klar und geradeaus zu denken, hattest Du großen Anteil daran!

Biophysics group
My thanks also go to the whole biophysics group for a really great atmosphere both in terms of collaboration as well as interpersonal relations. Thanks for all the support in the lab, thanks for inspiring discussions. It was a great joy to work and spend time together with you! In particular my thanks to Dr. Stefan Nuschele, Dr. Mohammad Amin "Babak" Fallah, Dr. Josef Griesbauer, Dr. Stefan Bössinger, Dr. Christoph Westerhausen, Dr. Christian "K&K" Fillafer, Dr. Shamit Shrivastava, Dr. Bernhard Fichtl, Dominik Breyer and Florian Strobl.

Studierende
Herzlichen Dank an meine fleißigen und talentierten Studierenden, deren Master- bzw. Bachelorarbeiten ich betreut habe. Vielen Dank für euer Engagement im Labor und beim Auswerten von Daten, liebe Mella (Melanie Stamp), lieber Markus (Markus Rennhak), lieber Flo (Florian Salmen). Alles herzlich Gute für eure Zukunft!

Mitarbeiter am Lehrstuhl für Experimentalphysik I, Uni Augsburg
Neben der Arbeitsgruppe Biophysik war/ist eine Vielzahl weiterer Personen am EP I tätig, die ebenfalls für hervorragende Arbeitsbedingungen sowie eine ganz exzellente zwischenmenschliche Atmosphäre sorg(t)en - es war mir eine wahre Freude, mit euch zusammenzuarbeiten, Labore, sonstige Räumlichkeiten, Gerätschaften sowie Freud und Leid mit euch allen zu teilen. Insbesondere blicke ich dankbar zurück auf meine Bürogemeinschaft in 305 sowie auf den "Mythos 308".

Prof. Evan Evans group at UBC, Vancouver
I had the great honor and joy to visit the group of Prof. Evan Evans at the University of British Columbia, Vancouver, where I had the opportunity to learn the BioForceProbe technique. Thanks a lot for all the support I thankfully received from you guys - both academically as well as personally. Thanks to Prof. Dr. Evan Evans, Prof. Dr. Koji Kinoshita, Dr. Andrew Leung and Prof. Dr. Igor Kuznetsov.

Boston University
Besides the Biophysics group, I had further awesome support at Boston University from Dr. Mark J. Bradshaw, in particular in terms of working at the infernal machine, the BFP, which was a physically demanding task. Thanks for your support! Beyond that, you and Vanessa introduced me into the campus life and all things connected with with it. Thanks to both of you for being such nice hosts!

Finanzierung und institutioneller Rahmen
All diese schöne Forschung und all diese damit verknüpften persönlichen Erfahrungen wären nicht möglich gewesen ohne eine adäquate Finanzierung. Zunächst meinen Dank an die Bayerische Forschungsstiftung, die mir ein Stipendium gewährt hat und sich stets als unbürokratischer und unkomplizierter Finanzierungspartner gezeigt hat. Darüber hinaus war ich eingebunden in das "NIM Graduate Program", das Graduiertenprogramm der Nanosystems Initiative Munich. Vielen Dank sowohl für stellenweise finanzielle Unterstützung bei Forschungsvorhaben, vor allem aber auch für das Schaffen eines vorzüglichen Netzwerks unter den Doktoranden der beiden Münchner Universitäten sowie der Uni Augsburg - stets stimulierende Gespräche sowie produktive Zusammenarbeit waren die Früchte dieses Rahmens. Hierin steht nicht nach der Rahmen, den uns Doktoranden das "Center for NanoScience" geboten hat - in den Worten eines Doktorandenkollegen: "Auf dem CeNS!".

Freunde und Familie
Neben der Forschung bleibt man Mensch - ich bin sehr dankbar für viele gute Freunde sowie meine Familie, die mir immer persönlich starken Rückhalt geboten haben, die mit mir viel Freud und wenig (weil kaum vorhandenes) Leid geteilt haben. Danke für all eure ideelle Unterstützung - dies bereichert solch eine Arbeit weit mehr, als manch einer zunächst vermuten würde.

Daniela
All die Jahre stand mir zur Seite eine ganz besondere junge Frau - Daniela, vielen Dank für die Liebe, mit der Du mich die letzten Jahre begleitet hast! Manch graues Haar ist in dieser Zeit meinen Schläfen entwachsen - das wird jetzt vielleicht wieder weniger, vielleicht.....